

Dissertation
submitted to the
Combined Faculties of the Natural Sciences and Mathematics
of the Ruperto-Carola-University of Heidelberg, Germany
for the degree of
Doctor of Natural Sciences

Presented by
Isabel Franco Rico
born in: Mexico City, Mexico
Oral examination: 4th Feb, 2011

The origin of low-mass early-type galaxies:
A combined view from stellar populations
and N-body simulations

Referees:

Dr. Thorsten Lisker

Prof. Dr. Ralf Klessen

Kurzfassung

Anhand der Daten des COMBO-17 Projekts werden stellare Massen von Galaxien frühen und späten Typs im Rotverschiebungsbereich $0 < z < 2.1$ bestimmt. Hierarchische Strukturentstehung sagt voraus dass sich elliptische Galaxien etwa bei $z \approx 1$ bilden, d.h. den Bereich der "blue cloud" verlassen. Der Übergang von "blue cloud" zu "red sequence" ist noch nicht vollständig verstanden. Wir untersuchen einen Entstehungsmechanismus, der möglicherweise erklären kann, wie sich Galaxien späten Typs in elliptische Galaxien geringer Masse durch sogenanntes "harassment" umwandeln. Wir führen N-Körpersimulationen durch, in denen eine dreikomponentige Galaxie (Scheibe + Bulge + Halo) auf einer exzentrischen Bahn in einen Galaxienhaufen eindringt. Während die Galaxie in den Haufen stürzt, wird sie durch Gezeitenkräfte von nahen Vorbeiflügen an anderen Haufengalaxien auseinandergerissen. Solche Kräfte sind stark genug, um eine morphologische Umwandlung der Galaxie in eine elliptische Zwerggalaxie zu bewirken. Im Rahmen eines kombinierten N-Körper- und Sternpopulations-Ansatzes ordnen wir der simulierten Galaxie unterschiedliche Sternpopulationen zu und verfolgen deren Entwicklung. Dies erlaubt es uns, beobachtbare Größen, insbesondere integrierte Farben, zu extrahieren, um die Simulationsergebnisse mit beobachteten elliptischen Zwerggalaxien aus dem Virgohaufen zu vergleichen. Dies bildet die Grundlage der Diskussion, ob durch harassment typische elliptische Zwerggalaxien gebildet werden können.

Abstract

The COMBO-17 survey data is used to measure stellar masses of late and early-type galaxies in the redshift range $0 < z < 2.1$. Hierarchical galaxy formation predicts that early-type galaxies leave the blue cloud and assemble at $z \approx 1$. The transit from blue cloud to red sequence is yet not fully understood. We explore one formation mechanism that might explain how late-type galaxies can transform in low-mass early type galaxies via galaxy harassment. We aim to understand the formation of early-type dwarf galaxies through the so-called galaxy harassment scenario. We perform N-body simulations in which a three-component galaxy (disk + bulge + halo) enters a galaxy cluster in an eccentric orbit. While the galaxy is falling, it gets tidally disrupted by close encounters with other galaxies that populate the cluster. Such encounters are sufficiently vigorous to morphologically transform the galaxy into an early-type dwarf.

Through a combined N-body and stellar population approach, we assign multiple stellar generations to the simulated galaxy and trace their evolution. This allows us to extract observable quantities, in particular integrated colours, in order to compare the simulation results to observed Virgo cluster early-type dwarfs. Based on this analysis we discuss whether harassment is able to form typical early-type dwarf galaxies.

Part I

Contents

1	Introduction	4
2	Data and Photometry	7
2.1	The COMBO-17 Optical data	7
2.2	The ESO/EIS GOODS-ISAAC JHK bands data	8
2.3	J,H,Ks Photometry	10
3	The new galaxy spectral template library	12
3.1	Library build-up	14
3.1.1	The star formation scenario	15
3.1.2	The extinction law of Pei 1992	17
3.1.3	The galaxy color library	19
3.2	Object multicolor classification and redshift estimation	19
4	Restframe properties of galaxies in the GOODS-CDFS	24
4.1	The galaxy sample	25
4.1.1	Sample Criteria	25
4.1.2	Comparison between the new galaxy library and the Wolf galaxy library	27
4.2	Restframe luminosities	32
4.3	Red sequence evolution of galaxies until $z=2.2$	36
4.4	Stellar mass estimation	38
5	Conclusions	45

Chapter 1

Introduction

To understand how galaxy evolution takes place in the Universe, it has been necessary to build extragalactic surveys with several filters that can allow to perform studies in order to test and confirm the galaxy evolution theories.

In the frame of hierarchical galaxy evolution where more massive galaxies form from smaller ones by interacting between each other and merging there are several predictions that can be confirmed by sampling the galaxies contained in the surveyed fields locally and at $z \geq 1$.

One of the main predictions of this galaxy evolution theory is that early-type galaxies begin to assemble at $\approx z = 1$ leaving the blue cloud and beginning to establish the red sequence approximately at this redshift. As a consequence, the stellar mass density of the early-type galaxy population increases since $z \approx 1$ (Kauffmann & Charlot 1998). Also, it has been proved that the cosmic SFR has declined by an order of magnitude since $z \approx 1$ (Madau et al. 1998).

Thus, it would be interesting to have a galaxy sample suitable to trace the evolution of galaxies up to higher redshifts in order to test and study the galaxy evolution theory predictions. For this, is necessary to carry out deep observations with different filters that can provide with information about the properties of galaxies in terms of its stellar populations, age, stellar mass, etc.

One of the main aims of this work, is to extend the observed wavelength range coverage of the COMBO-17 multicolor classification extragalactic survey to the infrared wavelength regime. This survey already has a filter set consisting of five broad band filters and twelve narrow band covering the optical range from 365nm to the beginning of the near infrared regime at

917nm. This filter set allows to perform object classification and estimate their photometric redshifts in the five survey fields up to redshift $z = 1.1$.

One of the limitations of this survey is that as galaxies contain a significant population of old stars that at higher redshifts become too faint to be observed with optical filters, it is necessary to expand the survey to the infrared wavelength regime in order to be able to measure the contribution of the old stellar populations constituting the galaxies what is reflected by the raise of the flux of the galaxies in the infrared wavelength range.

The COMBO-17 field S11 was the first survey field to include two infrared filters (J and H) to begin with the extension of the survey towards near infrared wavelengths. In this work, the Chandra Deep Field South (CDFS) was chosen to be the second survey field to continue the survey extension to the near infrared bands. Although there was no near infrared data available to cover the CDFS in its totality, it became possible to cover a part of the field (GOODS-CDFS sub field) using the public available data provided by the ESO/EIS ISAAC GOODS-CDFS for the filters J, H and Ks.

The way the COMBO-17 survey performs object classification is based in the colors measured by its filter set. We say that it is a color based survey in the sense that one fits an artificial galaxy template to the observed spectral energy distribution (SED) of the observed galaxies in the field and compares the observed colors measured by its filter set with the colors of the artificial galaxy spectral template that fits best the observed galaxy SED giving as result together with the object classification the photometric redshift of the galaxy.

Another aim of the work presented here is to generate an artificial galaxy template set suitable to perform the multicolour classification mentioned above. So far the COMBO-17 survey has delivered galaxy classification and redshift estimation with a set of templates that were built empirically in order to match the photometric SEDs of the objects in the CDFS (Wolf, et al. 2003) using a non-realistic single star forming burst as star formation rate. As a result, this library delivers accurate redshift estimation but it is not suitable to derive important quantities that allow to carry out galaxy evolution studies (e.g.stellar masses of galaxies). That is why it is necessary to develop a different set of artificial templates that can provide with a more realistic approach of how galaxies are constituted in terms of their stellar populations.

A new set of artificial galaxy templates is developed in order to match the SEDs of galaxies with a spectra that is composed of a mix of young and old stellar populations. This is achieved by giving a more realistic star forming scenario consisting of two star forming bursts where the first one is followed by a second one that varies the amount of its young blue newly formed stars once the stars created in the first burst are red and some of them have already begun to die. This two burst model matches successfully the galaxy spectra and delivers accurate and improved photometric redshifts.

The results of the extension of the COMBO-17 optical filter set to the infrared wavelength range are shown in this work. New multicolor object classification was performed and new photometric redshifts were estimated. A galaxy sample was selected and used to test from the technical point of view the quality of the newly estimated redshifts. Later on, it was used to analyse the establishment of the red sequence galaxies at $z \approx 1$. Stellar masses were obtained for this galaxy sample using to already existing stellar mass methods (Bell et al. 2004, Borch et al. 2006). It turns out that even though the selected sample is limited in size, it has been proved that this is a successful way to derive galaxy properties that allow to study galaxy evolution up to redshift $z = 2.2$.

Chapter 2

Data and Photometry

The inclusion of a new dataset covering the near infrared wavelength range brings the opportunity to the COMBO-17 extragalactic survey to extend its filter set coverage to perform multicolour classification to higher redshifts in its five fields. The near infrared data from the ESO/EIS ISAAC GOODS-CDFS will allow the survey to improve the template fitting of the objects contained in its fields and thus, provide more accurate redshifts as well as to improve multicolor object classification for the galaxies and at the same time put some constraints concerning the dust reddening in galaxies. The main aim of this inclusion is to extend the redshift range of the survey from $z = 0 - 1.1$ up to $z \approx 2.2$. Thus, stellar masses of galaxies can be estimated as it is possible to see the mass contribution of the old stellar populations that dominate the total stellar mass of the galaxies.

2.1 The COMBO-17 Optical data

The COMBO-17 optical data was observed with the Wide Field Imager (WFI) at the 2.2m MPG/ESO telescope in La Silla, Chile. The WFI covers a field of view of $34' \times 33'$ on a CCD mosaic consisting of eight $2k \times 4k$ CCD's with a scale of $0.238''$. This multicolor survey has successfully completed 1 squared degree of observations in its five different fields with its 5 broad-band and 12 narrow-band filters covering the entire optical range from 400nm to 930nm (see tables 2.1, 2.1). In this work, we have focused mainly in the Chandra Deep Field South (CDFS) centered in the coordinates $\alpha_{2000} = 03^h 32^m 25^s$ and $\delta_{2000} = -27^\circ 48' 50''$ (Fig. 2.1). Observations were made in four different observing runs between October 1999 and February 2001. The total exposure time is $\approx 195ks$ using $\approx 35ks$ for deep R-band imaging.

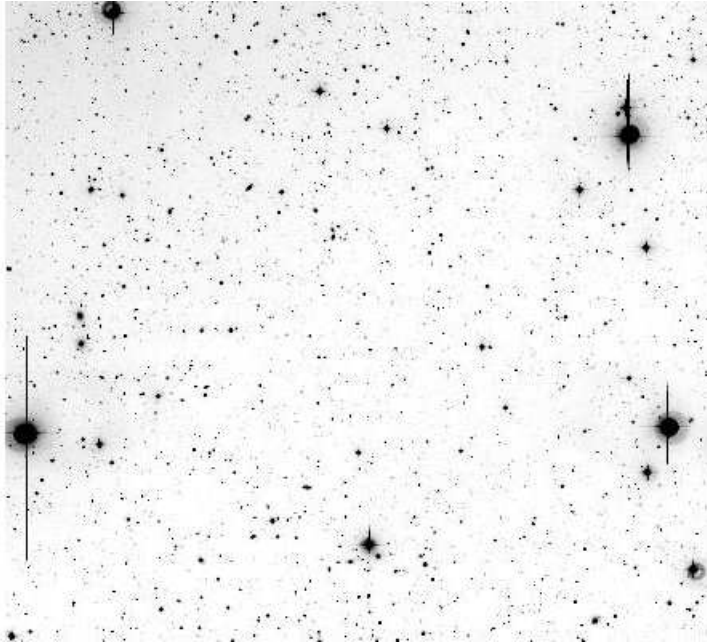


Figure 2.1: COMBO-17 survey deep R-band image of the Chandra Deep Field South $\alpha_{2000} = 03^h 32^m 25^s$ and $\delta_{2000} = -27^\circ 48' 50''$. The detection limit of the survey is $R \leq 26$. The total exposure time of the COMBO-17 deep R-band image is of 35ks.

The source extraction software SExtractor (Bertin & Arnouts 1996) was used for object detection. The default parameter file was modified in order to first search for the deepest objects and get rid of the ones that have a S/N higher than 3 (≈ 0.3 error in magnitude). The resulting catalogue has 63,501 objects reaching a 5σ point source limit of $R \approx 26$.

2.2 The ESO/EIS GOODS-ISAAC JHK bands data

The infrared data used in this work, is the Version 1.5 of the ESO-EIS GOODS-ISAAC data release. It covers 159.1 and 159.7 arcmin of the GOODS-CDFS region. This data was taken in three infrared bands J,H,Ks (see table 2.3) where J,Ks bands cover the whole field (24 sub fields) while H band covers 126.7 arcmin (19 sub fields) (Fig. 2.2). Data was fully reduced by the Advanced Data Products group in the Virtual Observatory Systems.

Mosaic images for the three bands are also available, but they were not used as the PSF varies from tile to tile within each mosaic. This data set has no aperture corrections nor PSF matching what would lead to the obtention

Filter (nm)	Name	Exposure time (sec)	$5 - \sigma$ limit	Mag (Vega)
365/40	U	20000	24.3	24.7
455/100	B	14000	25.7	25.9
540/90	V	6000	25.2	25.3
650/165	R	20000	26.0	26.2
850/150	I	7500	23.8	23.2

Table 2.1: Broad band filter set of the COMBO-17 survey

Filter/width (nm)	Exposure (sec) time	$5 - \sigma$ limit	Mag (Vega)
420/30	8000	24.4	24.7
465/15	10000	24.3	24.9
486/30	5000	24.2	24.3
518/16	6000	24.1	24.3
571/24	4000	24.0	24.2
605/21	5000	23.9	24.2
646/27	4500	23.8	23.2
696/23	6000	23.6	23.9
752/20	8000	23.5	23.2
816/24	20000	23.4	23.6
856/14	15000	23.3	22.8
914/27	15000	23.2	22.6

Table 2.2: Narrow band filter set of the COMBO-17 survey

of non precise object catalogues.

The ISAAC/GOODS-CDFS data was already reduced with the ESO/MVM data reduction pipeline. The resulting science images are co-added sky subtracted frames. Calibration was performed by using a pre-existing catalogue of the field. It was then compared with already calibrated Hubble Space Telescope (HST) data. The RMS scatter in the astrometry is $0.1''$ in the whole field. The science images were first PSF-matched and convolved with a Gaussian. The zero points were determined using approximately 3 to 12 sources in each of the frames. Its aperture magnitude was measured and used after to determine the zero points. The RMS scattering in the zero points are: $0.1 - 0.06mag_{AB}$ in J-band, $0.01 - 0.08mag_{AB}$ in Ks-band and up to $0.17mag_{AB}$ in H-band. The exposure times are given normalized to unity, so that the magnitudes can be obtained using $m_{AB} = -2.5 * \text{Log}(F) + \text{zero point}$. In order to make this images suitable for the COMBO-17 pho-

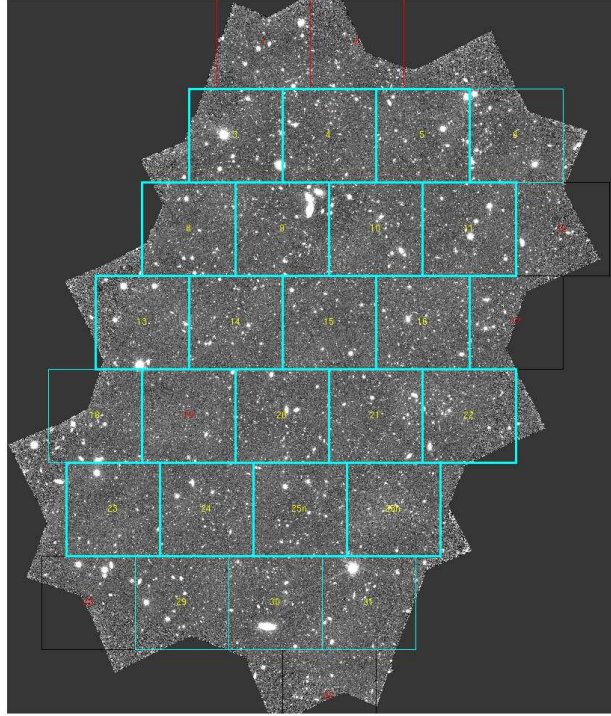


Figure 2.2: Mosaic of ISAAC tiles, overlaid on the HST/ACS GOODS z-band mosaic: 21 tiles in the J and Ks bands (cyan thick), 5 additional tiles in the J and Ks bands (cyan, thin). Each ISAAC field is 2.5 arcmin ESO-EIS GOODS/ISAAC Data Release: Version 1.5

tometry, they had to be rescaled, as the COMBO-17 images have a pixel scale of $0.38''$, while the ISAAC/GOODS images have a pixel scale of $0.15''$. Also, COMBO-17 works in Vega magnitudes while ISAAC/IMAGES are in the AB system, for this was necessary to use the AB zero point corrections given by the GOODS team: $J_{AB} = J_{Vega} + 0.90$, $H_{AB} = H_{Vega} + 1.38$, and $K_{sAB} = K_{sVega} + 1.86$.

2.3 J,H,Ks Photometry

The photometry was carried out using the astronomical software package MPIAPHOT (Meisenheimer, Roeser (1991), Meisenheimer (2004)) devel-

Filter/width(μm)	Name
1.25/0.29	J
1.65/0.30	H
2.16/0.27	Ks

Table 2.3: ESO/EIS ISAAC filter set

oped at the Max Planck Institute for Astronomy. MPIAPHOT measures the central surface brightness of the objects after convolving their appearance outside the atmosphere to an effective point spread function (PSF) of 1.5'' diameter. The command routines had to be modified in order to be suitable for photometry analysis in the infrared wavelength regime.

To begin the photometry, it was necessary to obtain a catalogue containing all the sources detected in all the different science images for the three different infrared bands and project its coordinates into the reference frames of each single exposure using the command ISAAC/PROJECT. For this science images it was not necessary to correct for frame translation and rotation but in principle this command also performs these corrections. This was verified by checking that the RMS values of the errors in the position were less than 0.13 in order to avoid mis-matching that can lead to an error in the photometry. Then the stellar PSF is measured by selecting between 50 to 500 bright stars in each of the frames, the program chooses the most suitable Gaussian smoothing for reaching the common effective PSF of 1.5''. After this step, all flux measurements are averaged into a single final flux where its error is obtained from the scatter between the frames. The final step is then to normalize the flux of the objects in each of the frames. The COMBO-17 CDFS field just has one standard star, the number 60783 in the COMBO-17 survey catalogue, located at $\alpha = 03^h 32^m 02^s .360$ and $\delta = -27^\circ 34' 22''.1$ with an R-band magnitude of 15.5, unfortunately, it falls out of the GOODS-CDFS field, hence, we had to incorporate it into each of the three flux-band catalogues to be normalized.

Afterwards, the count rates were converted into physical fluxes by calibrating the counts with the standard star and the filter transmission curves using the MPIAPHOT command ISAAC/INTEG. The flux calibration is then carried out by using the ISAAC/FLUX command that convolves the spectra of the standard star with the total system efficiency in all the filters.

Chapter 3

The new galaxy spectral template library

To perform the multicolor classification based in the color of the survey objects, it is necessary to fit an artificial galaxy template to the observed spectral energy distribution (SED) of the galaxies in the field and compare the color indices obtained from the colors measured by the surveys filter set with the color indices created out of the artificial galaxy spectral template that fits best the observed galaxy SED.

A set of spectral galaxy templates has to be produced to match the SED's of the galaxies. This set is called a galaxy library and the way it is created will be discussed in this chapter.

The idea of developing a new galaxy library to perform multicolor classification in the COMBO-17 survey, comes from the aim of reproducing the star formation histories of different types of galaxies more accurately than the current galaxy library used. The new galaxy library will replace the former one as it provides a better match to real galaxy spectra, as well as would deliver more reliable stellar masses of galaxies than the current one, which has a star formation rate formed by a single-burst history.

The previous spectral library for galaxy classification was created in order to match empirically the data but the histories of the objects are not reliable because of the way this library was designed. This has a star forming scenario that has one star forming burst with an initial interstellar medium metallicity of $0.10Z_{\odot}$. The COMBO-17 galaxy survey has used this library in order to perform multicolor classification in three of its five fields including the CDFS.

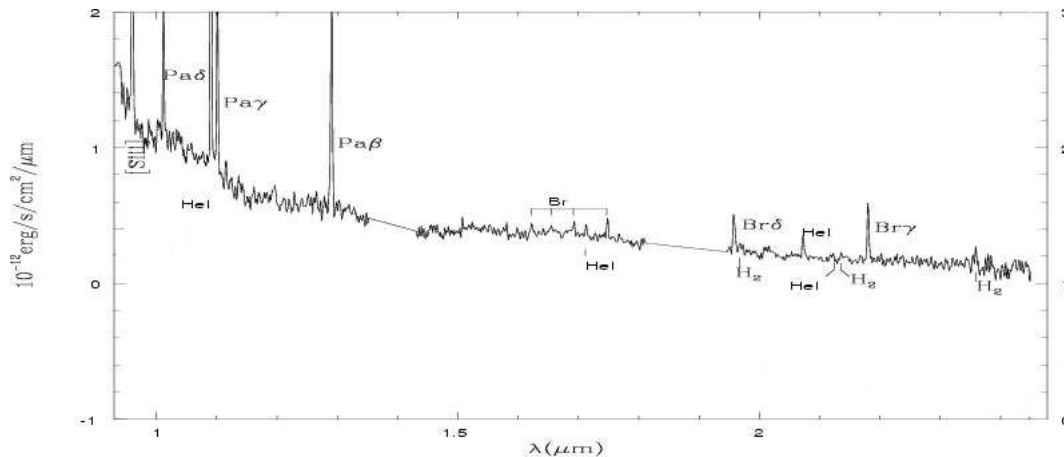


Figure 3.1: The brightest HII region in the galaxy Tol 35 located at a distance of 30.3 Mpc. The regions of poor atmospheric transmission have been replaced by straight lines. Source: L.Vanzi, et al. 2002.

Observations in the Chandra Deep Field South (CDFs) provided an useful set of data in the optical (COMBO-17), near-infrared (GOODS-JHK), wavelength regimes to test and improve a new spectral galaxy template library, designed to operate between the rest-frame wavelength range 0.1μ and $\sim 3\mu$. In this range the stellar continuum and emission lines from HII regions dominate the Spectral Energy Distribution (SED) of galaxies like in the example shown in Fig.3.1. The new filter inclusion plus the new galaxy library were necessary if the aim is to improve the accuracy of the photometric redshifts as well as derive more realistic galaxy properties in terms of stellar population components and its intrinsic extinction.

The new spectral library is built by using a population synthesis code PEGASE 2.0 (Fioc, Rocca-Volmerange 1997) assuming a Kroupa (2003) initial mass function. An old burst of exponentially decaying star formation with an initial metallicity of $0.1Z_{\odot}$ is followed by a second burst that varies in strength in order to reproduce the spectra of very blue galaxies. In addition, the templates include dust extinction of various strengths. For the multicolor classification, the spectral library is redshifted between $z = 0$ and $z = 2.5$ and converted into the colors observed by COMBO-17 plus its near-infrared extension provided by the public ESO-EIS GOODS/ISAAC data. It is important to note that the multicolor classification of the survey is based on the comparison between the measured color indexes of the objects and the color indexes derived from the spectral templates derived from the population synthesis code PEGASE 2.0.

3.1 Library build-up

The spectral galaxy template library is a 2-dimensional 'strength-extinction' library designed to operate between $z = 0 - 2.2$. Strength-extinction means that the library is in one dimension based in the strength of the second star forming burst relative to the strength of the first star forming one. The second dimension is the one that accounts for the extinction or reddening of the galaxies, it provides the galaxy library with different extinction levels that applicable to the spectral galaxy templates resulting from the first library dimension. Extinction is taken into account according to the SMC extinction law (Pei 1992) explained in section 3.1.2.

One of the aims of this new galaxy template library is to extend the current redshift range $z = 0 - 1.1$ to the range $z = 0 - 2.2$. For this, it is necessary to include the ESO-EIS GOODS/ISAAC infrared bands that cover the GOODS sub field located inside the Chandra Deep Field South (CDFS). In this section, the procedure to generate the spectral galaxy library will be explained.

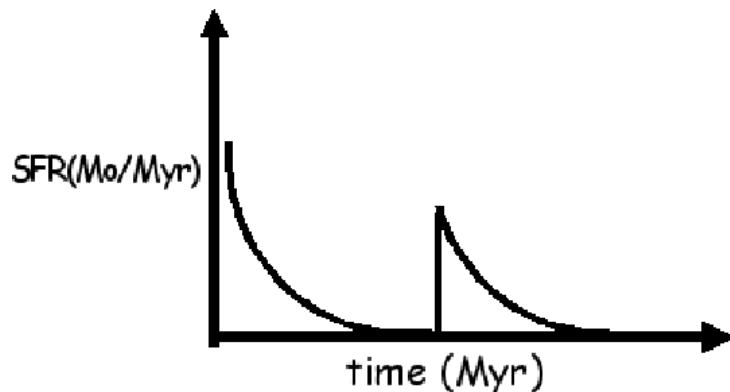


Figure 3.2: Star formation scenario of the 2-dimensional 'strength-extinction' galaxy library. At the beginning one single burst is forming stars. When the age of its old stellar population is older than $3Gyr$ a second burst begins to create stars.

To create the spectral galaxy template library, it was necessary to generate artificial galaxy templates using in this case the stellar population synthesis program PEGASE 2.0. An input file including the essential parameters that characterize a stellar population such as the initial mass function and its lower and upper limits and the type of supernovae ejecta is given as starting point. Then the star forming scenario is also provided, i.e. the metallicity of the interstellar medium (ISM) and the star formation rate (SFR). The program has stellar libraries with evolutionary stellar tracks for different

metallicities that allow to calculate the position of the stars that populate the artificial galaxy in the Hertzsprung-Russell diagram according to the given ISM initial metallicity and the mass of the stars inferred from the given IMF. The program then, calculates the metallicity of ISM gas and stars together with the star formation rate for all the time steps required. In order to produce continuum spectra and emission-line fluxes for all SFHs defined in one scenario file, PEGASE 2.0 delivers an output file containing the spectral data for a given grid of time steps running from 0 to 20 Gyr after the first burst of star formation.

As we wanted a more precise time grid than the default PEGASE 2.0, more time steps were included in the grid using linear interpolation because areas with low grid density reduce the quality of the generated spectra. Later on, additional time steps were again included as the idea was to follow closely the beginning of the second star forming burst. Afterwards, the spectral template library was finally created.

The second dimension of the spectral galaxy library is generated by applying the extinction law of Pei (1992). There is a pre-existing routine created by C. Wolf that applies Pei's extinction law to the template library relative to the B-band absorption in A_B magnitude. Currently, both galaxy libraries (Wolf, et al 2003 and this new one) contain six different absorption values applicable to the spectral galaxy templates as explained above. These values are $A_B = 0.00, 0.42, 0.84, 1.26, 1.68, 2.10$ for a given $E_{(B-V)} = 0.0, 0.1, 0.2, 0.3, 0.4, 0.5$ and following $A_B = 4.2 \times E_{B-V}$.

3.1.1 The star formation scenario

The star formation scenario that was chosen in order to create this new spectral template galaxy library is formed by one first exponentially decaying star forming burst whose interstellar gas has an initial metallicity of $0.1Z_{\odot}$. As mentioned before, several authors take this initial metallicity value as models of galaxy formation predict that when stars begin to form, the metallicity of interstellar medium has this initial value approximately. The gas begins to form stars with an e-folding time of $\tau_1 = 1$ Gyr. The formation of stars out of the interstellar gas is represented by the Initial Mass Function (IMF). For this scenario, the Kroupa(2003) IMF was chosen due to its behaviour in the low-mass end, meaning that the different slopes that shape the IMF seem to give a better description of the behaviour of the masses of the stars that compose the stellar populations than other initial mass functions, e.g. Salpeter (1955).

The first star forming burst is followed by a second short-duration exponentially decaying burst that has an e-folding time of $\tau_2 = 0.1$ Gyr whose

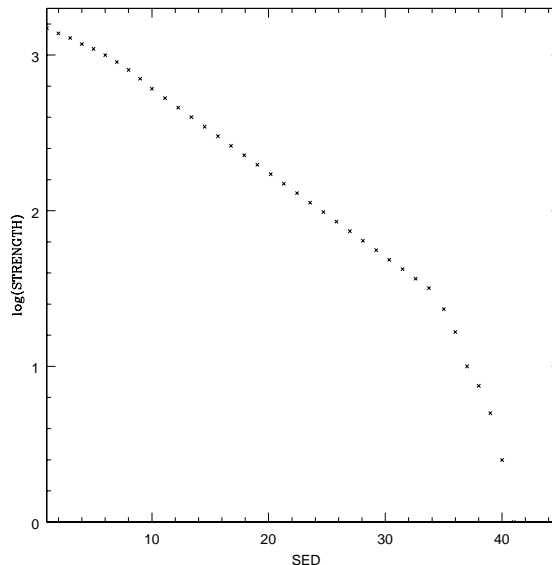


Figure 3.3: Library SED binning for each of the 39 SED's that were created using the star formation history described in Section 2.2.1. Each SED step was calculated for each of the burst strengths. The library was re-binned as it was found that there was a peak in the distribution of galaxies that belong to the blue cloud.

strength varies relative to the strength of the first burst ranging between 1/100 to 15 times the strength of the first star forming burst. This allowed us to reach the spectra of blue galaxies due to the amount of newly formed young stars that will make the synthetic spectra look bluer. This has to be done because even if the amount of massive stars that were formed during the first burst is smaller compared with the amount of low and intermediate mass stars formed the integrated light still depends strongly on the massive stars. Also the fact that their lifetime is shorter than for the low and intermediate mass stars makes the spectra look redder when we look at the star formation just right after the second burst.

The star formation rate $\phi(t)$ is then given by the following equation:

$$\phi(t) = P_1 e^{-(t/\tau_1)} \quad \text{if } t \geq t_{old} \quad (3.1)$$

$$\phi(t) = P_1 e^t + P_2 e^{-(t-3000)/\tau_2} \quad \text{if } t \leq t_{old} \quad (3.2)$$

where P_1 and P_2 are the strengths of each of the star forming bursts. The amount of stars created during the second burst, that is given by the parameter P_2 varies in intensity relative to the amount of stars that were created during the first star forming burst that is represented by parameter

P_1 , t_{old} is the age of the old stellar population when the second star forming burst begins to form stars; in this model, t_{old} is 3 Gyr.

There were several versions of this galaxy spectral library. The results presented in this work are the ones obtained from the last version. It is important to notice that the galaxy template library used to perform the multicolor classification in the way described showed a peak in the early-type galaxy distribution (blue cloud) according to their SED distribution. In order to correct for this problem, the galaxy spectral library had to be re-binned in the first 39 SED's that are the ones that contain the artificial spectra for the blue galaxies (Fig. 3.3). The rest of the SED's are taken from the galaxy spectral library created by C. Wolf (2003) as there is no change for the reddest SED's, this is due to the fact that in this part of the library the second star forming burst is negligible.

3.1.2 The extinction law of Pei 1992

Pei 1992 derived an extinction law based on the empirical extinction curves of the Large and Small Magellanic Clouds (LMC and SMC respectively) by adjusting the relative abundances of graphite and silicate grains and leaving all other properties fixed to those appropriate to the Galactic extinction curve. Properties such as absorption and scattering optical depths, mass-density ratio of the interstellar dust to the neutral hydrogen. He presented a fitting function for the extinction curves of the three galaxies valid over the full wavelength range.

The first step of this law derivation considers the empirical extinction curve defined as:

$$\xi(\lambda) = A_\lambda/A_B \quad (3.3)$$

where A_λ is the extinction in magnitudes at a wavelength λ and A_B is the extinction in the B-band.

Using the relation for the color excess $E_{\lambda-V} = A_\lambda - A_V$ and dividing by E_{B-V} he obtained the following expression:

$$\xi(\lambda) = [(E_{\lambda-V}/E_{B-V}) + R_V] + (1 + R_V) \quad (3.4)$$

where $R_V = A_V/E_{B-V}$, being A_V the extinction in the visual V-band. The second step is to include a dimensionless dust-to-gas ratio, k :

$$k = 10^{21}(\tau_B/N_{H_I}) \quad (3.5)$$

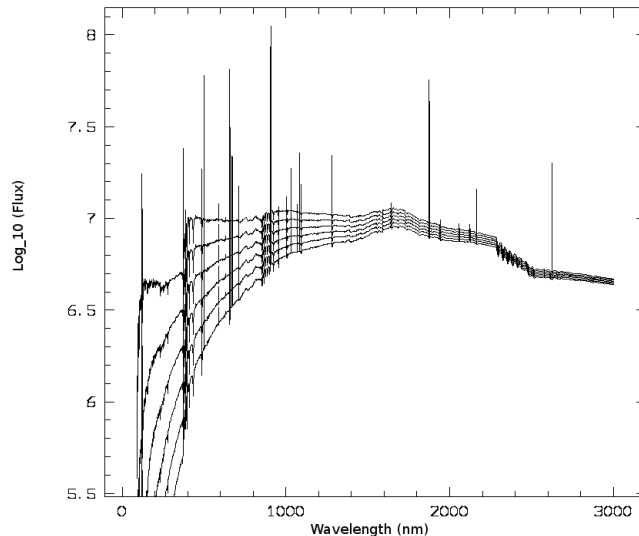


Figure 3.4: Example of the five different extinction levels applied to the galaxy spectral library for a burst strength of $\sim 15\%$ following Pei 1992. The extinction levels in A_B used for the library build-up are $A_B = 0.00, 0.42, 0.84, 1.26, 1.68, 2.10$

where τ_B is the extinction of the optical depth in the B-band relative to the neutral hydrogen column density. Writing it in terms of the color excess, is obtained:

$$k = 9.21 \times 10^{20} (1 + R_V) (E_{B-V} / N_{H_I}) \quad (3.6)$$

Extinction is generally measured from two reddened and two unreddened stars that have almost identical spectra. For the Milky Way, the O and B main-sequence stars are useful for measuring extinction as they have well defined spectral lines besides they are luminous enough to be seen at large distances inside the Galaxy. For the LMC and SMC, OB supergiants are used to measure extinction due to its high brightness in the ultra-violet regime.

To use the equations written above, an average value of R_V is needed. For this is necessary to extrapolate after the mid-infrared range to infinite wavelength.

This method gives more accurate values of R_V than other existing methods used to obtain A_V (Aannestad & Purcell 1973). At the end, the final result is the following equation,

$$E_{\lambda-V} / E_{B-V} = [c(1 + R_V) / 1 + (\lambda / \lambda_B)^2] - R_V \quad \text{for } \lambda \geq \lambda_V \quad (3.7)$$

Afterwards, this equation is fitted to a set of different values for λ^{-1} , $E_{\lambda-V}/E_{B-V}$ for the three galaxies that were compiled from several authors. Plugging this in equation (3.4) a general form for the extinction curve is derived.

3.1.3 The galaxy color library

The COMBO-17 extragalactic survey performs multicolor classification based on the color indices of its filter set, the spectral template galaxy library needs to be converted into a color library by calculating the color indices resulting from the set of SED's contained in the galaxy library. This artificial color indices are compared with the observed colors of the objects in the field and based on this approach the best fitting galaxy template for each of the objects is obtained.

The COMBO-17 survey has a pipeline that carries out the survey multicolor classification. It translates the color library into a four dimensional array where each of the dimensions are the necessary parameters required to perform the multicolor object classification. The first dimension in the array accounts for the redshift step. The redshift grid is equidistant on a $\log(1+z)$ axis. The step size on this logarithmic axis is equal to the step size on a linear grid at $z = 0$ that is the redshift starting value of the color galaxy library. The location of the remaining parameters is free in the sense that it doesn't modify the classification process. In this particular case, the second dimension is for the extinction levels (6 in total), the third field is for the number of SED's composing the spectral library and the fourth dimension accounts for the fitting iterations.

As final result a color galaxy library containing the color indices calculated from the SED's coming from the galaxy library is obtained. This is the starting point of the COMBO-17 multicolor classification process. In the next section, this classification process will be described in detail.

3.2 Object multicolor classification and redshift estimation

The general picture of the multicolor classification process is the following, the objects contained in the survey catalogue are classified into four different classes: stars, galaxies, quasars and white dwarves by using the maximum likelihood statistical estimate (ML). After objects are classified, their redshifts can also be estimated based on a statistical approach that will be explained in the next subsection.

In detail, the multicolor classification carried out by COMBO-17 is done in the following way:

Following Wolf et al. 2000 and 2004, the COMBO-17 survey multicolor classification scheme computes the integrated probabilities of the different object classes c_j and normalizes them to 100% what means that these are the only possible classes of a survey object to fall in. Then the decision estimator has to choose from the four existing object classes $c_i =$ stars, galaxies, quasars and white dwarves. Each object is assumed to belong to one of this classes using the maximum likelihood decision estimator (ML) that is basically the probability of an object to belong to one of the classes mentioned, so the highest likelihood. When the probability of an object to belong to a certain class is higher than 75% then the object is classified, if not, the object remains unclassified.

In addition to the class itself, other physical properties of objects can be derived from the photometric spectra such as stellar population components (model dependent), the age of the object and its star formation rate.

Equation (3.8) is the maximum likelihood probability for the objects to belong to the classes mentioned previously.

$$P(\text{object}|c_j) = \frac{\text{object}}{c_{star} + c_{galaxy} + c_{quasar} + c_{whitedwarf}} \quad (3.8)$$

As mentioned before, the COMBO-17 survey measures the fluxes of the objects in its 17 optical bands plus the 3 ISAAC-NIR bands inside the CDFS and uses the color indices as input of the classification rather than the fluxes themselves with the aim of getting rid of the problem of flux normalization.

The color index (c.i.) is the difference in magnitude of two of the COMBO-17 survey filters and is given by:

$$c.i._{i-j} = m_i - m_j = -2.5 \log(F_i/F_j) \quad (3.9)$$

The errors of the magnitudes measured are then:

$$\sigma_{m_i} = -2.5 \log(1 \pm \sigma_{F_i}/F_i) \quad (3.10)$$

For smaller values of σ , the last equation can be approximated by:

$$\sigma_{m_i} \approx \sigma_{F_i}/F_i \quad (3.11)$$

So that the color index error is:

$$\sigma_{i-j} = (\sigma_{m_i}^2 + \sigma_{m_j}^2)^{1/2} \approx (\sigma_{F_i}/F_i)^2 + (\sigma_{F_j}/F_j)^2)^{1/2} \quad (3.12)$$

This color-based approach is somehow equivalent to the flux-based one with some constraints and assumes that there is a particular base filter (the one with the longest exposure time) free of flux errors that in the case of the COMBO-17 survey is the deeply exposed R-band filter (35ks of total exposure time). The calibration of the filter was based on the spectrophotometric standard stars that lie inside the fields. Their spectra were reduced and compared with the estimated absolute spectrophotometric accuracy comparing several spectra of an external calibrator (HD 49798) obtained during the entire observing run of the CDFS. All color indices are then compared with this free flux error ensuring optimum errors for the colors.

Wolf et al. 2000 show the equivalence between the flux-based and color based classification, obtaining that:

$$\xi \approx \Delta F_k / \sigma_k \quad (3.13)$$

Where ξ is $F_{k,obs} - F_{k,model} / \sigma_{F_k}$.

The maximum likelihood estimations determined for the classification depend strongly on the color indices and their errors (σ_k); both values have to be correctly calibrated. The multicolor classification would fail if the errors are underestimated, for this, errors in the calibration are taken into account by assuming a minimum error for each color index of 0.05 mag what would avoid a wrong maximum likelihood estimate.

Redshift estimation

The redshift estimation is carried out in two different ways, The first is based on the minimum error variance estimator (MEV) that calculates the mean and the variance of the redshift probability distribution and the second is the maximum likelihood (ML). Redshifts are calculated in these two ways simultaneously, because even if MEV provides the best redshift estimation, there are some objects in the survey where no MEV value can be estimated. When objects have an uni modal behaviour, the MEV estimates are almost identical to ML, the problem raises when some survey objects have ambiguities in their color space. This means that instead of having a very well defined non-broad distribution, it happens that the distribution is bimodal or too flat. In this cases there is a flag that is added to the survey catalogue to make notice that the object then will be calculated using another probabilistic estimator, in this case ML. ML will provide a less accurate redshift estimation based on the probability integral under the two peaks of a bimodal distribution and decide then which one is the most likely alternative. When objects have flat distributions objects are usually recognized by the classifier as unclassified and no redshift or a wrong redshift can be provided.

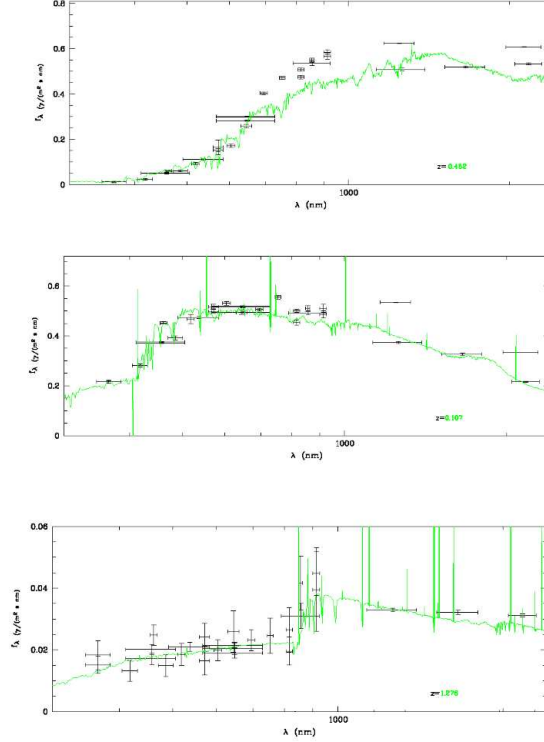


Figure 3.5: Examples of the fitting of spectral energy distributions (SED's) obtained by using the new galaxy template library to the photometry. In the top, a galaxy classified as early-type galaxy. In the top, a galaxy classified as starburst galaxy. Below, the spectra of a galaxy with a strong star forming second burst.

The redshift errors are estimated based on the a-priori knowledge of the Monte Carlo simulations performed by Wolf and Meisenheimer where the performance of the object classification and redshift estimation is tested, depending on the S/N of the photometry which determines both, the classification performance and the completeness of the redshifts of the objects in the catalogue. All this depends of aperture photometry used to establish the spectral shape of the objects (see Section 2.3). The input redshifts are then compared with the recovered estimates. Problems arise when objects are faint as their spectral features are weak and contaminated by the noise.

There are two main error sources, one is when redshift is changing and the second is the magnitude. When redshift is changing the filter set translates into an error that scales as $(1+z)$. That is why all the errors of the COMBO-17 objects are expressed in terms of $\delta_z/(1+z)$. When magnitude

is changing noise is changing too, then the S/N ratio across all the filter fluxes varies what affects the measured SED. Moreover, photometric errors increase inversely proportional to a decreasing flux, the redshift mean errors scale as $\sigma_z/(1+z) \propto 1/F$ being F the mean flux of an object.

Chapter 4

Restframe properties of galaxies in the GOODS-CDFS

In this chapter the galaxy sample and some of its properties such as the redshift distribution and the SED distribution will be shown, as well as the selection criteria used in order to select this galaxy sample.

As next step, the two libraries will be compared in order to find differences in the multicolor classification when the former library is replaced by the two-burst model one.

The two galaxy libraries are two dimensional in the sense that multicolor classification will depend on two independent parameters. The former one is an age-extinction library while the newly developed is a burst strength-extinction one. Both libraries are applied into the optical plus infrared extension dataset into the GOODS-CDFS in order to be consistently compared. Some galaxies show different redshift estimates when the two libraries are applied independently. There are some trends concerning the template fitting that will be discussed.

The inclusion of the NIR data in the COMBO-17 filter set will be discussed too. However, note that no comparison can be made as the analysis would not be consistent because the multicolour classification for the optical data set is only available when the Wolf galaxy library is used to perform classification. The ideal would be to have a classification of the galaxy sample with the new galaxy library in order to compare only the influence of the inclusion of the near infrared filters when combined with the COMBO-17 optical data.

Different properties can be derived from this galaxy sample, such as the restframe luminosities for the galaxies together with their newly estimated redshifts. Red sequence evolution of galaxies can be traced up to $z = 2.2$ and stellar masses of galaxies can be derived.

4.1 The galaxy sample

4.1.1 Sample Criteria

In order to have a complete sample of galaxies where its restframe properties can be derived, selection criteria in order to obtain the most suitable sample of galaxies for analysis was necessary to establish. The first selection criterion in order to have a complete sample of galaxies, was to select those ones with flux measurements both in the optical range and in the three infrared bands (J,H,Ks). It is important to recall that J-band filter measurements do not cover the whole GOODS-CDFS field. As second selection criterion, we selected only the galaxies that are classified just as 'Galaxy' in the multicolour survey catalogue. This, was to get rid of those objects where the classifier cannot provide a clear decision due to difficulties on interpreting the object colors as discussed in section (3.2).

In particular, there are three cases where this can occur according to Wolf's 2003 column catalogue explanation:

- Galaxy (Star?). Where most likely it would be a galaxy at $z \leq 0.2$. It has star colour, but extended shape and $z \leq 0.2$:Overlap in colour space.
- QSO (Gal?). Colour of QSO's, extended shape, low-L AGN or contaminating galaxy.
- Galaxy (Unclj). Colour undecided. Statistically almost always a galaxy.

The last selection criterion was to double-select the sample based in its Ks-band magnitude $Ks\text{-band} < 23$ and selecting simultaneously at $R < 25$ as the aim was to cross-match the K-detected sources with the pre-existing COMBO-17 R-band selected catalogue.

Finally, a sample of ≈ 4300 galaxies in the GOODS-CDFS was obtained. Histograms (4.1,4.2,4.3,4.4) show the distribution of the galaxy sample in terms of SED's and photometric redshift estimated values together with the distribution of its errors.

In order to test the quality of the redshifts obtained, they were compared with spectroscopic redshifts of hundreds of galaxies that were found in the ESO-GOODS/CDFS master compilation catalogue. In Fig 4.6 this galaxies are shown. The ones whose spectroscopic redshift quality is high according to the master compilation catalogue are shown in colors. From FORS2 latest data release, galaxies which quality flag is defined as solid redshift reliability are shown in red. Galaxies whose spectroscopic redshift was obtained using

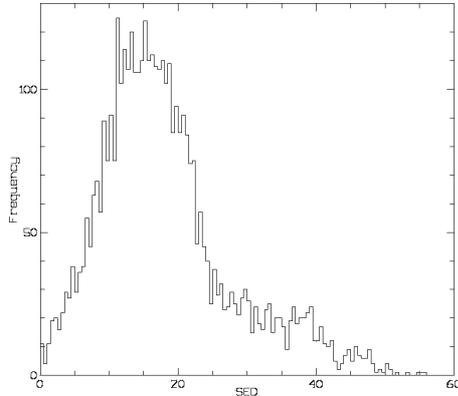


Figure 4.1: SED distribution of the galaxy sample obtained with the COMBO-17 plus its NIR extension multicolor classification scheme.

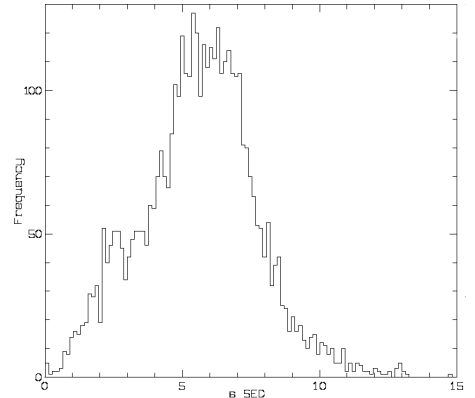


Figure 4.2: SED error distribution of the galaxy sample obtained with the COMBO-17 plus its NIR extension multicolor classification scheme.

VIMOS with quality flags of the 100% and 95% are shown in yellow and pink respectively. This comparison shows that our photometric redshifts are in good agreement with the spectroscopic ones. The scatter from the 45 deg line is ≈ 0.2 dex in the widest area around the line. This can prove that two-burst metallicity consistent models deliver a good redshift estimate for galaxies.

One interesting point would be to see the contribution of red light coming from early-type galaxies to the blue light coming from the late-type ones. Fig 4.5 shows this contribution as a function of look back time ($H_0 = 100\text{km/s}$). The galaxy sample is composed mostly of late-type galaxies (blue gals) that dominate by number each of the redshift bins where the galaxy sample was divided. The old stellar populations that compose the early-type galaxies (red gals) dominate the light in a bigger range locally meaning that has become more abundant towards present days. Their influence and number, decreases when going further back in time until $\approx 3\text{Gyr}$ where the light coming from the old stellar populations of the early-type galaxies becomes prominent once again decreasing for older times until $\approx 6.3\text{Gyr}$ where two peaks show again the raise of an increasing amount of light coming from red galaxies.

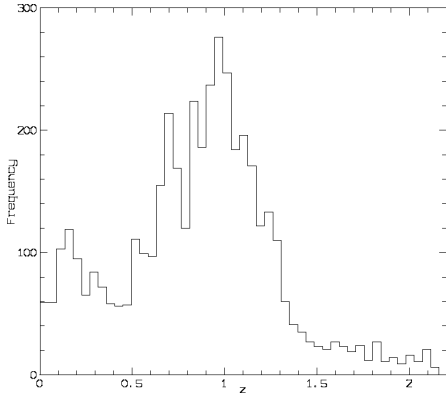


Figure 4.3: Redshift distribution of the galaxy sample obtained with the COMBO-17 plus its NIR extension multicolor classification scheme.

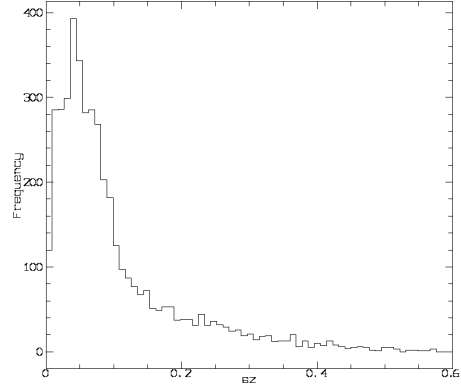


Figure 4.4: Redshift error distribution of the sample obtained with the COMBO-17 plus its NIR extension multicolor classification scheme.

4.1.2 Comparison between the new galaxy library and the Wolf galaxy library

The new galaxy library was built in a way that could reproduce closely the results delivered by the Wolf galaxy library (because of its redshift accuracy) but this time including a star forming scenario that would be more realistic in order to obtain galaxy properties that would allow the COMBO-17 survey to deliver properties of galaxies such as stellar masses of galaxies. Although for the majority of the galaxies in the sample redshifts are the same the results delivered by both libraries show differences in redshift that deserve a closer look in order to understand the effect of the second star forming burst.

In Fig 4.7, the comparison between both redshift estimations is shown. The y-axis z shows the redshift estimations for the galaxy sample with the two-burst galaxy library that I will call the new galaxy library. In the x-axis z_{old} , the redshift estimations with the single burst galaxy library are shown, and I will refer to it as the Wolf galaxy library.

As mentioned before, there are considerable differences in redshift values for a certain amount of galaxies. There are three interesting groups of galaxies that will be discussed in detail. The first group is the one of the galaxies with a very high increase in redshift value compared with those delivered by the Wolf galaxy library. The second group is the one of the galaxies whose redshift values increase but not as dramatic as the first group. The last group is the one of the galaxies that with the new multicolor classification obtain a lower redshift value.

It is interesting to divide the galaxy sample according to their given SED

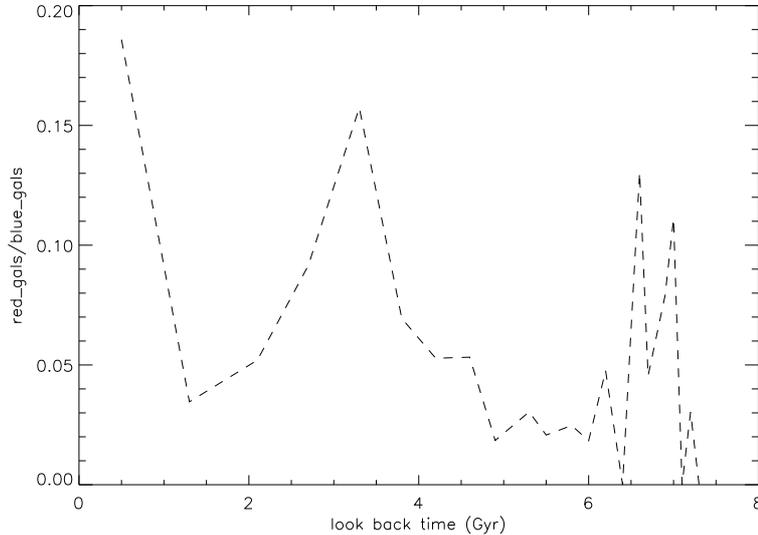


Figure 4.5: Fraction of red galaxies relative to the blue galaxies as a function of look back time in Gyr. The sample galaxies are selected in $K < 23$ and $R < 25$ and the redshift range is $z = 0 - 2.2$. Blue galaxies (late-type) dominate in number each of the redshift bins of the sample. Red galaxies (early-type) are more prominent locally and at intermediate redshifts. At $z \geq 1$ a double peak is noticeable suggesting that early type galaxies were already in place at these redshifts.

in different SED bins (Fig 4.9). It will be possible to follow the formation of the three subgroups mentioned above. It would be interesting to find some features that make us understand how the multicolor classification performed in both ways chooses the best template to fit the galaxies in the sample.

In Figure 4.9 galaxies are ordered in SED bins from late-type (starburst galaxies) to early-type galaxies. It is found that the galaxies have the biggest differences in redshift in the first SED bins ($\approx 10\%$ of the galaxy sample), what is expected due to the effect of the second star forming burst that is stronger in the first SED's. This effect decreases when moving towards higher SED's as the amount of young stars formed during the second burst decreases when SED number increases. Thus, the differences in redshift estimation become less common for galaxies with higher (redder) SED numbers.

The spectra of some of the galaxies with noticeable difference in redshift is shown as example in the following figures fitted by both different galaxy libraries.

For the galaxies lying in the first SED bins with a very high difference in redshift ($z \gg z_{old}$), the former library fits the spectra with young SED's and higher extinction levels in comparison with the new galaxy library that

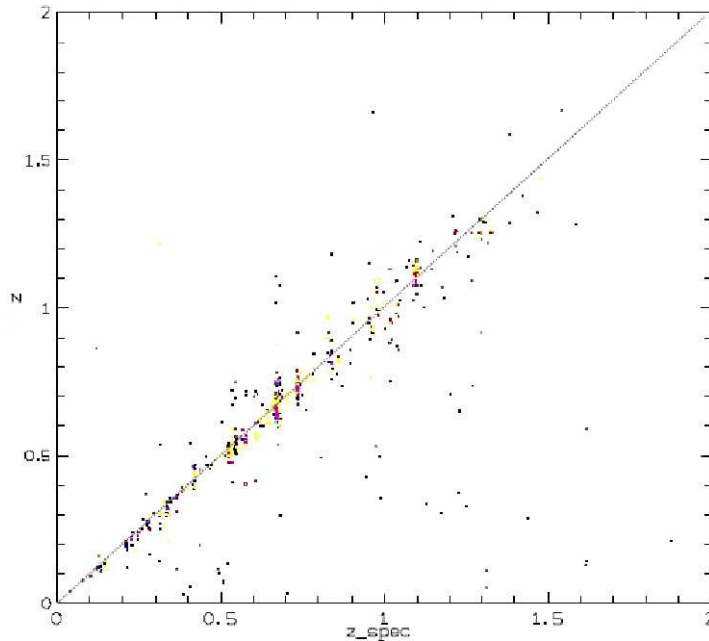


Figure 4.6: COMBO-17 photometric redshifts vs. Spectroscopic redshifts from VIMOS and VVDS. Source of spectroscopic redshifts: ESO master compilation catalogue. In red, the FORS2 spectroscopic redshifts defined as solid redshift reliability, in yellow the VIMOS spectroscopic redshifts with a reliability quality flag of 100%. In pink, VVDS spectroscopic redshifts with a 95% reliability quality flag.

fits the spectra with a template that has a big amount of blue stars and a lower extinction level. Although the Wolf library is based in age and the new library is based on strength of the second burst, it is possible to compare them in terms of blue or red galaxies. As mentioned before, this tendency begins to be less prominent when going towards higher SED's.

As an example, two galaxies and their SED's are shown together with the best fit provided by both galaxy libraries (Fig 4.10). For the galaxy with COMBO-17 ID-number 32819, the best fitting template according to Wolf's galaxy library is the one of a very young galaxy with an extinction A_B slightly higher than the one given by the new galaxy library, the redshift estimate value delivered by the Wolf galaxy library is $z_{old} = 0.0592$ and the one delivered by the new galaxy library is $z = 1.671$. This trend of 'redder' SED's given by the Wolf library compared to the given by the new galaxy library begins to vanish when going to higher redshift. As shown in the examples, both templates try to fit the galaxy spectra. The overall shape of the spectra is reproduced by both templates that try to fit the 4000\AA break and then follow the behaviour of the photometric SED even though they don't really fit the filters. It is important to remind in this point that the

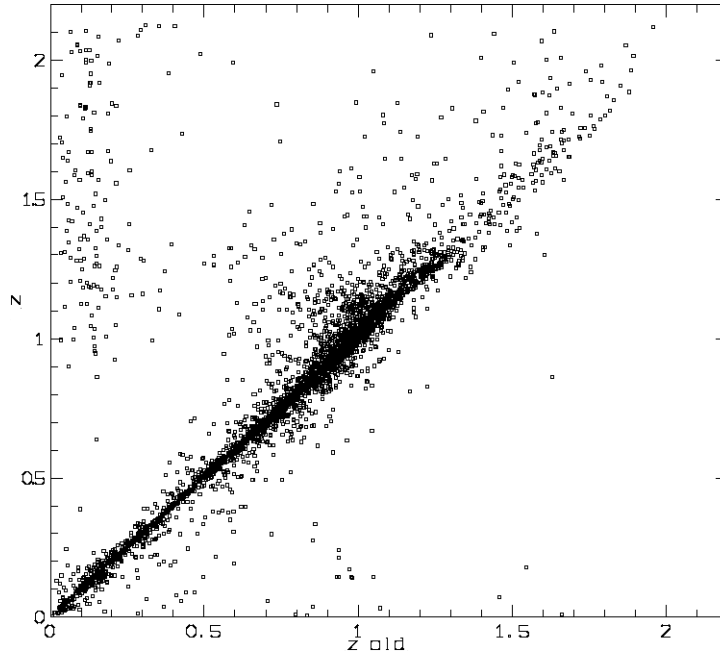


Figure 4.7: Comparison between the photometric redshifts obtained using both galaxy libraries. It is noticeable the difference in redshift values for some of the galaxies in the galaxy sample. There are three subgroups of galaxies that will be analysed in more detail: Galaxies with a **very high increase** in redshift. Galaxies with **increase** in redshift and galaxies that **decrease** their redshift values when compared with the redshift estimates obtained using the Wolf galaxy library. Both estimations were carried out in the same data set COMBO-17 optical data plus its GOODS/ISAAC-NIR extension in the GOODS-CDFS.

survey is color based so the main aim is to reproduce the overall shape and not to really to fit the filter set.

The second example shows a galaxy with a strong drop from the optical to the near infrared range. Such galaxy spectra is difficult to fit for both procedures failing on reproducing the overall shape of the galaxy.

For the galaxies whose redshift estimation is higher, $z \geq z_{old}$, the dust reddening of the galaxies has slight variations or remains the same. There is a trend when going from low SED's to higher SED's. The new galaxy delivers fits that are somehow redder than the ones delivered by the former library. Figure 4.11 shows two galaxies examples of this group as an example.

This trend was found just by statistics, there is no real reason to assure that this is expected just taking in account the difference in the star forming scenarios. Spectra of several objects belonging to this group were examined by comparing both fits and finding as a result this particular trend. This means that the new template fitting classifies galaxies as more evolved

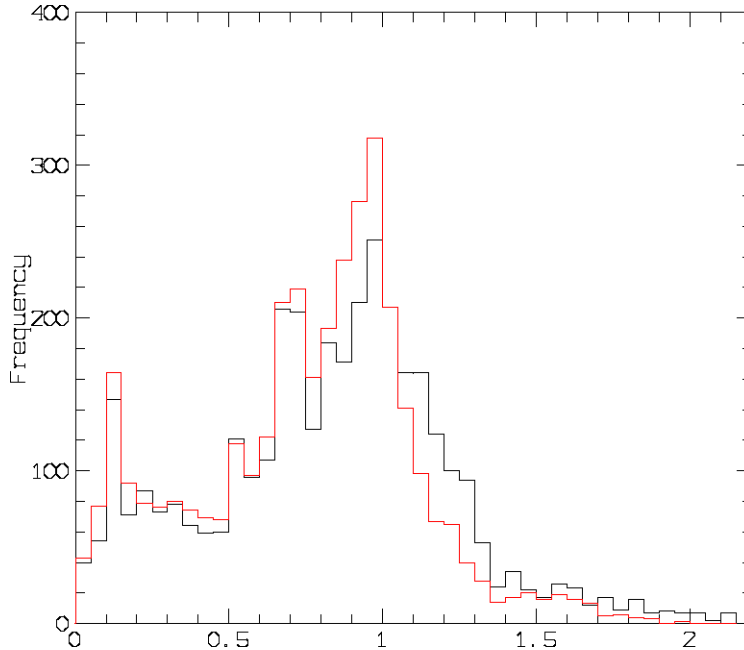


Figure 4.8: In black, the distribution of galaxies according to the new galaxy library is shown. In red, the distribution of the galaxies according to the Wolf galaxy library. Galaxies redistribute in redshift in the two different multicolor classifications. Local maxima are placed in the same positions at $z \approx 0.13$, $z \approx 0.7$, $z \approx 1.0$. The black histogram shows a small excess of galaxies in the interval $1.1 \leq z \leq 1.4$.

galaxies than with the former galaxy library.

The last group is the one of those galaxies which redshift estimates are lower than the ones obtained with the Wolf galaxy library. Both templates reproduce quite well the overall shape of the galaxies in general. One of the exceptions is shown as an example in Fig 4.12. The galaxy #41424 is better fitted by the new galaxy library as it reproduces the increase of the galaxy flux in the infrared wavelength range. There are some galaxy spectra that both libraries are not capable to fit, this is the case of the galaxy #24016 fail on reproducing the increase of flux coming from the last optical narrow band filter of the survey.

It is important to remember that even if the Wolf galaxy library delivers very accurate redshifts, the templates delivered do not have a realistic meaning because of its one burst star formation rate. One of the aims of this work is to constrain the dust reddening dimension of the library by having a more realistic star forming scenario plus the addition of the NIR filter set to the survey.

The inclusion of NIR data to an optical survey provides information about the old stellar population that is contained in the galaxies. With this inclu-

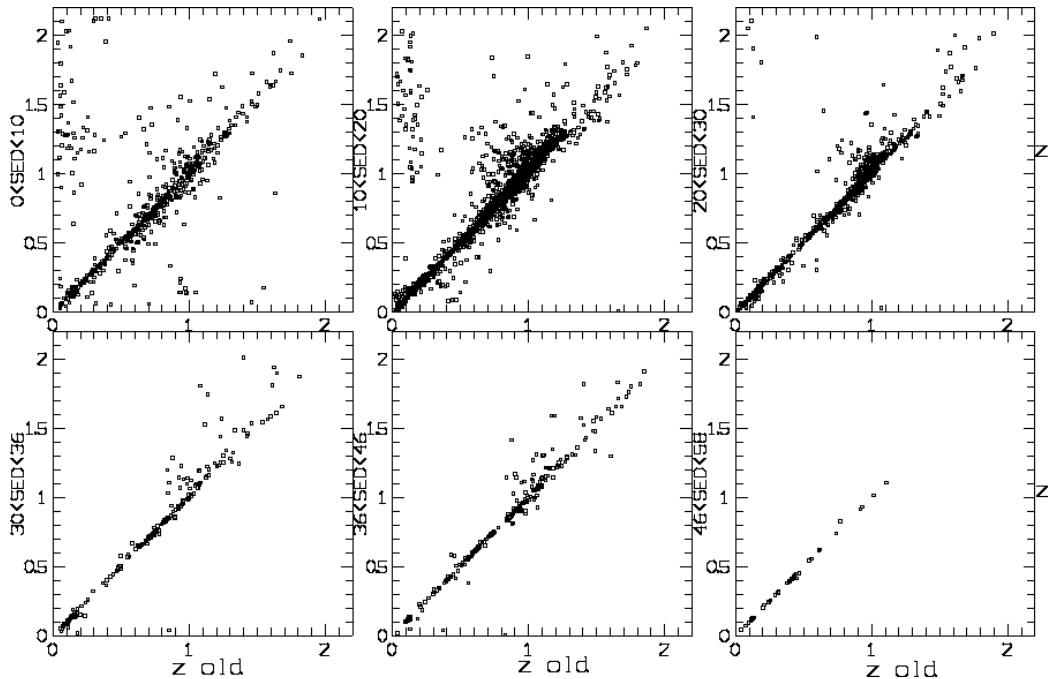


Figure 4.9: Galaxy sample shown in different SED number bins. The effect of the second burst is highly noticed in the first SED bins (bluer). Its effect decreases with increasing SED number (redder).

sion, it is possible to obtain information up to the wavelength range where the old population dominates the spectra. Another advantage of the NIR inclusion is to reduce the uncertainty of measurements as more filters are added to the original filter set allowing to increase the color space and constrains in a higher degree the properties of the galaxies, like the age-extinction (or strength-extinction) degeneracy existent in the survey multicolor classification.

4.2 Restframe luminosities

Restframe luminosities are calculated by using the measured photometry of each of the objects in the survey and by calculating its distance modulus under a cosmological model. To calculate the distance modulus in this particular case, the Λ CDM Universe is adopted, being $\Omega_m = 0.3$, $\Omega_\lambda = 0.7$ and taking the Hubble constant value of $H_0 = 100$ km/sMpc. This value for H_0 is taken by convention by the COMBO-17 survey. In this particular case, it is simply taken to make easier further comparisons of the results obtained with other already published which Hubble constant value is $H_0 = 100$ km/sMpc

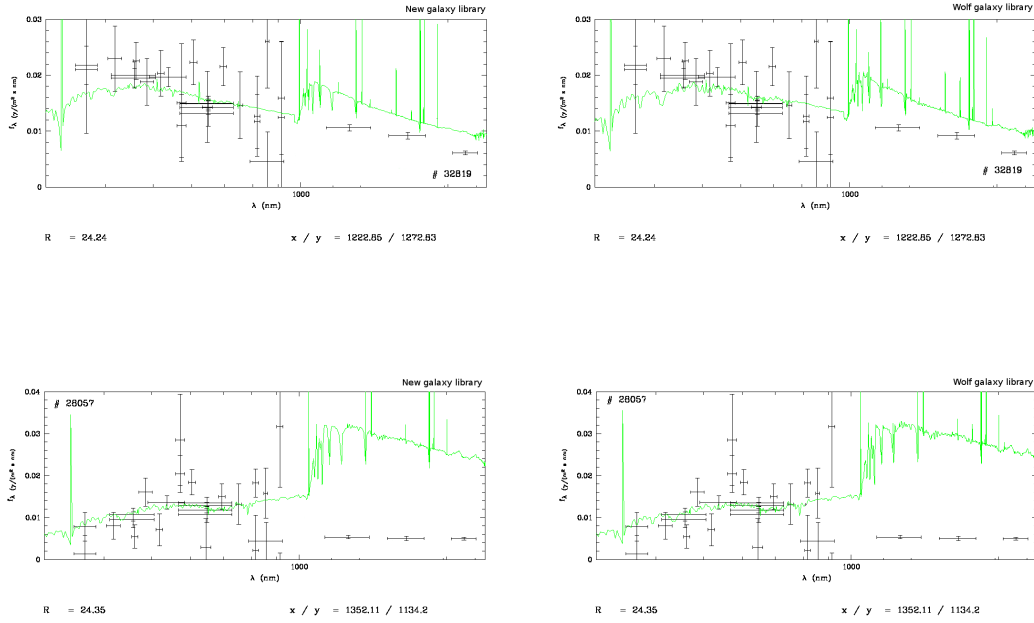


Figure 4.10: Galaxies with very high difference in redshift estimation: For the galaxy #32819, the estimated age according to the Wolf galaxy library is $age = 99.33\text{Myr}$ and $A_B = 0.318$ delivering a redshift value of $z_{old} = 0.0592$. According to the new galaxy library, this galaxy has a blue young stellar population of ≈ 5.81 times the amount of stars formed during the first star forming burst, $A_B = 0.210$. Delivering a redshift value of $z = 1.671$. For the galaxy #28057, the estimated age according to the Wolf galaxy library is $age = 199.94\text{Myr}$ and $A_B = 1.055$ delivering a redshift value of $z_{old} = 0.187$. According to the new galaxy library, this galaxy has a blue young stellar population of ≈ 1.30 times the amount of stars formed during the first star forming burst, with a dust reddening of $A_B = 0.422$, the delivered redshift estimate value is $z = 1.809$.

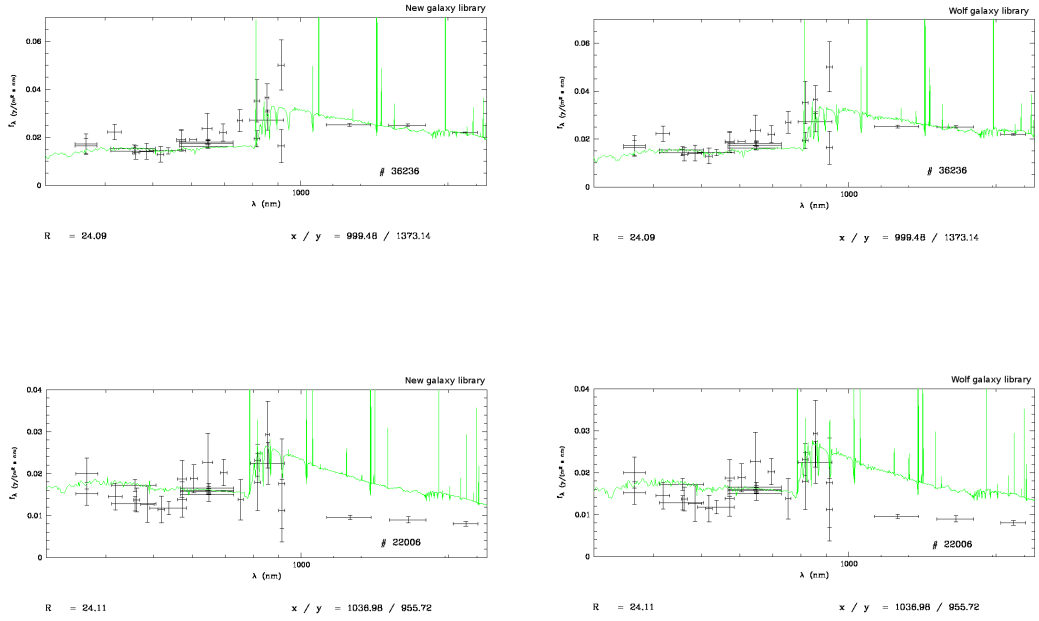


Figure 4.11: Galaxies classified with higher redshifts than before: For the galaxy #36236, the estimated age according to the Wolf galaxy library is $age = 57\text{Myr}$ and $A_B = 0.442$ with a redshift value of $z_{old} = 0.897$. According to the new galaxy library, this galaxy has a blue young stellar population of of ≈ 0.418 times the amount of stars formed during the first star forming burst, $A_B = 0.148$ and a redshift value of $z = 1.179$. For the galaxy #22006, the estimated age according to the Wolf galaxy library is $age = 50.82\text{Myr}$ and $A_B = 0.479$ with a redshift value of $z_{old} = 0.838$. According to the new galaxy library, this galaxy has a blue young stellar population of of ≈ 14.29 times the amount of stars formed during the first star forming burst, $A_B = 0.42$ with a redshift value of $z = 1.107$.

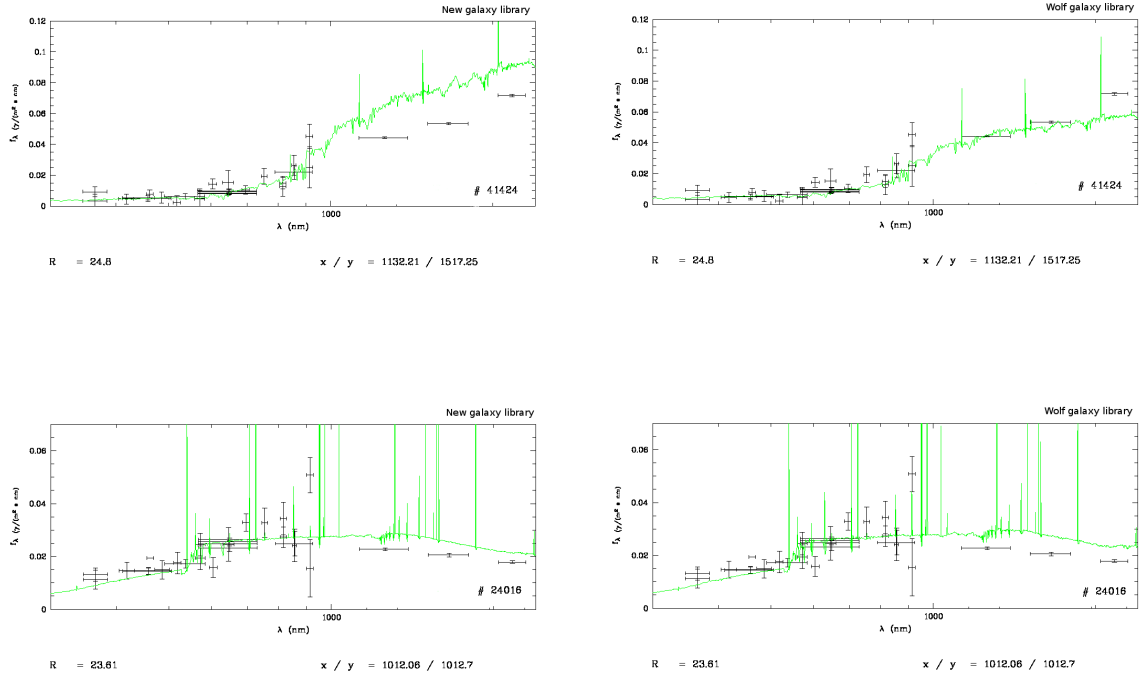


Figure 4.12: Galaxies with lower redshift estimates: For the galaxy #41424, the estimated age according to the Wolf galaxy library is $age = 2.505 \text{ Gyr}$ a dust reddening value of $A_B = 0.479$ and a redshift estimate of $z_{old} = 1.268$. According to the new galaxy library, this galaxy has a blue young stellar population that is basically negligible (less than 0.001 times the amount of stars formed during the first star forming burst), but it is equivalent to an age of 3.25 Gyr with an extinction value of $A_B = 0.546$ and a redshift value of $z = 1.025$. For the galaxy #24016, the estimated age according to the Wolf galaxy library is $age = 92.5 \text{ Myr}$ with a dust reddening value of $A_B = 1.403$ and a redshift estimate of $z_{old} = 0.589$. According to the new galaxy library, this galaxy has a blue young stellar population of of ≈ 8.44 times the amount of stars formed during the first star forming burst, $A_B = 1.638$ and a redshift value of $z = 0.449$.

(e.g. Bell, et al.2004).

Technically, let's recall that all spectral galaxy templates are calculated at $z = 0$, thus, it is necessary to apply the K-correction in the following way: First, restframe luminosities within the wavelength range covering from the U-Ks band, are calculated by placing the best-fitting redshifted template of each galaxy into the observed SED. If a restframe band is out of the original wavelength range, luminosities are calculated by extrapolating the SED outside the range.

In other words, the best-fitting template is placed into the observed SED relating the measured broadband that is closer to the given redshifted rest-frame band of interest. A K-correction table is used and basically it looks like the colour library designed previously, the difference is that instead of having observed-frame - observed frame color indices, now this K-correction table has rest-frame - observed-frame colors.

The errors for the luminosities take in account two different issues, a minimum error for absolute calibration of 0.1 mag. The error of mag-best (that defines the total magnitude of the galaxies) is provided by SExtractor. The second issue taken in account is the error of the nearest observed-frame band which drives the normalisation of the template.

The errors of the restframe colours are added quadratically from the two observed-frame bands near the two rest-frame bands combined in the colour index and a 0.1 mag error added in again. Aperture correction is not used as it does not affect the colour in the absence of colour gradients. (detailed description in the COMBO-17/CDFS catalogue, Wolf, et al. 2003).

4.3 Red sequence evolution of galaxies until $z=2.2$

The trace of the red sequence evolution of galaxies until $z = 2.2$ provides an important proof that supports the hierarchical galaxy formation theory. One of its predictions states that the red sequence is already well established at $z \approx 1$ when star formation in galaxies is being quenched somehow at this redshift.

It is possible to find the evolutionary trace of our galaxies in terms of their restframe colors and absolute magnitudes. Although the galaxy sample is small, it is possible to try to find the establishment of the red sequence with the help of the 24μ data from the Far Infrared Deep Extragalactic Legacy Survey (FIDEL).

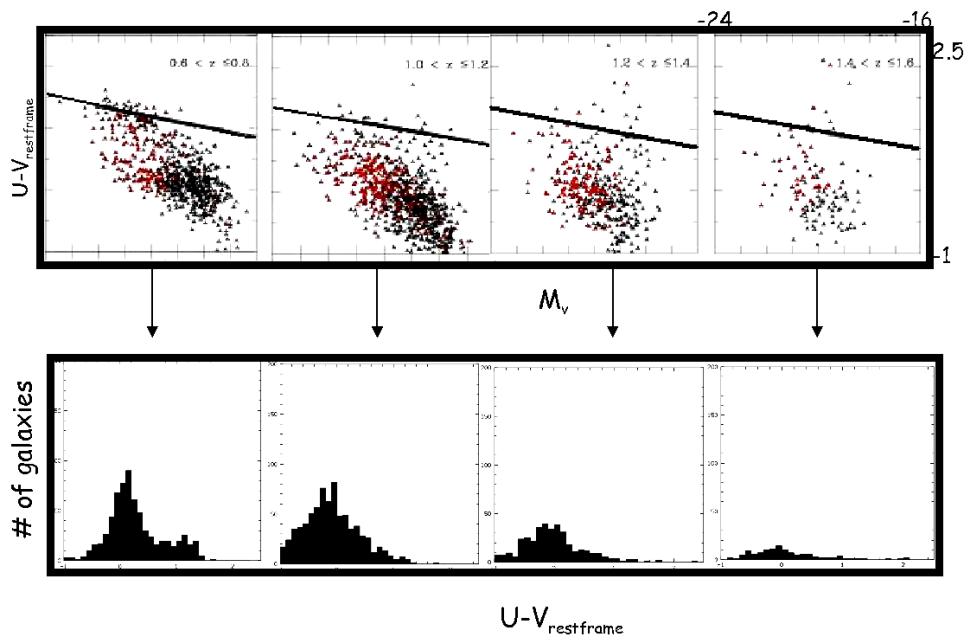


Figure 4.13: Galaxy sample divided in redshift bins as a function of their restframe colors $U - V$ and its absolute magnitude M_v . In red, galaxies detected by the COMBO-17 survey plus its near infrared extension that are also detected with the 24μ data from the FIDEL survey (Photometry made by Dr. X. Zheng). The red sequence is well established since $z \approx 1$ while is lost beyond $z \approx 1$. The histograms show the distribution of the galaxy sample as a function of their restframe colors $U - V$. The bimodality (peaks of blue and red galaxies) is noticeable in the first redshift bin while it becomes diffuse and then disappears beyond $z \approx 1$.

In Fig. 4.13 is shown the distribution of the sample galaxies in four different redshift bins. In red, the galaxies that are detected by the COMBO-17 survey plus its infrared extension and that at the same time are 24μ detected. The solid line is the division between red sequence galaxies and the ones that belong to the blue cloud (Bell 2004). The first two redshift bins $0.6 \leq z \leq 0.8$ and $1.0 \leq z \leq 1.2$ show a well established red sequence of objects being this noticeable since the 24μ detected galaxies do not belong to the red sequence. This means that galaxies that are falling into the red sequence are passively evolving with time. Beyond $z \geq 1$ the red sequence is not present any more, unfortunately it is not possible to confirm the lose of the red sequence of galaxies beyond this redshift as the data sample is limited by the few amount of galaxies found at this redshifts.

The histograms show the distribution of galaxies of the sample, the first histogram belonging to the first redshift bin $0.6 \leq z \leq 0.8$ shows the bimodal distribution of the galaxies. The first peak (blue peak) contains star forming galaxies while the second peak (red peak) contains those galaxies which star formation process is finished or galaxies in the way to finish their star formation processes. At this point would be interesting to estimate the total SFR of this galaxies in order to distinguish which of them have still on-going star formation and which have already turned the process off. This calculation was not performed as it would be part of another analysis that at the end was not carried out.

As a further step, the evolution of the galaxy luminosity function can be studied for this galaxy sample up to $z = 2.2$ as well as the total luminosity density from the local Universe up to $z = 2.2$.

4.4 Stellar mass estimation

The aim of this work was to improve the the already estimated stellar masses for the galaxies in all the COMBO-17 fields (Borch, et al. 2006). The idea was to estimate stellar masses using the multicolor classification for this small galaxy sample and then apply it to the entire five observed fields. In parallel, the library developed in this work was successfully tested in the Chandra Deep Field South as well as in the Abell-901 field.

The first attempt was to estimate the stellar masses directly from the PEGASE 2.0 output files by taking the total mass of the objects generated during the PEGASE2.0 run: stellar masses (M^*), masses for neutron stars (M_{NS}) and masses from white dwarves (M_{WD}). Afterwards, all of them were added up and multiplied by the star formation rate delivered by the code in each of the time steps:

$$M' = \Sigma_i(M_* + M_{NS} + M_{WD}) \times SFR(\text{per timestep})dt \quad (4.1)$$

getting finally,

$$M_{\text{stellar}} = cM' \quad (4.2)$$

Where c is a normalization factor.

For some reason, when obtaining stellar masses in this particular way the values obtained were wrong. After several checks the conclusion was that PEGASE2.0 when used in the way it was delivers inconsistent values for mass to light ratios. One possible reason could be that when manipulating the SFR parameters in order to deliver such high values of gas mass for the highest star forming bursts, the star formation history calculated for each of the time steps might be wrong, even though the generated galaxy template spectra is correct.

I decided to estimate the stellar masses with an already known method. In particular, following Borch et al. 2006 with some modifications in order to make the technique suitable to my work. The method in general is the following (Borch et al. 2006):

Galaxies are classified under the COMBO-17 frame-work. A galaxy library is provided in order to get spectral galaxy templates in the same way as described in Chap 3 Sec 3.1. In this case, a star formation rate with three different components is used, multicolor classification and redshift estimation are performed. Redshift estimates are less accurate than the ones obtained when using Wolf's one single burst library 2003.

Borch's library 2006, uses a star forming scenario consisting on a star formation rate with three components. To reproduce the old population, an exponentially decaying star forming burst with e-folding time of 1 Gyr is first started up (component a) following a constant star formation rate since the initial burst (component b). A second star forming burst in the recent past (60 million years ago) is included too (component c). Its exponential decay time is kept constant, $\tau_c = 10^8$ yrs. Bluer galaxies are generated by increasing the relative amount of recent star formation by the ratio of its components c/a .

In order to avoid the redshift accuracy issue mentioned before, the classification process is divided in two parts: First, objects are classified and redshifts estimated using the Wolf galaxy library. Due to its non-realistic one single burst history it cannot provide with real values of stellar masses. Therefore, after classification is performed, stellar masses of all galaxies and their uncertainties are obtained by fitting the photometric SED's with the set of templates provided by Borch 2006.

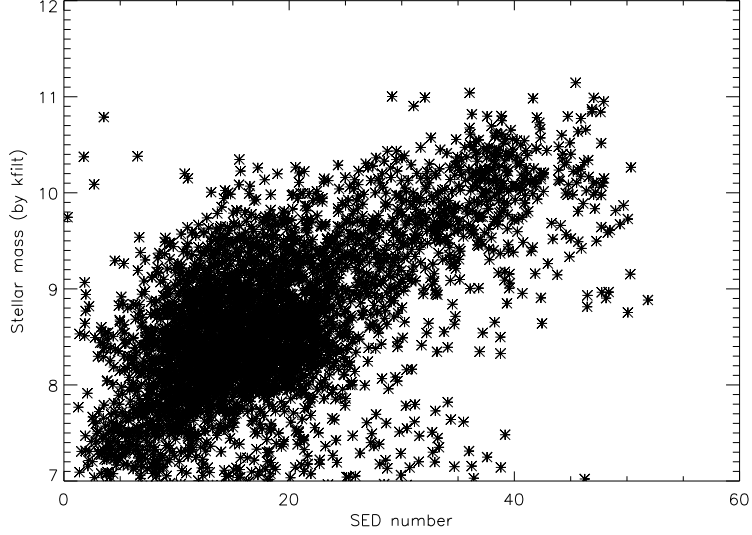


Figure 4.14: Distribution of galaxy stellar masses depending on its SED derived using the color method proposed by Borch et al. 2006.

The following is the equation that describes the mass estimation depending on the redshift and the fitted SED's:

$$h_{70}^2 \frac{M}{M_{\odot}} = \frac{f_{816} \eta_{tot} 4\pi D_L^2 (1+z) \frac{hc}{\lambda} \int Q_{\lambda} d\lambda}{\sum_{k=a,b,c} \frac{k}{m_k} F_{\lambda,k} \int Q_{\lambda} d\lambda} \quad (4.3)$$

Equation 4.3 delivers the stellar mass of any galaxy with observed values f_{816} , η_{tot} that is the Kron magnitude factor given by SExtractor when building the catalogue, $F_{\lambda,k=a,b,c}$ is the total luminosity, D_L is the luminosity distance, Q_{λ} is the spectral response of the system, given by the transmission curve of the 816 filter and the quantum efficiency of the CCD.

To deliver the sample stellar masses, the classification process was not modified as in Borch et al. 2006 due to the good quality of the redshifts estimated with the new galaxy library.

The equation 4.3 was used to deliver the masses with some modifications as the reddest filter in our case is the Ks-band. The numerical transmission curve used in this estimation is the one for the Ks-band provided by the ISAAC user manual.

In order to compare the stellar masses obtained by using Borch et al 2006, stellar masses were also estimated using the existing correlation between restframe optical colors and stellar mass-to-light ratios that is independent of star forming history parameters such as dust content and metallicity (Bell & de Jong 2001, Bell et al. 2004).

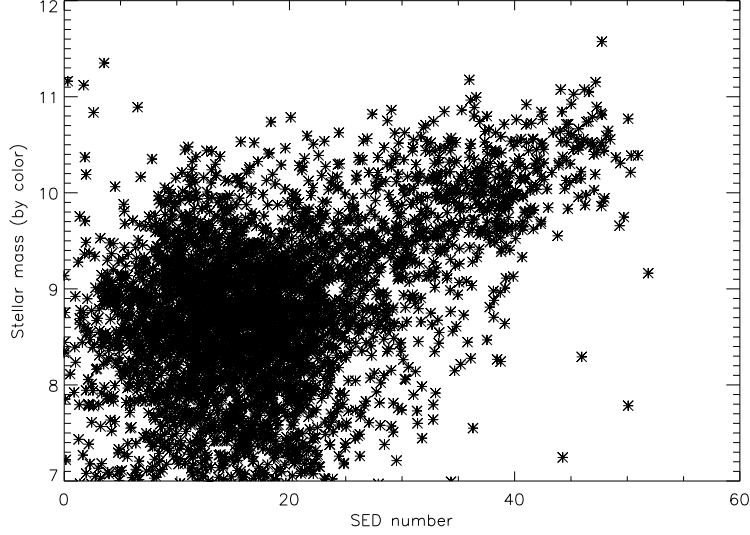


Figure 4.15: Distribution of galaxy stellar masses depending on its SED derived using the color method proposed by Bell et al. 2004.

Based on the existing color-mass to light correlation, (Bell et al. 2005) estimate stellar masses using the rest-frame B and V band magnitudes:

$$\log_{10}\left(\frac{M}{M_{\odot}}\right) = -0.4(V - 4.82) + [-0.628 + 1.305(B - V) - 0.15] \quad (4.4)$$

Where the last term -0.15dex is a conversion factor when using a Kroupa IMF as in this case.

Calculating stellar masses in such a way provides a rather quick and easy way to compare the stellar masses using the modified Borch technique.

In Figs (4.14,4.15) the distribution of stellar masses depending on its SED type is shown for both methods. Most massive galaxies are located in the reddest SED's with the exception of some galaxies that look red but their stellar mass is $\approx 10^9 M/M_{\odot}$ probably dwarf galaxies.

In Figs (4.16,4.17) the stellar masses of the galaxy sample as a function of their rest-frame color index U-V is shown for different redshift bins. The black line indicates the separation of red sequence from blue cloud galaxies, proposed by Bell et al.(2004), after conversion into the $M_{stellar} - (U - V)_{rf}$ plane:

$$(U - V)_{rf} \geq 0.227\log_{10}(M_{\odot}) - 1.16 - 0.352z \quad (4.5)$$

When using Bell, et al. 2004 color method in order to estimate stellar masses in galaxies, it is found that at $z \approx 1$, when galaxy assembly begins (Section 3.4) the red galaxies with masses higher than $10^{10}M_{\odot}$ are the 68% of the total number of early-type galaxies (Fig 4.17). In contrast, using Borch et al. 2006, it is found that these red galaxies that are passively evolving are the 76.8% of the massive red galaxies (Fig 4.16). This means that galaxies with masses higher than $10^{10}M_{\odot}$ have not yet completed the build-up of the stellar mass at this redshift.

Estimating masses with the modified Borch et al. 2006 stellar mass estimation technique gives a higher number of galaxies passively evolving at $\approx z = 1$. Borch et al.2006, find that the 60% of the massive galaxies are assembling at this redshift and that early-type galaxies constitute the 60% of the total number of massive galaxies. Unfortunately our sample is quite small and it is not possible to have a robust sample of galaxies in the CDFS. It is restricted by the fact that the GOODS-CDFS field does not have infrared measurements for the three different bands as not all of its sub-fields have H-band measurements what limits our galaxy sample even more.

One solution for the sample robustness would be to combine this galaxy sample with the ones that will be obtained further in the rest of the COMBO-17 fields when its infrared extension is finished in its totality. The stellar mass function can be derived for this galaxy sample up to $z = 2.2$ allowing to study the stellar mass density of galaxies up to the present days and confirming the increase of stellar mass density at $z \approx 1$

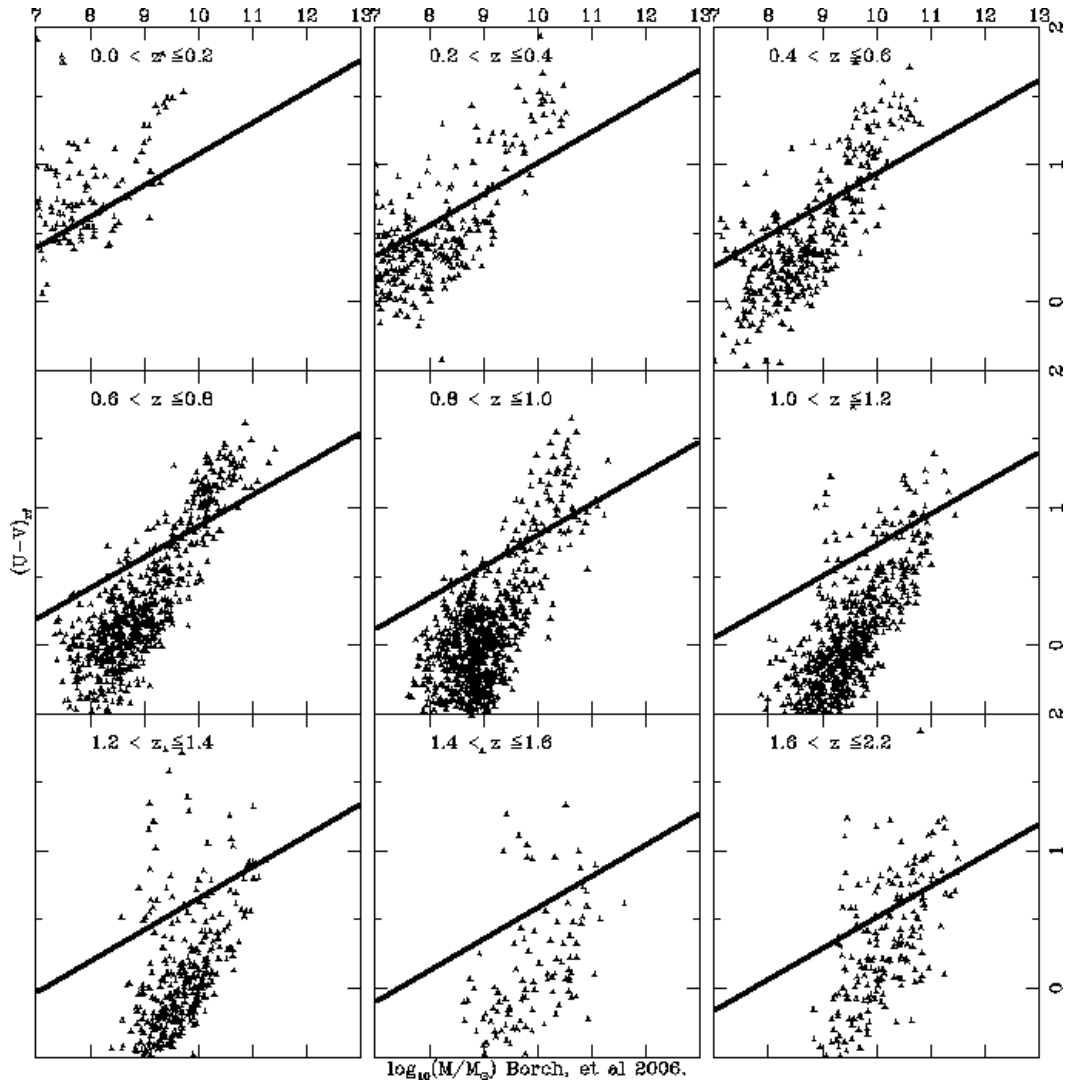
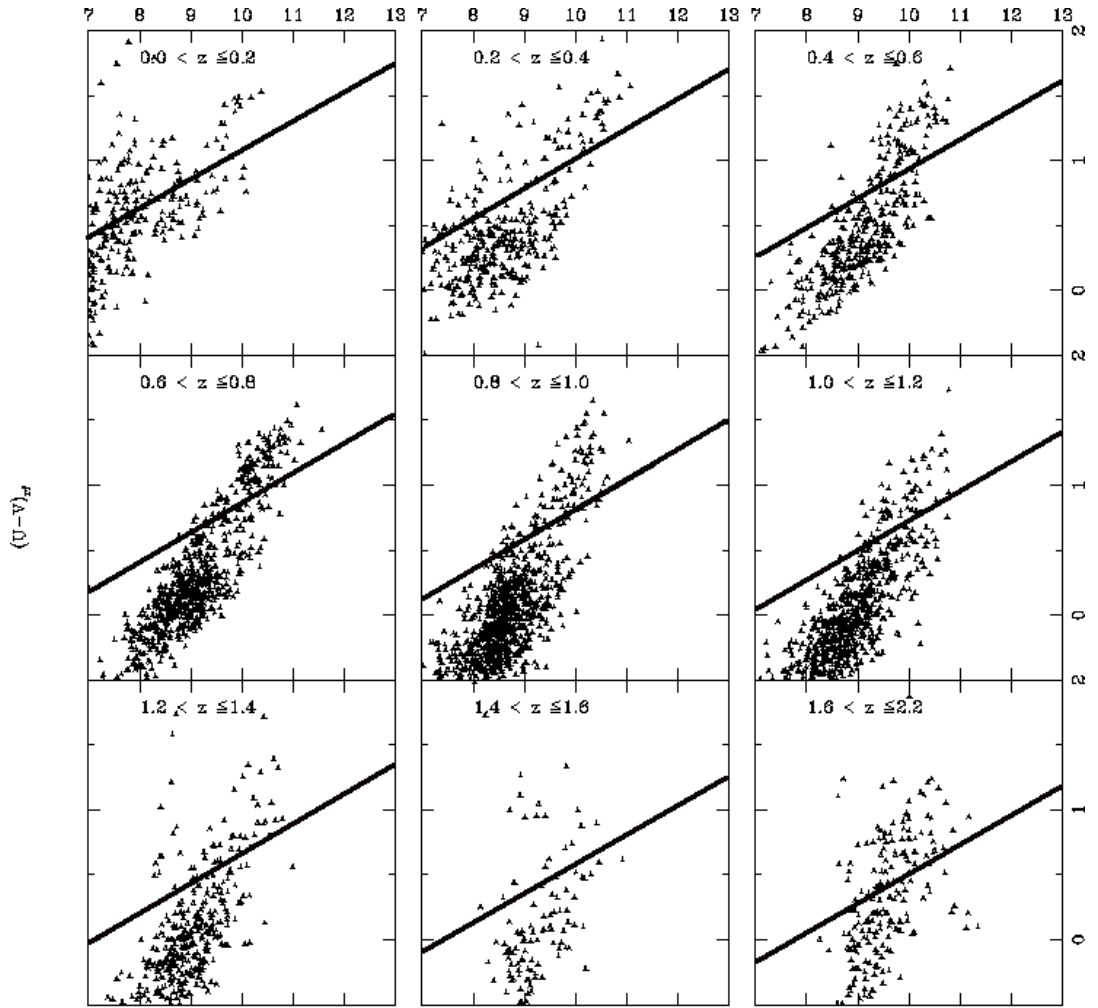


Figure 4.16: Rest-frame U-V color as a function of the stellar mass proposed by Borch et al. 2006 for different redshift bins. The black line divides the blue cloud galaxies from the red sequence ones (Eq 4.5). Assembly of early-type massive galaxies begins at $\approx z = 1$ as predicted by the hierarchical evolution model.



$\log_{10}(M/M_{\odot})$ Bell, et al 2004.

Figure 4.17: Rest-frame U-V color as a function of stellar mass using the optical colour method from Bell, et al. 2004 for different redshift bins. The black line divides the blue cloud galaxies from the red sequence ones (Eq 4.5) Assembly of early-type massive galaxies begins at $\approx z = 1$ as predicted by the hierarchical evolution model.

Chapter 5

Conclusions

In terms of the COMBO-17 survey technical improvement there are two big improvements that were done in this work that can be mentioned, the inclusion of three infrared bands to the survey filter set in the GOODS-Chandra Deep Field South and the development of a new spectral galaxy template library that allows to classify objects in the survey field with a more realistic approach and determine redshifts in a more accurate way acting together with the filter set extension.

The inclusion of the near infrared data to the survey filter set, provided the opportunity of extending the survey wavelength regime up to redshift 2.2 allowing the survey to measure the light coming from the old stellar populations of the galaxies in its fields. Being able to do this, the stellar masses of galaxies can be estimated as the main contributors to the galaxy mass are the old stars populating the galaxies.

The new filter set also provides a tool for better constrain the photometric measurements performed before just with the optical filterset.

This combined together with the design of the new galaxy template library suitable to operate in the mentioned wavelength range allows the multicolor classification of the survey to improve its classification procedure providing with more accurate redshift estimates and constraining the star formation histories of the galaxies in a better way than the former filter set and the former galaxy template library.

Important properties of galaxies can be derived from this two technical improvements. In one hand, now it is possible to trace the restframe colour evolution of the galaxies up to a redshift where important tests concerning galaxy evolution can be made. It was possible to confirm that galaxies begin to assemble at $\approx z = 1$ what it is one of the main predictions of the hierarchical galaxy evolution theory.

It was possible to estimate stellar masses by two already existing different

methods assessing that massive galaxies do not begin to assemble until $\approx z = 1$ and that this assemble is not yet fully complete at this redshift.

As a future work, it would be interesting to develop other galaxy template libraries that take other physical parameters into account instead of using a closed box model to create galaxy evolution scenarios where accretion or outflows are taken into account in order to provide with an even more realistic multicolour classification tool.

To keep extending the filter set towards other wavelength ranges would help to get a better picture of the stellar populations in galaxies and of its evolution during cosmic time.

Bibliography

- [1] Bell E. & de Jong,2005, ApJ, V.625, 1, pp. 23-36
- [2] Bell,E. et al, 2004, ApJ,V.608, 2, pp. 752-767
- [3] Bell E. & de Jong,2001, ApJ, V.550, 1, pp. 212-229
- [4] Bertin,E. SExtractor user manual V.2.5
- [5] Borch,A.,2006, PhD thesis, Evolution of stellar mass density since redshift 1.0.
- [6] Borch,A. et al, 2006, A&A, V.453, 3, pp. 869-881
- [7] Carroll,B.,Ostlie,D. 1996,'An Introduction to Modern Astrophysics'
- [8] Kauffmann, G. et al. 2003, MNRAS, 341, 54
- [9] Madau,P., Pozzetti, L. & Dickinson, M. 1998, ApJ, 498, 106
- [10] Pei,Y. 1992, ApJ, V.395, pp. 130-139
- [11] Vanzi,L., Hunt L. K., 2002, A&A 390, 481-489
- [12] Wolf C., Meisenheimer K. et al. 2003, A&A, V.401, pp. 73-98
- [13] Wolf,C,2003, RevMexAA, Vol. 17, pp.247
- [14] Wolf C. et al. 2004, A&A, 421, pp. 913-936
- [15] <http://www.eso.org/science/goods/releases/20050930/releasenotes>

Part II

Contents

Introduction	50
1 The N-body6 GPU code	57
1.0.1 The Hermite integration method	58
1.0.2 Hierarchical time steps	60
1.0.3 The Ahmad - Cohen scheme	61
1.0.5 N-body units	63
2 The Virgo cluster tidal field	65
2.1 The field tidal forces	67
2.2 Eccentric orbit	69
2.2.1 Tidal radius	70
2.2.2 Oort Functions	71
2.3 Equations of motion of the galaxy within the clusters potential	72
3 Initial conditions: Galaxy Model	77
3.1 The halo distribution function	77
3.2 The bulge distribution function	78
3.3 The disk distribution function	79
3.4 The galaxy model	81
4 Galaxy harassment	87
4.1 The Monte Carlo method	87
4.1.1 Perturber mass determination	88

4.1.2	Impact parameter distribution	90
4.1.3	The encounter rate	92
4.1.4	The perturbers velocity	93
4.2	Galaxy harassment simulation setup	94
4.2.1	Scaling of quantities	95
4.3	Simulating the Virgo tidal field	97
4.4	Stellar evolution models of the galaxy	98
4.4.1	The disk stellar population	100
4.4.2	The bulge stellar population	102
5	Results	107
5.0.3	The effect of the tidal field	107
5.0.4	The galaxy harassment effect	111
5.0.5	Image photometry	113
5.0.6	Structural parameters	115
6	Discussion	129
	Conclusions	134
	Bibliography	I

List of Figures

1	Luminosity functions for two samples of galaxies. The top panel is based on a sample of galaxies near the Milky Way. The bottom panel is based on a sample of galaxies located in the Virgo cluster. The figure is taken from Binggeli et al. (1988).	52
1.1	Block time steps exemplary for four particles. Source: Nbody6 ++ code manual.	61
2.1	Age distribution of Virgo galaxies (red=old)from GALEV-Gazelle. The X-ray contours come from Schindler et al. 1999. Source: J. Janz O. Hielsche.	66
2.2	Bright early type dwarf ellipticals scheme taken from Lisker et al. 2007: The ellipsoids found in the bottom of each subtype are based on the median of the estimated intrinsic axial ratios for each sub-type.	67
2.3	Scheme of the galaxy orbiting the Virgo cluster center.	69
2.4	Galaxy's eccentric orbit over time for an eccentric orbit with an eccentricity value of $e = 0.5$	71
3.1	Iteration process for the calculation of the halo and disk combined potential. . .	80
3.2	Iteration process for the calculation of the halo and disk combined potential. . .	81
3.3	Galaxy model rotation curve: The three components and the total contribution are shown in different colors. The galaxy's typical velocity at half-mass radius is 70km/s	82
3.4	Toomre stability parameter $Q = \sigma_r \kappa / 3.36 G \Sigma$	84
3.5	Cumulative mass for the components of the galaxy model: The three components and the total contribution are shown in different colors. The galaxy's total mass is $5 \times 10^{10} M_{\odot}$	85

3.6	Galaxy model volume density profile. The three components and the total contribution are shown in different colors. The blue line is a density profile $\propto r^{-2}$	85
4.1	Differential subhalo abundance functions per unit host mass for the final halos in the GA1,GA2 and GA3n simulations, error bars assume Poisson uncertainties in the counts. Source: Gao et al. (2004).	88
4.2	Cumulative radial distributions at $z = 0$ for subhalos within r_{200} for the GA3n halo and 15 clusters. The lines overlying the symbols are the corresponding fits. Source: Gao et al. (2004).	89
4.3	Gravitational focusing deflects the orbit of the perturber, r_{min} is the minimum distance between one another.	91
4.4	Perturber velocities drawn out of a Maxwellian distribution with a set of random numbers	94
4.5	Kroupa Initial Mass Function. Source Kroupa (2005).	99
4.6	Star formation rate of the galactic disk of the galaxy model	100
4.7	Galactic disk stellar mass	101
4.8	Galactic disk gas mass	101
4.9	Metallicity evolution of the galactic disk.	102
4.10	Star formation rate of bulge component of the galaxy model.	103
4.11	Stellar mass evolution of the bulge component. The SFR assigned follows an exponential decay with an e-folding time $\tau = 1 \times 10^7 yrs$.	103
4.12	Evolution of the gas mass of the bulge component over time. The SFR assigned follows an exponential decay with an e-folding time $\tau = 1 \times 10^7 yrs$.	104
4.13	Metallicity evolution of the bulge mass component. The initial metallicity assigned is Z_0 .	104
5.1	Schematic representation of the relevant time scales for the stellar evolution of the galaxy	108
5.2	Tidal energy as a function of galaxy's position relative to the cluster center in N-body units.	109
5.3	Coriolis energy as a function of galaxy's position relative to the cluster center in N-body units.	110

5.4	Projected particle positions of the three galaxy components. In red: halo; green: disk, blue: bulge	110
5.5	Disk thickening caused by tidal heating. Right figure: Disk at beginning of the simulations. Left figure: Disk after one orbital period of the galaxy within the galaxy cluster has been completed.	111
5.6	Time evolution of the galaxy embedded in the Virgo galaxy cluster field. The figure shows the projected particle positions for the three galaxy components in N-body units (1-Nbody length unit = 5 kpc). The left side figures show the same projection for the disk and bulge component.	118
5.7	Time evolution of the galaxy embedded in the Virgo galaxy cluster field. The figure shows the projected particle positions for the three galaxy components in N-body units (1-Nbody length unit = 5 kpc). The left side figures show the same projection for the disk and bulge component.	119
5.8	Time evolution of the galaxy embedded in the Virgo galaxy cluster field under the effect of the tidal field forces and encounters with other galaxies. The figure shows the projected particle positions for the three galaxy components in N-body units (1-Nbody length unit = 5kpc). The left side figures show the same projection for the disk and bulge component.	120
5.9	Time evolution of the galaxy embedded in the Virgo galaxy cluster field under the effect of the tidal field forces and encounters with other galaxies. The figure shows the projected particle positions for the three galaxy components in N-body units (1-Nbody length unit = 5kpc). The left side figures show the same projection for the disk and bulge component.	121
5.10	Galaxy remnant at the end of the simulation.	122
5.11	Effective surface brightness versus effective radius. The red dots represent the initial model and the subsequent stages after encounters have occurred. The arrow points towards the final stage (remnant galaxy). In blue: early-type galaxies. In green: late-type galaxies.	123

-
- 5.12 Effective surface brightness versus SDSS-r absolute magnitude M_r . The Virgo distance modulus is $M - m = 31.09$. The red dots represent the initial model and the subsequent stages after encounters have occurred. The arrow points towards the final stage (remnant galaxy). In blue: early-type galaxies. In green: late-type galaxies. 124
- 5.13 Effective radius versus SDSS-r absolute magnitude M_r . The Virgo distance modulus is $M - m = 31.09$. The red dots represent the initial model and the subsequent stages after encounters have occurred. The arrow points towards the final stage (remnant galaxy). In blue: early-type galaxies. In green: late-type galaxies. . . . 125
- 5.14 SDDS color - magnitude diagram: $g - i$ vs absolute magnitude M_r . The Virgo distance modulus is $M - m = 31.09$. The red dots represent the initial model and the subsequent stages after encounters have occurred. The arrow points towards the final stage (remnant galaxy). In blue: early-type galaxies. In green: late-type galaxies. 126
- 5.15 SDDS color -color diagram: $u - r$ vs $i - z$. The red dots represent the initial model and the subsequent stages after encounters have occurred. The arrow points towards the final stage (remnant galaxy). In blue: early-type galaxies. In green: late-type galaxies 127

List of Tables

3.1	Disk parameters of N-body galaxy model: disk mass, disk scale radius, disc truncation radius, disc scale length, disc truncation width.	83
3.2	Bulge parameters of N-body galaxy model: Bulge cut-off potential, bulge velocity dispersion, bulge central density.	83
3.3	Halo parameters of N-body galaxy model: Halo central potential, halo velocity dispersion, halo potential flattening, halo concentration $C = R_{c2}/R_k2$, characteristic halo radius.	84
3.4	Galaxy model properties: disk mass, disk central radial velocity dispersion, disk radial extent (in disk scale lengths), bulge mass, bulge radial extent (in disk scale lengths), halo mass, halo radial extent (in disk scale lengths).	84
5.1	Structural parameters derived from the galaxy photometry.	115
5.2	Galaxy colors derived from the galaxy photometry.	115

Introduction

Galaxy clusters and their formation are fundamental for understanding the cosmology of the Universe. Their galactic populations provide the key for understanding their evolution, showing different properties than the galaxies that are found in the field. Several interesting processes take place in this environment and drive a morphological and dynamical evolution of the objects sitting within the clusters. These environmental effects determine in a big part, the different morphologies of the galaxies that are found on them. Also, the fact of having old or young galaxy clusters that are still not virialized plays a role in the physics of the clusters.

Interestingly, the galactic populations of these objects are ruled by different relations, as discovered by Dressler (1980) work, it was proven that galaxies do not seem to sit randomly in the cluster. They follow the so-called morphology-density relation, that basically tells us that galaxies have different morphologies depending on where are they located in the galaxy cluster.

Late-type galaxies such as spirals and irregulars are located preferentially in the outskirts of the cluster. On the other hand, low-mass early-type galaxies seem to cluster in the center orbiting the core or orbiting around a more massive companion.

There are several interesting ways to try to disentangle the origin and formation of these objects. Many studies of the luminosity function (LF) have been made to locate galaxies depending on their morphology and luminosity. The LF gives the relative numbers of galaxies as a function of luminosity but also as a function of its morphological type. It gives the number of galaxies per unit volume for

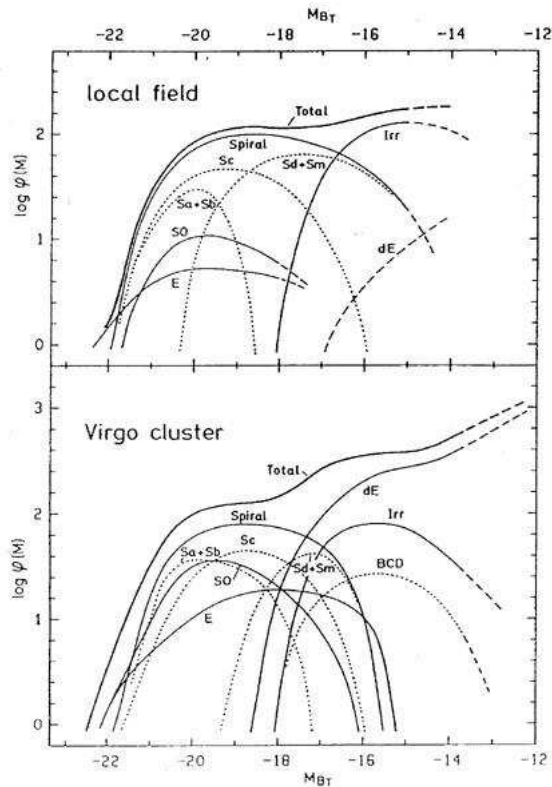


Figure 1: Luminosity functions for two samples of galaxies. The top panel is based on a sample of galaxies near the Milky Way. The bottom panel is based on a sample of galaxies located in the Virgo cluster. The figure is taken from Binggeli et al. (1988).

a morphological type. This function is parametrized by the Schechter function (Schechter and Peebles, 1976) :

$$\Phi(L) = \phi_* L^\alpha \exp\left[\frac{-L}{L^*}\right] dL \quad (1)$$

where α is the faint-end slope of the LF.

The faint-end of the LF is dominated by dE galaxies in clusters, while the late-type ones such as spirals and irregulars dominate in low-density environments. Still, to assess this definitely is hard, as errors in measurements can mislead by the fact of taking the co-moving volume V/V_{max} . This a volume measure that assumes that the number density of objects remains constant with time but galaxies are not really uniformly distributed in space (Binggeli et al, 1998).

These early-type galaxies are called early-type dwarf (dEs), because these galaxies

resemble the early-type galaxies (ellipticals). By definition, these objects have an absolute magnitude of $M_B > -18$ and they are mostly found in galaxy cluster environments.

Previously, it was thought that these galaxies were an extension of the bright elliptical galaxies but fainter. They are considered to be the progenitors of brighter systems according to the hierarchical formation scenario that as a consequence of our current standard cosmological model Λ CDM.

With the advance of galactic surveys such as the SDSS Virgo data set, it has been discovered that these galaxies are not as simple as it was thought and that indeed, they have a more complex morphology and kinematics than it was expected (Lisker et al. (2008, 2006)).

The cluster environment affects the galaxy morphology. Mechanisms such as ram pressure, tidal stripping and galaxy harassment can play a significant role on determining the fate of a galaxy's shape through its time evolution.

Ram pressure stripping is the pressure generated by a moving galaxy within the galaxy cluster. When it orbits through the intracluster medium (ICM), its gas experiences a ram pressure driven by the following relation:

$$P_{ram} = \rho v^2 \quad (2)$$

where ρ is the density of the intra cluster medium (ICM) and v is the galaxy's orbital velocity.

According to this equation (Gunn and Gott, 1972), ram pressure stripping is expected to become more significant in a high density environment like in the center of a galaxy cluster. This kind of mechanism is purely hydrodynamical and affects mainly diffuse gas.

Boselli (2008) based on the work made by Vollmer et al.2001 models ram-pressure stripping events and galaxy starvation (i.e. no more surrounding gas that can act as supply for star formation) concluding that star-forming systems such as disk galax-

ies that are infalling in the cluster are effectively stripped of their gas by subsequent ram-pressure events.

The tidal field of the cluster itself has strong dynamical influence on galaxies, in particular in their extended halos. First the dark matter halos are stripped, after few Gyrs, the gas available to provide the interstellar medium with material to form stars, leading to a gradual decline in star formation in cluster galaxies. This phenomenon was first invoked by Larson et al. (1980), and simulated by Bekki and Chiba (2001). The latter assumed an accretion rate of $1 M_{\odot}/yr$ for a normal field galaxy, and show that the tidal field of the cluster efficiently removes the gas reservoir from a galaxy, and consequently its fueling of star formation. This tidal truncation does not depend very strongly on the orbit of the galaxy in the cluster, and the consequent truncation of the SF is widespread through the cluster, contrary to what is expected from ICM interactions. Once the gas reservoir is removed, disk galaxies are slowly transformed into lenticulars (SO's) thickening and shortening their stellar disk.

Tidal stripping results from the interaction of a system with its environment or with another system. It occurs when a tidal force exceeds the gravitational forces exerted by the perturber which can be in this case either the cluster or a galaxy (perturbers) and the reference system. Its effect is given by the following equation:

$$\frac{2GM}{R^3}r > \frac{Gm}{r^2} \quad (3)$$

where M is the mass of the perturber, R is the distance of the perturber, m is the mass of the perturbed system and r is the distance from the center. Tidal interactions may also have short time scales in galaxy clusters, being dominant in the cluster outskirts. There is then, a correlation between morphology and distance to the cluster center. Within the cluster, galaxy-galaxy tidal forces and galaxy-cluster tidal forces are both present but the latter has its stronger interaction near the cluster center.

Galaxy harassment (Moore et al., 1998) is the effect of several fast encounters between two or even more galaxies combined with the tidal field. The effect of these interactions depends both in the velocity of the encounter and in the density of the environment. What basically happens here is an energy exchange between both galaxies giving place to an increase of its internal energy. The dark matter halo embedding the galaxy and the stars that form it absorb energy as $\Delta E \approx \frac{1}{2}\Delta V^2$. Where ΔV^2 is the change on relative velocity between the perturbed galaxy and the harassing one.

All this physical processes can change the morphology of galaxies in a galaxy cluster by stripping material and gas from them consequently resulting in a star formation quenching. It is still matter of debate which process leads to this change in morphology.

The galaxy harassment scenario has been recreated in numerical simulations by several authors (Moore et al., 1998), Mastropietro et al. (2004), A. Aguerri et al. (2010), R. Smith et al. (2010)) arriving to different conclusions. R. Smith (2010) concludes that galaxy harassment does not strip material from the galaxy in its first passage by the pericenter so effectively as Moore et al. (1998) or Mastropietro et al. (2005). On the other hand A. Aguerri et al (2010) focus their work on trying to investigate whether the different locations of the remaining dwarf galaxy of a harassed disk galaxy in the fundamental plane compared to the location of elliptical galaxies can be due to the morphological transformation of disks into low- mass systems. This works also finds galaxy harassment strongly efficient to strip material out of galaxies, losing after several encounters the 50% – 80% of its total mass and 30% – 60% of luminous matter.

As mentioned in the abstract of this work, our aim is to explore the galaxy harassment scenario via N-body direct numerical simulations in the context of multi-stellar populations by comparing the colors and other physical parameters such as surface brightness and effective radius of the remnant of our harassed galaxy with those of the dwarf ellipticals found in the Virgo galaxy cluster field using observations from

the Sloan Digital Sky Survey (SDSS).

In Chapter 1, the usage and performance of the N-body6 GPU numerical simulation code used in this work in order to model a three-component disk galaxy infalling into the Virgo galaxy cluster will be described.

Chapter 2 describes the Virgo cluster tidal field exerted by the cluster as well as the implementation of the elliptical orbit that the simulated galaxy follows across.

Chapter 3 describes the initial conditions of our simulation, i.e. the build-up of the galaxy model that is used to carry out the galaxy harassment simulations.

In Chapter 4 the Monte Carlo method that we used in order to model the galaxy perturbers that cause the harassment effect is described as well as the simulation setup within the N-body6 GPU code. The stellar population models that represent the stars that compose the bulge and the galactic disk of our harassed galaxy using the GALEV synthetic spectra models will be also described in this chapter.

Chapter 5 describes the results of our simulations for the tidal field, the galaxy harassment effect and the comparison of the left-over stellar population of the remnant after having suffered several encounters.

In Chapter 6, a discussion about the results is followed comparing the results obtained by other works and the one done in this present work.

Chapter 1

The N-body6 GPU code

The usage of GPU's (Graphic Processor Units) have become very popular since the last few years. they tend to accelerate a broad range of applications, ranging from purely scientific tasks such as computational physics and astrophysics, image processing, engineering simulations until video and game applications.

Part of this development is based in the city of Beijing, in the National Astronomical Observatories of China (NAOC), where since February of this year a new GPU cluster has been installed and is currently running with 85 nodes, each with two NVIDIA Tesla C1070 GPU cards.

The direct N-body code used in this work is the N-body6 GPU, which is the GPU version of the already existing Nbody6 (Aarseth, 1999). This code is designed so far to run in one single node system. For the upcoming year, it is expected to be suitable also for the code Nbody6++ (Spurzem, 1999), which is the parallelized version of Nbody6.

The following is a description of the main technical aspects and procedures that the direct code Nbody6 follows in order to perform the numerical simulations. This chapter is based on the Nbody6++ user manual (Spurzem, 1999).

1.0.1 The Hermite integration method

Each particle is completely specified by its mass m , position r_0 and velocity v_0 where the subscript 0 denotes its initial values at time t_0 . The equation of motion for each particle i is given by its momentary acceleration $a_{0,i}$. This acceleration is due to the interaction with all other particles. This acceleration and its time derivative $a'_{0,i}$ are given by:

$$a_{0,i} = - \sum_{i \neq j} G m_j \frac{r_{0,ij}}{r_{0,ij}^3}, \quad (1.1)$$

$$a'_{0,i} = - \sum_{i \neq j} \left[\frac{v}{r_{0,ij}^3} + \frac{3r_{0,ij}(v_{0,ij} \cdot r_{0,ij})}{r_{0,ij}^5} \right] \quad (1.2)$$

where G is the gravitational constant, $r_{0,ij} = r_{0,i} - r_{0,j}$ is the relative particle position and $v_{0,ij} = v_{0,i} - v_{0,j}$ is the relative spatial velocity between the particle i and the particle j . A new position and velocity is 'predicted' for the next time step t by performing a Taylor series expansion for the position $r_i(t)$ and the velocity $v_i(t)$ to the third order:

$$r_{p,i}(t) = r_0 + v_0(t - t_0) + a_{0,i} \frac{(t - t_0)^2}{2} + a'_{0,i} \frac{(t - t_0)^3}{6} \quad (1.3)$$

$$v_{p,i}(t) = v_0 + a_0(t - t_0) + a'_{0,i} \frac{(t - t_0)^2}{2}. \quad (1.4)$$

The computed values of r_p and v_p do not fulfill the requirements for an accurate high-order integration, as mentioned in the code manual, even if one choses very small time steps an error on predicting the particle positions and velocities may occur. Therefore, it is required to perform an Hermite interpolation that approximates the higher accelerating terms by a Taylor series:

$$a_i(t) = a_{0,i} + a'_{0,i}(t - t_0) + a_{0,i}^2 \frac{(t - t_0)^2}{2} + a_{0,i}^3 \frac{(t - t_0)^3}{6}, \quad (1.5)$$

$$a'_i(t) = a'_{0,i} + a_{0,i}^2(t - t_0) + a_{0,i}^3 \frac{(t - t_0)^2}{2}. \quad (1.6)$$

Here the values for $a_{0,i}$ and $a'_{0,i}$ are already known, but a further derivation of Eq.(1.2) for the two missing orders on the right hand side turns to be cumbersome.

Instead, one has to determine the additional acceleration terms from the predicted r_p and v_p . The acceleration and time derivatives according to Eqs (1.1) and (1.2) are newly calculated obtaining the acceleration terms $a_{p,i}$ and its derivative $a'_{p,i}$. Because these values ought to be generated by the high-order terms (which calculation is avoided in the code), they are put into the left-hand sides of Eqs (1.5) and (1.6). Solving then for $a_{0,i}^{(2)}$ in Eq (1.) and then substituting it into Eq(1.5) and simplifying the obtained expression yields to the third derivative:

$$a_{0,i}^3 = 12 \frac{a_{0,i} - a_{p,i}}{(t - t_0)^3} + 6 \frac{a'_{0,i} + a'_{p,i}}{(t - t_0)^2}. \quad (1.7)$$

Similarly, substituting in Eq(1.7) into Eq(1.5) gives the second derivative:

$$a_{0,i}^2 = -6 \frac{a_{0,i} - a_{p,i}}{(t - t_0)^2} - 2 \frac{2a'_{0,i} + a'_{p,i}}{(t - t_0)}. \quad (1.8)$$

Note that the desired higher-order accelerations are found just from the combination of the low-order terms for r_0 and r_p . Although one never derived a higher order than the first derivative, the higher orders are easily achieved through Eqs(1.1) and (1.2). This is called the Hermite scheme.

The accuracy of the integrator is virtually the same as in the case of an explicit high-order derivation (Makino and Hut, 1988). Finally, one extends the Taylor series for $r_i(t)$ and $v_i(t)$ the Eqs (1.3) and (1.4), by two more orders and finds the corrected position $r_{1,i}$ and velocity $v_{1,i}$ of the particle i at the next time t_1 as:

$$r_{1,i}(t) = r_{p,i}(t) + a_{0,i}^{(2)} \frac{(t - t_0)^4}{24} + a_{0,i}^{(3)} \frac{(t - t_0)^5}{120} \quad (1.9)$$

$$v_{1,i}(t) = v_{p,i}(t) + a_{0,i}^{(2)} \frac{(t - t_0)^3}{6} + a_{0,i}^{(3)} \frac{(t - t_0)^4}{24}. \quad (1.10)$$

the integration cycle for upcoming time steps may now be repeated from the beginning (Eqs (1.1) and (1.2)). The error in r and v within the two consecutive time steps $\Delta t = t_1 - t_0$ is proportional to Δt (Makino, 1991; Makino and Aarseth, 1992).

1.0.2 Hierarchical time steps

Stellar systems are characterized by a fair range of densities which gives rise to different time scales of orbital parameters. In the classical picture, the closest two bodies, which require the smallest time-step due to the strong gravitational attraction, would determine the time-step for the force calculation for the entire system. However, for bodies in regions where the force variation is relatively small, a permanent re-computing of the force terms is time consuming, so, in order to economize the calculations, these object shall be allowed to move a longer distance before a re-computation of the force becomes necessary. This is the idea of the method used in the parallel Nbody 6 ++ code for assigning different time steps $\Delta = t_1 - t - 0$, that are quantized powers of 2, between the force computations.

First, each particle is assigned its own individual Δt_i . The block time-steps are then synchronized by taking the next-lowest Δt_i that is a quantized power of 2 (Makino, 1991), building a set $2^{-i}, i = 0, \dots, i_{max}$ where i_{max} is the minimum integer that fulfills the relation for the smallest time step $\Delta t_{min} > 2^{i_{max}}$. This creates a block of several particles which are due to the movement at each time step, as illustrated in Fig 1.1. In this example, the particle i has the smallest time step at the beginning, so that its spatial coordinates are determined at each time step. The time step of particle k is twice as large as i 's, and its coordinates are just extrapolated at the time steps marked by odd numbers, while a full force calculation is due to multiples of the largest Δt_i of all particles, here determined by particle m . The width of the time step of each particle may be altered after the end of the integration cycle, as demonstrated for the particles k and l beyond the label '8'. The time steps have to stay commensurable with both, each other as well as the total time, such that a hierarchy is guaranteed. This is the so-called 'block time step scheme' (Aarseth, 1963).

As a first estimate, the rate of change of the acceleration seems to be a reasonable quantity for the choice of an appropriate time step : $\Delta t_i \propto |a_{1,i}| |a'_{1,i}|$, but it turns out that for special situations in a many-body systems, it provides some undesired

numerical errors, so that nowadays, the following formula is mainly used:

$$\Delta t_i = \sqrt{\eta \frac{|a_{1,i}| |a_{1,i}^{(2)}| + |a'_{1,i}|^2}{|a'_{1,i}| |a_{1,i}^{(3)}| + |a_{1,i}^{(3)}|}}, \quad (1.11)$$

where η is a dimensionless accuracy parameter which controls the error. In most applications it is taken to be $\eta \approx 0.02$ to 0.04 .

In the code, the time steps are adjusted to their appropriate values fairly quick. Although successive time steps normally change smoothly, it is convenient to constrain the growth by a stability factor of 1.2 in order to exclude rapid changes in peculiar cases and to guarantee maximum precision in the force calculation.

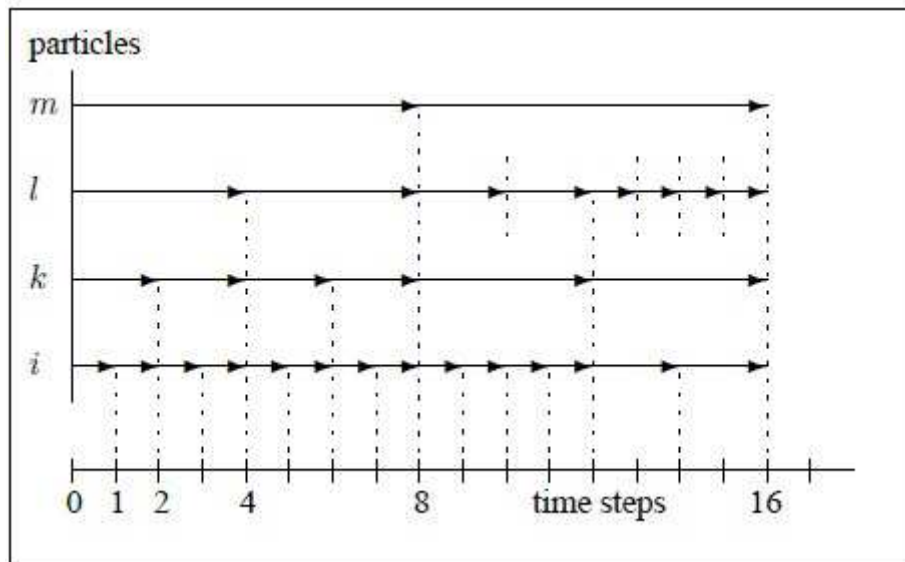


Figure 1.1: Block time steps exemplary for four particles. Source: Nbody6 ++ code manual.

1.0.3 The Ahmad - Cohen scheme

The computation of the full force for each particle in the system makes simulations very time consuming for large particle numbers, therefore, it is desirable to construct a method to speed up the calculations within the code while retaining the collisional

approach. One way to achieve this is to employ a 'particle neighbor scheme' (Ahmad and Cohen, 1973).

The idea behind this scheme is the splitting of the force polynomial Eq(1.5) for a given particle i in two parts, an irregular and a regular component:

$$a_i = a_{i,irr} + a_{ireg} \quad (1.12)$$

The irregular acceleration $a_{i,irr}$ results from particles in a certain neighborhood i . They give rise to a stronger fluctuating gravitational force, which is determined more frequently than the regular one of the more distant particles that do not change their relative distance to i so quickly. The full summation in Eq.(1.1) can be replaced by a sum over the N_{nb} nearest particles for $a_{i,irr}$ and a distant contribution from all the other. Whether a particle is a neighbor or not, is determined by its distance: all members inside a specified sphere (the neighbor sphere) with radius r_s are held in a list, which is modified at the end of each regular time step when the total force summation is performed. In addition, approaching particles within a surrounding shell satisfying $r_{0,ij}$.

In order to make the N-body6 GPU code suitable for the galaxy harassment simulations, it has been necessary to modify already existing subroutines and implement the code with new routines. Below I mention which changes and implementations have been made:

- Generalization of the Oort constants with Oort functions
- Modification of external force routines
- Eccentric orbit for infalling galaxy
- Monte Carlo routines for galaxy perturber generation
- Traditional scaling to different scaling system (in particular for this simulation)
- Implementation of new stellar evolution scheme (Ralf Kotulla and Daniel Bialas)

1.0.5 N-body units

By convention it has been agreed to have a standard N-body unit system where the gravitational constant G , the initial mass of the system M and the initial energy E_0 for bound systems are defined:

$$G = 1 \frac{[N_u]_l^3}{[N_u]_m [N_u]_t^2} \quad (1.13)$$

$$M = 1 [N_u]_m \quad (1.14)$$

$$E_0 = -\frac{1}{4} \frac{[N_u]_l^2 [N_u]_m}{[N_u]_t^2} \quad (1.15)$$

Inside the N-body6 GPU code physical units are scaled into N-body units in the following way:

All physical units are scaled using mainly three fundamental quantities: the length scaled called $RBAR$, the mass scale $ZMBAR$ and the gravitational constant which value in this unit system is $G = 1$. The time scale $TSTAR$ and the velocity scale $VSTAR$ are computed by using these fundamental scales:

$$N_{u_l} = RBAR \quad pc \quad (1.16)$$

$$N_{u_m} = ZMBAR \quad M_\odot \quad (1.17)$$

$$N_{u_t} = TSTAR \quad Myr \quad (1.18)$$

$$N_{u_v} = VSTAR \quad km/s \quad (1.19)$$

Where $TSTAR$ and $VSTAR$ are defined as:

$$TSTAR = \sqrt{RBAR^3 / G * ZMBAR} \quad (1.20)$$

$$VSTAR = 6.65 \times 10^{-2} \sqrt{G * ZMBAR / RBAR} \quad (1.21)$$

The scaling that has been performed in order to carry out our simulations will be explained later on in subsection 5.1.1. The complexity of the scaling requires a detailed explanation of how this is performed as in our case, we have three different scales: the galaxy's inner scale, the galaxy cluster scale and the stellar evolution scale.

Chapter 2

The Virgo cluster tidal field

The Virgo galaxy cluster (VC) has an irregular structure, as it is still a young galaxy cluster that is still undergoing relaxation, meaning that it is not yet completely virialized.

This galaxy cluster is located at the equatorial coordinates $\alpha = 12h30m$, $\delta = +12^\circ$, at a distance of 16.5Mpc. The active galaxy M87, is often referred to as the center of the galaxy cluster, as it is the center of the most massive subcluster of the VC.

There are about five clearly identified substructures in the VC. The two major components are a subclump called the 'M87 subclump' (Cluster A) and the 'M49 subclump' (Cluster B). The VC has about 1277 members and 574 possible members (VCC, Binggeli et al. (1985)) meaning that there is no clear distinction for these galaxies of whether they belong to the background or to the cluster.

Different morphological types are found in the VC, though dE galaxies are by far the dominant by number galaxy type. Galaxies in the VC show some trends when looking at their projected spatial distribution. Binggeli et al. (1988), found out how the different morphological types of the VC seem to distribute over the cluster by looking at the galaxy density as a function of location in the cluster and as a function of its type.

E and S0 galaxies are concentrated around the galaxy M87. These galaxies seem to be aligned with the jet of this galaxy (Arp, 1968), while the distribution of spiral and irregular galaxies (Sp and Irr) do not seem to follow any particular trend. They

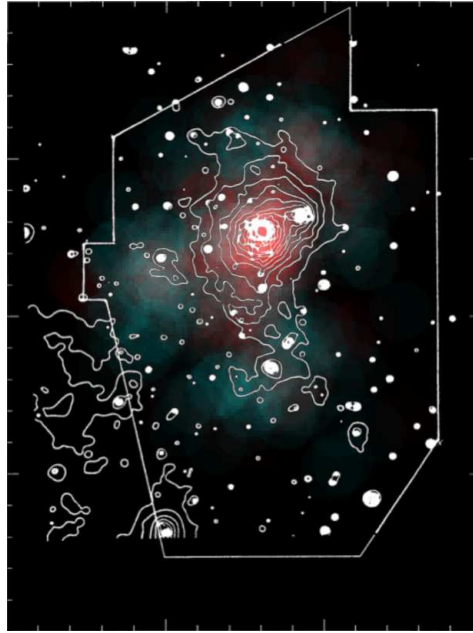


Figure 2.1: Age distribution of Virgo galaxies (red=old) from GALEV-Gazelle. The X-ray contours come from Schindler et al. 1999. Source: J. Janz O. Hielsche.

all seem to be scattered over the galaxy cluster.

On the other hand, the spatial distribution of dE's and dS0's is similar to that of the E and S0 galaxies concentrating towards Cluster A. They show a wide distribution in position and one can distinguish them between bright and faint, and between nucleated or non-nucleated. Lisker, 2007 showed a new classification scheme for the early-type dwarf ellipticals dE's by estimating intrinsic axial ratios for the subtypes shown in (Fig 2.2).

Galaxies not just display spatial trends due to their morphological type. The velocity dispersion of these objects is quite different too. E, S0's and dE's (early-type galaxies) have a narrower velocity distribution than Sp or Irr (late-type galaxies), which show a much broader spread in velocities, suggesting that these galaxies are not in the same evolutionary stage as the early-type ones. Some works have suggested that these galaxies are currently infalling in the galaxy cluster core (Tully and Shaya, 1984; Tully, 1986). dS0 galaxies are distributed in an array that coincides with the axis of symmetry that spans from the Cluster A to another smaller

subclump Cluster C.

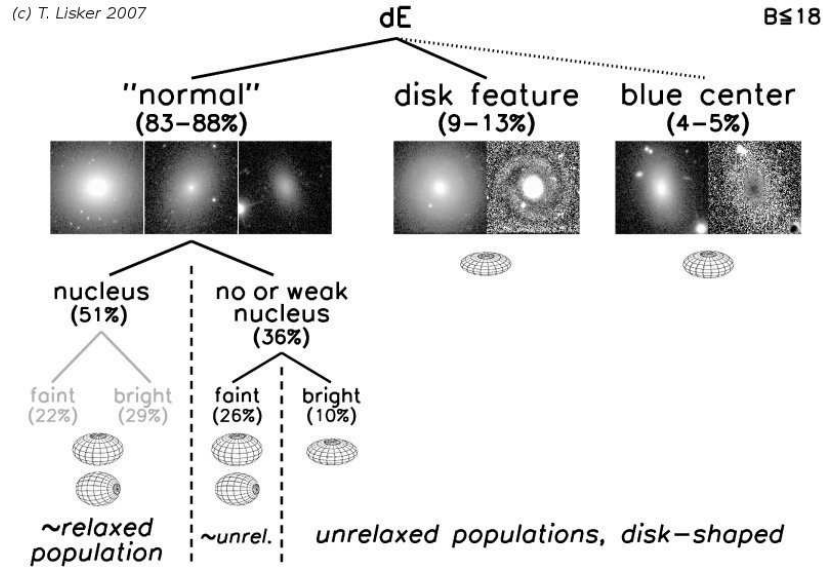


Figure 2.2: Bright early type dwarf ellipticals scheme taken from Lisker et al. 2007: The ellipsoids found in the bottom of each subtype are based on the median of the estimated intrinsic axial ratios for each sub-type.

Throughout this work, we will drive our attention to early-type dwarf galaxies in the context of their origin and formation. In particular, as mentioned in the overview of this work, we will explore the morphological transformation of a late-type galaxy into a dE via close encounters with massive galaxies that are already sitting in the galaxy cluster. This process makes the galaxy lose most of its gas and mass undergoing the morphological transformation from a 'disk-like' galaxy into a 'spheroidal shape-like' galaxy.

2.1 The field tidal forces

Galaxies in galaxy clusters suffer the effects of its gravitational interaction with the galaxy cluster potential. Different forces are generated while this interaction takes place. These forces are originated as galaxies rotate and orbit around the center of the galaxy cluster.

In order to see how infalling galaxies in VC are affected by the cluster's field potential, we model the Virgo tidal field by following a parametrization of the universal dark matter profile suggested by the work published by Navarro et al. (1996).

Cosmological simulations of structure formation in a $\Lambda - CDM$ Universe, suggest that dark matter halos form following a universal density profile given by the expression:

$$\rho_{dm} \propto \left(\frac{r}{r_s}\right)^{-1} \left(1 + \frac{r}{r_s}\right)^{-2} \quad (2.1)$$

where ρ_{dm} is the dark matter density and r_s is the scale radius. To construct the dark matter halo density profile of the Virgo cluster we take the values given in McLaughlin (1999). This work provides a parametrization of the dark matter density of the VC based in a model that describes the mass and dynamics of M87 and the VC. Surface photometry and mass estimates coming from X-ray observations of the hot intracluster gas are used for its computation as well as the velocity dispersions of early-type Virgo galaxies. The latter are used to constrain the dark matter halo density in the range $0 < r < 2$ Mpc. It is assumed that the VC is spherically symmetric and that is centered in M87. Late -type velocity dispersions of galaxies are excluded as they reflect some optical irregular structure that might bias the modeling of the dark matter halo density profile. On the other hand, early-type Virgo galaxies are used as they are spatially concentrated with a roughly Gaussian velocity distribution.

The parameters used to construct the VC dark matter halo based on this model are :

$$\rho_{dm} = K \left(\frac{r}{r_s}\right)^{-1} \left(1 + \frac{r}{r_s}\right)^{-2} \quad (2.2)$$

$$M_{dm} = 4\pi K r_s^3 \left[\ln\left(1 + \frac{r}{r_s}\right) - \left(\frac{r}{r_s}\right) / \left(1 + \frac{r}{r_s}\right) \right] \quad (2.3)$$

Where K is the estimated density parameter $K = (3.2_{-1.3}^{+2.6} \times 10^{-4}) M_{\odot} pc^{-3}$ and r_s is the scale factor $r_s = 560_{+200}^{-150}$. In this model, the virial radius of the dark matter halo - within which its mean density is 200 times the critical density for closure - is $r_{200} = 1.55 Mpc$ for $H_0 = 70 \frac{km}{s} * s^{-1} Mpc^{-1}$ corresponding to a virial mass of

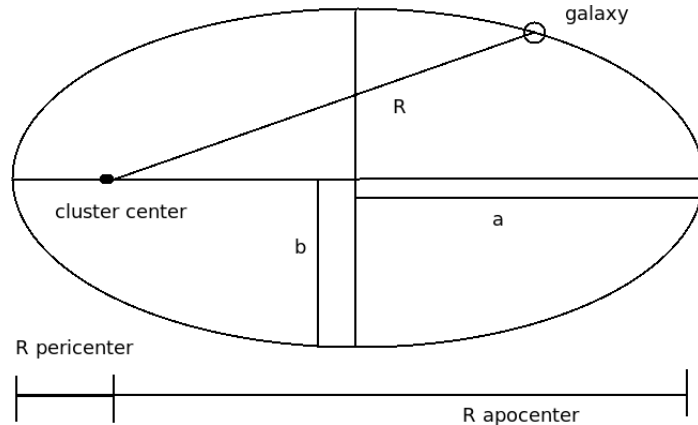


Figure 2.3: Scheme of the galaxy orbiting the Virgo cluster center.

$$M_{dm}(r_{200}) = (4.2 \pm 0.5) \times 10^{14} M_{\odot}.$$

2.2 Eccentric orbit

Galaxies move in eccentric orbits while infalling into a galaxy cluster. They usually fall into it by following an almost radial orbit. We assume that the galaxy is infalling in an eccentric orbit with e . Then, we use an orbit integration that approximates a two-body orbit with a keplerian orbit in the following way:

First, we take the polar equation that denotes a two-body orbit:

$$r = p/(1 + e \cos \theta(t)) \quad (2.4)$$

where p is the parameter of the ellipse.

For the determination of p in the polar formula, one uses the fact that angular momentum is conserved, using the expression $J^2/(GM)$. J is the constant angular momentum per unit mass and M is the gravitating mass of the central body, where we use the mass $M(R_0)$ determined at the galaxy's radius R_0 . By using this method, we approximate the galaxy's orbit by a keplerian instead of using the real orbit in the distributed mass potential. It is convenient for us to use this constant

mass approach since it is very difficult to estimate the error if one uses a petitions dependent mass that is variable with time $M(R(t))$.

To find the angle $\theta(t)$ subtended by the vector position of the galaxy and the major axis $2R_0$ we use again the angular momentum conservation, where the differential of angle $d\theta$ is expressed as:

$$d\theta = (J/r^2)dt \quad (2.5)$$

We make the galaxy begin at the orbit's apocenter, so we define the angular momentum in terms of it:

$$J = J_0 = r_{apo} * v_{apo} = r_{apo}^2 * \Omega_{apo} = const. \quad (2.6)$$

Where J is a constant which can be determined at the apocenter r_{apo} . The process of determining a new r from θ and then a new $d\theta$ from new r iteratively, is a kind of low-order simple two-body integration that allows us to work with a constant mass. Ω_{apo} is the galaxy cluster's angular velocity determined and interpolated at the apocenter position.

2.2.1 Tidal radius

Another important quantity that is calculated together with the eccentric orbit, is the tidal radius. This quantity tells us the radius of gravitational interaction between the potential and the galaxy:

The self-gravitating force is given by:

$$F \approx GM_{gal} \frac{\delta m}{r^2} \quad (2.7)$$

The tidal force is:

$$F_{tide} \approx GM_{cl} \frac{\delta m r}{R_{tide}^3} \quad (2.8)$$

These two forces become equal when,

$$F \approx F_{tide} \quad (2.9)$$

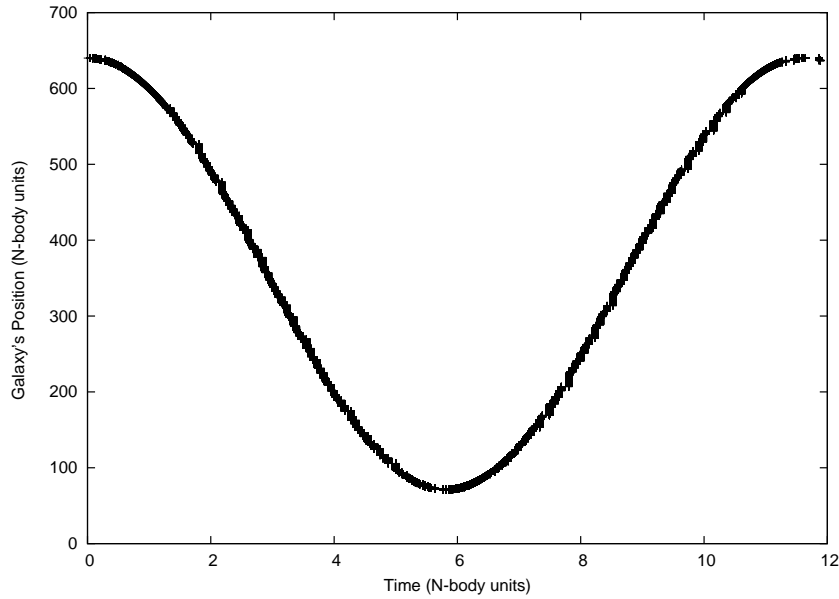


Figure 2.4: Galaxy's eccentric orbit over time for an eccentric orbit with an eccentricity value of $e = 0.5$

thus,

$$GM_{gal} \frac{\delta m}{r^2} \approx GM_{cl} \frac{\delta m r}{R_{tide}^3} \quad (2.10)$$

$$R_{tide} = R_{cl} (M_{cl}/M_{gal})^{1/3} \quad (2.11)$$

where R_{cl} is the distance from the cluster center to the galaxy. M_{cl} is the galaxy cluster virial mass and M_{gal} is the galaxy mass.

2.2.2 Oort Functions

The Oort functions are a measure of the local circular velocity of a system moving within a potential. In this particular case, it measures the circular velocity of the infalling galaxy embedded in the galaxy cluster potential. These equations are the general expression of the well known Oort constants which are often used when describing the dynamics of the Milky Way being the Oort constants in this case, calculated by measuring the proper motions of stars within the galaxy.

We will use then the general expression in order to see how the motion of the galaxy changes depending on its position and later on calculate the tidal forces based on

these functions. They are given by the following expressions:

$$A = \frac{1}{2} \left[\frac{V_{circ}}{R_0} - \frac{dV_{circ}}{dR} \right] \quad km/s/pc \quad (2.12)$$

$$B = \frac{1}{2} \left[\frac{V_{circ}}{R_0} + \frac{dV_{circ}}{dR} \right] \quad km/s/pc \quad (2.13)$$

We calculate the V_{circ} and its derivative V_{circ}' using the Virgo parametrization described at the beginning of this section.

$$V_{circ} = \sqrt{(GM_{dm}/r)} \quad (2.14)$$

$$V_{circ}' = (1/(2V_{circ}))[(4\pi G\rho_{dm}r) - (GM_{dm}/r^2)] \quad (2.15)$$

In the following section, the equations of motion are shown and they will be expressed in terms of the Oort functions described above. We decided to express them in this way as the N-body code was already suitable for working out the calculation of the tidal forces by using the Oort constants for the solar neighborhood, so we just generalized it by extending their computation in the radial extent of interest for this problem creating a radial grid of values that cover the range beginning in the galaxy cluster center to a distance further than the virial radius as we assume that our galaxy comes from outside the galaxy cluster and afterwards falls within.

2.3 Equations of motion of the galaxy within the clusters potential

The coordinate system of the galaxy-galaxy cluster is a rotating reference frame where the origin is placed in the center of the galaxy cluster $R_0 = (x'_0, y'_0, z'_0)$ and the galaxy moves around it in an eccentric orbit in the geometric plane XY . The x-axis points towards the radial direction, while the y-axis points towards the rotation direction and the z-axis is perpendicular to the orbital plane of the galaxy's motion.

As a first approximation, the equations of motion are expressed in terms of the

galaxy's potential $\phi_g(x, y, z)$, the galaxy cluster's potential $\Phi_c(x, z')$ and the forces originated by this two-body interaction in a rotating frame.

$$\ddot{x} = \frac{d\phi_g}{dx} - \frac{d\Phi_c^2}{dR}\Big|_{R_0}x + \omega^2x + 2\omega\dot{y} \quad (2.16)$$

$$\ddot{y} = -\frac{d\phi_g}{dy} - 2\omega\dot{x} \quad (2.17)$$

$$\ddot{z} = -\frac{d\phi_g}{dz} - \frac{d\Phi_c^2}{dz'}\Big|_{R_0}z' \quad (2.18)$$

Following Binney and Tremaine (1987), one can relate the derivatives of the potential with the epicyclic frequency κ and the vertical frequency ν . The equations of motion in the three directions are given then by:

$$\ddot{x} = f_x - (\kappa^2 - 4\omega^2)x + 2\omega\dot{y} \quad (2.19)$$

$$\ddot{y} = f_y - 2\omega\dot{x} \quad (2.20)$$

$$\ddot{z} = f_z - 2\nu^2z \quad (2.21)$$

Where $f_x, f_y, f_z = \nabla\phi_g$ and ω is the angular velocity.

The general equation of motion can be then expressed by:

$$\ddot{r} = f_g - \nabla\phi_g - 2\omega \times \nu - \omega \times (\omega \times r) \quad (2.22)$$

The term $\omega \times r$ is the Coriolis force originated by the galaxy's rotation. As it is convenient because of our simulation setup, we express these quantities in terms of the Oort functions in the following way (Binney and Tremaine, 1987):

$$\omega^2 = (A - B)^2 \quad (2.23)$$

$$\kappa^2 = -4B(A - B) \quad (2.24)$$

$$\kappa^2 - 4\omega^2 = -4A(A - B) \quad (2.25)$$

$$\nu^2 = 4\pi G\rho_g + 2(A^2 - B^2) \quad (2.26)$$

The term $4\pi G\rho_g$ in the last equation is zero in our case as it is the contribution of the galactic disk. This term that is not relevant for us as we do model the tidal field

as an external force in our simulations.

The forces that dominate the inner part of the galaxy cluster due to the gravitational potential are the centrifugal force that acts radially between the center of the cluster and the galaxy and the vertical tidal force that acts perpendicular to the Galactic plane.

The centrifugal force

Is the radial force exerted by the potential of the cluster over the galaxy, in terms of the Oort functions, its equation is given by:

$$\frac{df_R}{dR} = -(A - B)^2 + 4A(A - B) \quad (2.27)$$

The vertical tidal force

Is the force perpendicular to the galaxy's orbiting plane, in terms of the Oort's constants, they are given by:

$$\frac{df_z}{dz} \approx 4\pi G\rho_g + 2(A - B) \quad (2.28)$$

Iterating over z :

$$f_z \approx [4\pi G\rho_g + 2(A - B)]z \quad (2.29)$$

Inside the Nbody6 GPU code they are calculated first by applying the coordinate transformation to a rotating system. Afterwards, tidal forces are computed by the external force calculation routines in Nbody units

The Oort functions have dimensions of $1/t$:

$$[A] = [B] = 1/[N_u]_t \quad (2.30)$$

The tidal parameters within are given by the following expression:

$$TIDAL_1 = 4A(A + B) \quad (2.31)$$

$$TIDAL_2 = 0 \quad (2.32)$$

$$TIDAL_3 = -2(A + B)(A - B) \quad (2.33)$$

$$TIDAL_4 = 2(A - B) \quad (2.34)$$

$$(2.35)$$

We calculate them at each galaxy position relative to the cluster center by computing a grid of values at 1kpc and afterwards the tidal forces are calculated through these tidal parameters.

Chapter 3

Initial conditions: Galaxy Model

We decided to use the self-consistent galactic models of Kuijken and Dubinski (1995) to model the infalling galaxy.

The software is called GalactICS and is in principle designed to create 'Milky Way like' N-body particle models consisting on three components, the disk, the bulge and the halo. However, it is possible to use it for other 'galaxy types' if one modifies carefully some of the parameters that are used to compute the models. In our case we modify some of the free parameters that can be manipulated in the input of the code in order to generate an N-body galaxy model with the required characteristics of our galaxy. This code works with distribution functions for the three galaxy components and computes the mass of each component, the position of each star (particle) that compounds the galaxy and the velocities of each of them. This are then, the initial conditions of our N-body galaxy harassment simulation.

3.1 The halo distribution function

The halo is a flattened analogue of the King model, the so called lowered Evans profile (Kuijken and Dubinski, 1995). The lowering process imposes a maximum energy on the particles in the halo allowing to have a halo of finite size unlike the usual Evans profile (Evans, 1993), meaning that this distribution function truncates

at energy $E = 0$ the flattened logarithmic potential that characterizes the Evans profile. The halo distribution function is:

$$f_{halo}(E, Lz^2) = \begin{cases} [(AL_z^2 + B)\exp(-E_0/\sigma_0^2) + C][\exp(-E/\sigma_0^2) - 1] & \text{if } E < 0 \\ 0 & \text{if } E > 0 \end{cases} \quad (3.1)$$

The density of this distribution function is given by the following equation:

$$\begin{aligned} \rho_{halo}(R, \Psi) = & \frac{1}{2}\pi^3\sigma_0^3(AR^2\sigma_0^2 + 2B)\text{erf}(\sqrt{-2\Psi/\sigma_0^2})\exp(-2\Psi/\sigma_0^2) \\ & + (2\pi)^{3/2}\sigma_0^3(C - B - AR^2\sigma_0^2)\text{erf}(\sqrt{-\Psi/\sigma_0^2})\exp(-\Psi/\sigma_0^2) \\ & + \pi\sqrt{-2\Psi}[\sigma_0^2(3A\sigma_0^2R^2 + 2B - 4C) + \frac{4}{3}\Psi(2C - A\sigma_0^2R^2)] \end{aligned} \quad (3.2)$$

the concentration $q = R_{tidal}/R_{core}$ is determined by the dimensionless central potential ψ_0/σ_0^2 . The more negative the value the greater the concentration. The parameters R_a and v_0 , affect the scaling of the halo mass profile.

3.2 The bulge distribution function

The bulge distribution function follows a King profile. Its effect in the modeling is more predictable than in the previous case. For example, decreasing the central velocity dispersion will create a more centrally concentrated bulge and decreasing the ψ cut-off will truncate the bulge and decrease its total mass. The bulge distribution function is:

$$f_{bulge}(E) = \begin{cases} \rho_b(2\pi\sigma_b^2)^{-\frac{3}{2}}\exp[(\Psi_0 - \Psi_c)/\sigma_b^2] \exp[-(E - \Psi_c)/\sigma_b^2] - 1 & \text{if } E < \Psi \\ 0 & \text{if } E > \Psi \end{cases} \quad (3.3)$$

$$\begin{aligned} \rho_{bulge}(\Psi) = & \rho_b \left[e^{(\Psi_0 - \Psi)/\sigma_b^2} \text{erf}(\sqrt{(\Psi_c - \Psi)/\sigma_b^2}) \right. \\ & \left. - \pi^{-\frac{1}{2}} e^{(\Psi_0 - \Psi_c)/\sigma_b^2} \left(2\sqrt{(\Psi_c - \Psi)/\sigma_b^2} - \frac{4}{3} [(\Psi_c - \Psi)/\sigma_b^2]^{\frac{3}{2}} \right) \right] \end{aligned} \quad (3.4)$$

3.3 The disk distribution function

The disk is parameterized directly by its mass profile so its effect on the rotation curve is predictable over the time. The characteristic frequencies (ω , κ , etc.) in the equatorial plane are iteratively calculated as well as the correction functions for the disk distribution function. These functions are multiplicative corrections of the surface density and vertical velocity dispersion which appear in the Shu distribution function (Shu, 1969).

$$f_d(E_p, L_z, E_z) = \frac{\Omega(R_c)}{(2\pi^3)^{\frac{1}{2}}\kappa(R_c)} \frac{\rho_d(R_c)}{\sigma_R^2(R_c)\sigma_z(R_c)} \exp\left[-\frac{E_p - E_c(R_c)}{\sigma_R^2(R_c)} - \frac{E_z}{\sigma_z^2(R_c)}\right] \quad (3.5)$$

Where $E_p = E - E_z$ is the energy in planar motions, L_z is the specific angular momentum about the axis of symmetry R_c and E_c are the radius and energy of a circular orbit with angular momentum L_z , and Ω and κ are the circular and epicyclic frequencies at radius R_c . The density corresponding to this distribution function is obtained by integrating over the three velocity components. The V_r and V_z integrals are straight forward, leaving the V_ϕ integral:

$$\rho_d(R, z) = \int_0^\infty \left[dv_\phi \equiv dR_c \left(\frac{R_c \kappa(R_c)^2}{2R\Omega(R_c)} \right) \right] \frac{2\rho_d(R_c)\Omega(R_c)}{(2\pi)^{\frac{1}{2}}\sigma_R(R_c)\kappa(R_c)} \times \exp\left[-\frac{\Psi(R, 0) - \Psi(R_c, 0)}{\sigma_R^2(R_c)} - \left(\frac{R_c^2}{R^2} - 1\right) \frac{v_c^2(R_c)}{2\sigma_{R^2}(R_c)} - \frac{\Psi(R, z) - \Psi(R, 0)}{\sigma_z^2(R_c)}\right] \quad (3.6)$$

The combined potential of the disk and halo is constructed according to Poissons equation, using :

$$\nabla^2\Psi(R, z) = 4\pi G[\rho_h(R, \Psi) + \rho_d(R, \Psi, \Psi_z)] \quad (3.7)$$

In order to create the model, there are three main steps that are performed by this program:

First, the potential is calculated, afterwards, the disk distribution function is generated using this given potential. Each component with a self-consistent distribution of particle orbits is computed by running a succession of programs to end

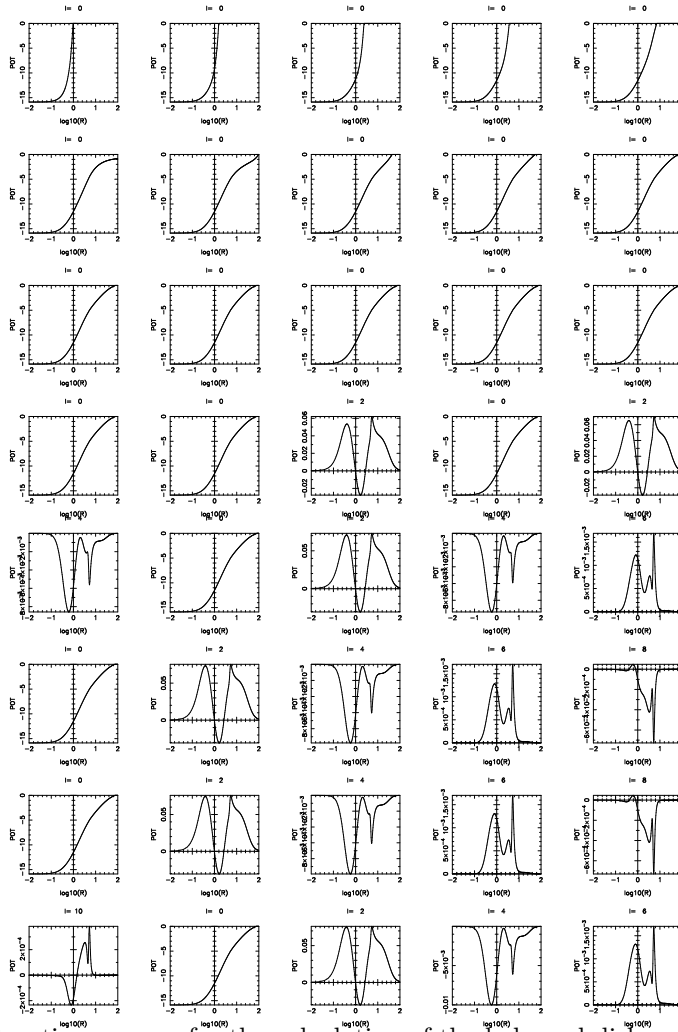


Figure 3.1: Iteration process for the calculation of the halo and disk combined potential.

up with a set of N-body particle masses, positions and velocities representing the modeled galaxy.

The potential is determined iteratively. It starts from an initial guess of the value of the potential, the density implied by the halo and bulge DF's is calculated, the disk density is added, and the potential of that mass distribution is used as starting point for the next iteration.

Initially only the monopole ($l = 0$) components are calculated until the model converges (Figs. 3.1), then one more harmonic is added per iteration up to the maximum requested, and once all harmonics are included the iterations are contin-

ued until the outer tidal radius of the halo is unchanged between iterations (Fig.3.2).

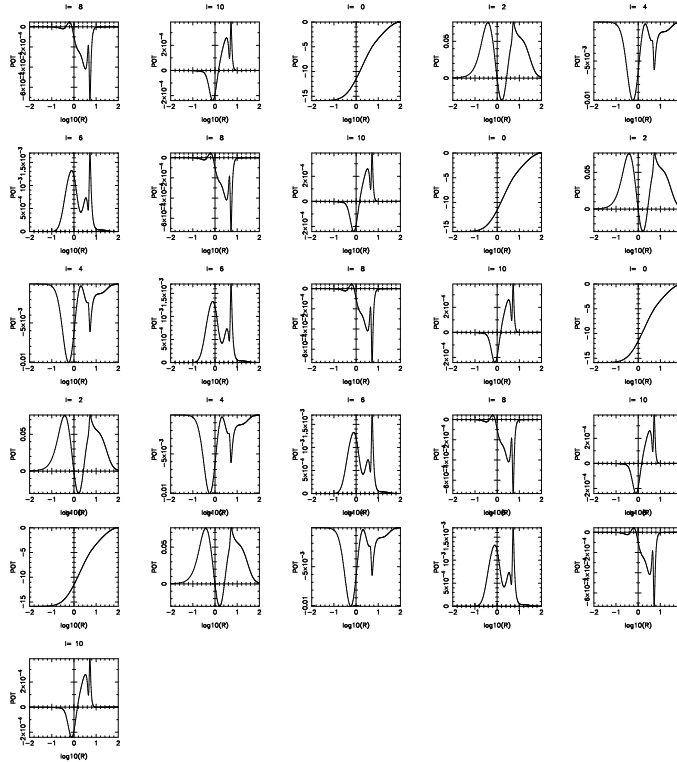


Figure 3.2: Iteration process for the calculation of the halo and disk combined potential.

3.4 The galaxy model

In previous publications, authors that have explored the galaxy harassment scenario through N-body simulations often use a disk galaxy that falls into the galaxy cluster (e. g. Mastropietro et al. (2005)). With the Kuijken and Dubinski (1995) models, it is possible to generate a bulge component with properties resembling to those of Sc-Sd galaxies, that even though they do not have a prominent bulge they neither lack of it.

Our galaxy has a total mass of $5 \times 10^{10} M_{\odot}$ (Fig3.5). It is formed by a disk, a bulge and a dark matter halo generated according to the distribution functions mentioned

in the previous section. The galactic disk has a stellar mass $M_d = 3 \times 10^9 M_\odot$. It has a disk scale-length of $R_d = 3kpc$ and a disk half-light radius of $5kpc$ extending about $5R_d$. The halo mass is about $16M_{disk}$ and has a radial extent of $25R_d$. The halo profile has a cut-off radius that makes the extension of the halo to be of finite length.

The rotation curve of the generated galaxy for the three galaxy components plus the total rotation curve is shown in Fig (3.3). The maximum contribution to the rotation curve of the galaxy from the disk is at around $2.5R_d$. The bulge component chosen for this galaxy model is less centrally concentrated compared to the Milky Way (see Fig3.6) making the bulge circular velocity component to be less pronounced reaching its peak velocity at larger radius.

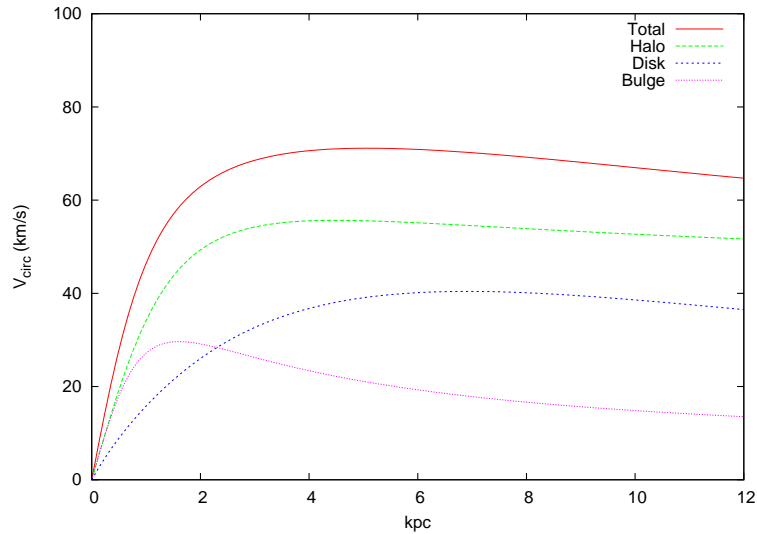


Figure 3.3: Galaxy model rotation curve: The three components and the total contribution are shown in different colors. The galaxy’s typical velocity at half-mass radius is $70km/s$.

We first created a sample model in order to check the program’s consistency before the parameters were modified to generate the desired galaxy model. The parameters used for the sample model (MW like model) and the three-component galaxy model (Sc model) are given in the following tables:

Disks can be affected by gravitational instabilities as these can cause overdense

Model	M_d	R_d	R_t	z_d	out
MW	1.00	1.0	5.0	0.15	0.3
Sc	1.00	1.0	5.0	0.15	0.3

Table 3.1: Disk parameters of N-body galaxy model: disk mass, disk scale radius, disc truncation radius, disc scale length, disc truncation width.

Model	Ψ_c	σ_b	ρ_b
MW	-2.0	0.50	10.0
Sc	-2.0	0.50	1.0

Table 3.2: Bulge parameters of N-body galaxy model: Bulge cut-off potential, bulge velocity dispersion, bulge central density.

regions within the disk to collapse. When modeling disks, it is important to know how stable is the disk that is being generated in the model. The Toomre Q parameter gives the conditions for a system instability. This is given by the following equation:

$$Q = \frac{\sigma_r \kappa}{3.36 G \Sigma} \quad (3.8)$$

Where σ is the stellar velocity dispersion, κ is the epicyclic frequency and Σ is the surface disk density. When $Q < 1$, the disk is unstable. The galactic disk of our galaxy model has a $Q = 1.7$ at the disk half-mass radius (Fig (3.4)).

Model	Ψ_0	σ_0	q	C	R_a
MW	-4.0000	1.00	0.9	0.1	0.5
Sc	-4.4788	1.00	0.9	0.1	0.5

Table 3.3: Halo parameters of N-body galaxy model: Halo central potential, halo velocity dispersion, halo potential flattening, halo concentration $C = R_{c2}/R_{k2}$, characteristic halo radius.

Model	M_d	$\sigma_{R,0}$	R_{e_d}/R_d	M_b	R_{e_b}/R_d	M_h	R_{e_h}/R_d
MW		0.94	0.50	5.6	0.29	1.7	9.6
Sc		0.94	0.50	5.6	0.16	1.7	16.6

Table 3.4: Galaxy model properties: disk mass, disk central radial velocity dispersion, disk radial extent (in disk scale lengths), bulge mass, bulge radial extent (in disk scale lengths), halo mass, halo radial extent (in disk scale lengths).

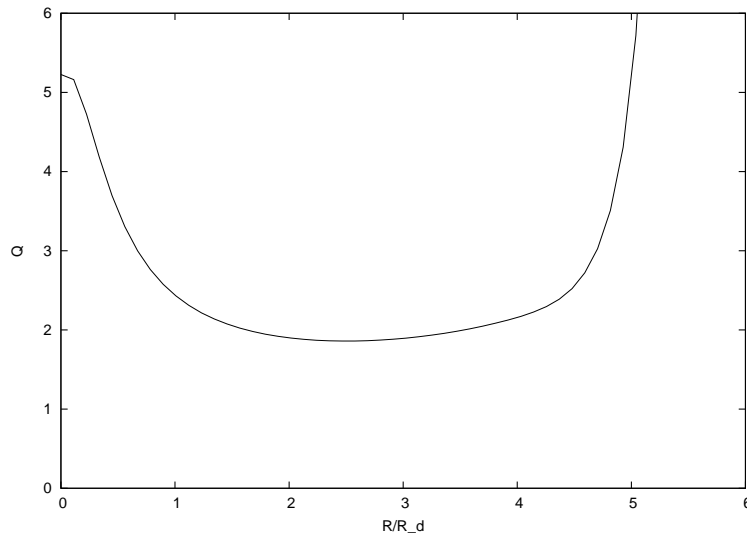


Figure 3.4: Toomre stability parameter $Q = \sigma_r \kappa / 3.36 G \Sigma$

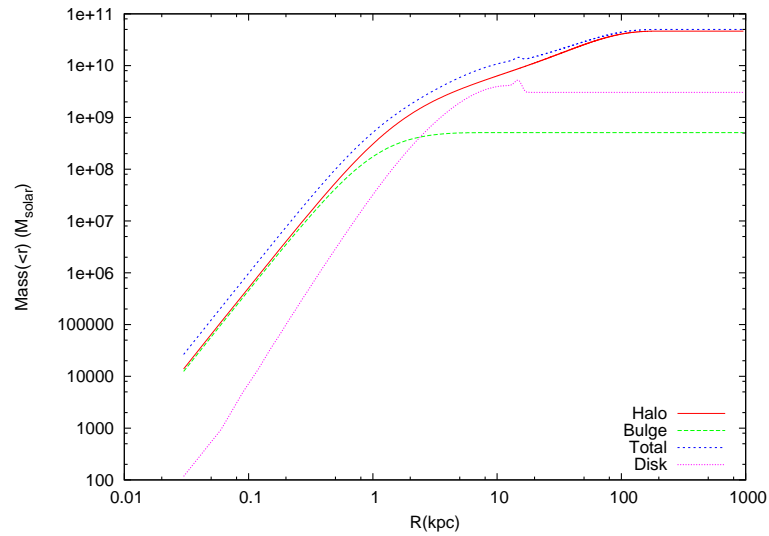


Figure 3.5: Cumulative mass for the components of the galaxy model: The three components and the total contribution are shown in different colors. The galaxy's total mass is $5 \times 10^{10} M_{\odot}$.

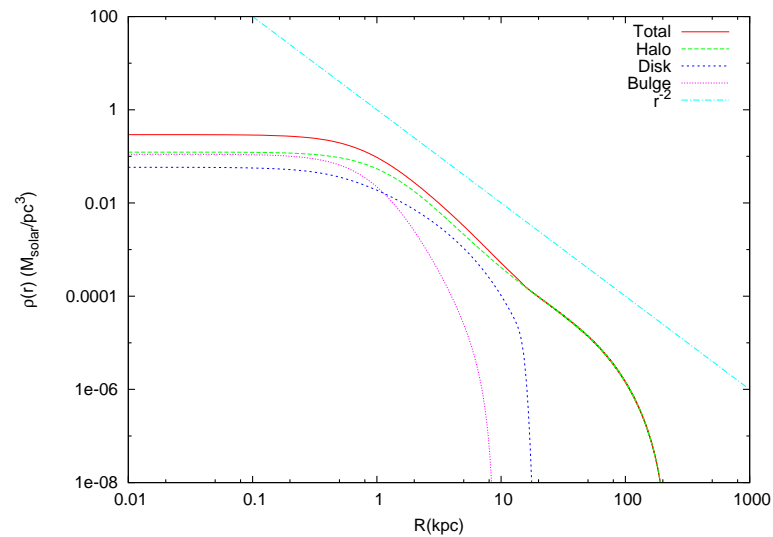


Figure 3.6: Galaxy model volume density profile. The three components and the total contribution are shown in different colors. The blue line is a density profile $\propto r^{-2}$

Chapter 4

Galaxy harassment

Galaxies that are infalling in galaxy clusters suffer several encounters with other galaxies in their way through the center of the galaxy cluster.

In these simulations, the galaxies that disturb the infalling galaxy are not modeled themselves, i. e. they are not originated as a set of N-body model as the modeled infalling galaxy does. The so-called Monte Carlo method was used in order to derive the basic parameters that are required to model the galaxy's perturbers. These parameters are the mass of the perturber, its velocity and its position.

4.1 The Monte Carlo method

We used the Monte Carlo method in order to obtain random numbers that describe the distribution functions of each of the perturber parameters.

In the case of the perturbers mass we take a subhalo distribution function prescribed by Gao et al. (2004). This distribution has a radial and a mass dependence and both are given separately. As they are linearly independent, we combine them in order to get a general expression that is both radial and mass dependent. The cumulative distribution function (CDF) of this expression is computed by generating a set of random numbers in order to draw the CDF to assure that indeed the perturber masses follow the desired distribution.

For the perturber velocities, we assume that they follow a Maxwell-Boltzmann distribution. It is computed by inverting the gamma function in order to get the CDF and sampling over it with a set of random numbers.

4.1.1 Perturber mass determination

Subhalos of dark matter are identified in cosmological simulations by using different methods, however the behavior of the subhalo populations seems to follow the same trend. This subhalo populations can be characterized by the differential subhalo mass function (MDF). Using the one prescribed in Gao et al. (2004) we have:

$$dn/dm \propto m^{-\alpha} \quad (4.1)$$

with $\alpha = 1.9$.

This MDF gives the mass dependence of the subhalo distribution over all possible

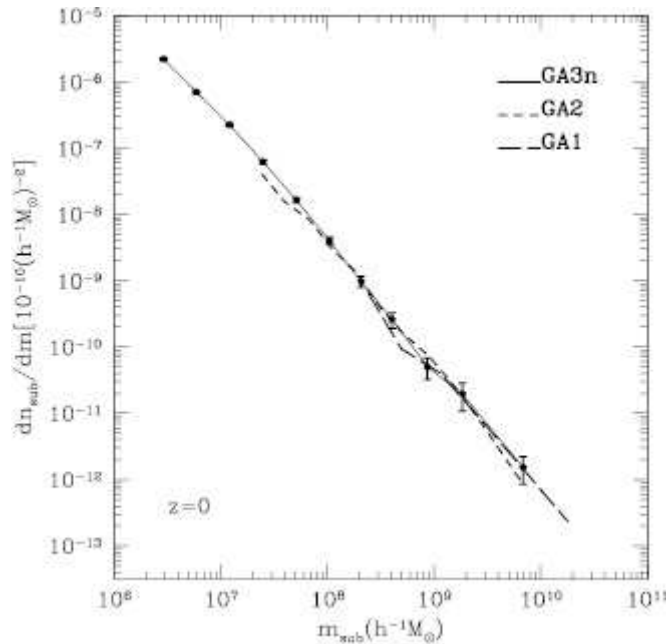


Figure 4.1: Differential subhalo abundance functions per unit host mass for the final halos in the GA1,GA2 and GA3n simulations, error bars assume Poisson uncertainties in the counts. Source: Gao et al. (2004).

mass ranges for the subhalos that embed the galaxy that will perturb the simulated galaxy.

The subhalo populations show also a radial dependence as it is shown in Fig(4.2) . The subhalo fraction relative to the total number of subhalos within the virial radius r_{200} is given by:

$$dN/dr \propto r^\beta \quad (4.2)$$

with $\beta = 1.1$.

Integrating, we obtain the cumulative mass $m \leq M$ inside R:

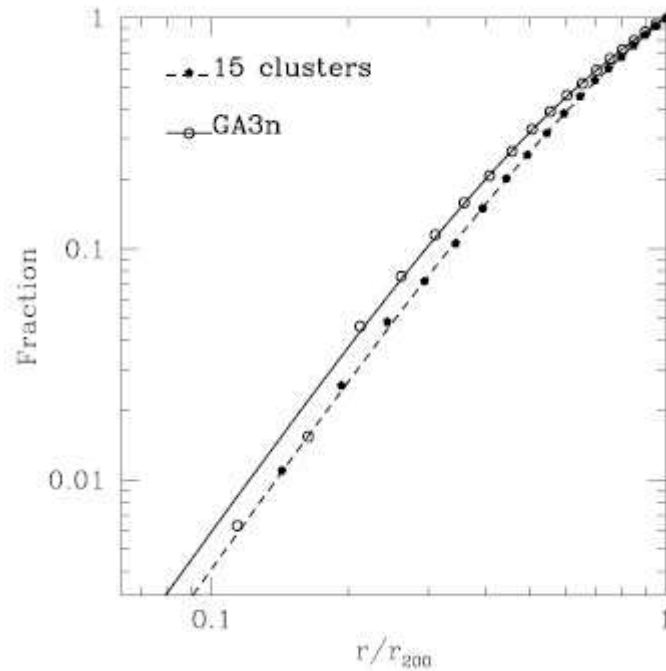


Figure 4.2: Cumulative radial distributions at $z = 0$ for subhalos within r_{200} for the GA3n halo and 15 clusters. The lines overlying the symbols are the corresponding fits. Source: Gao et al. (2004).

$$N(m \leq M) = C_1 \frac{1}{-\alpha + 1} m^{-\alpha+1} \quad (4.3)$$

$$N(r \leq R) = C_2 \frac{1}{\beta + 1} m^{\beta+1} \quad (4.4)$$

Afterwards, we combine the above equations (i.e. we multiply them since they are independent) and obtain the mass-radial dependent subhalo number density:

$$N(m \leq M, r \leq R) = C_1 * C_2 \frac{1}{(-\alpha + 1)(\beta + 1)} r^{\beta+1} M^{-\alpha+1} \quad (4.5)$$

The constants C_1 and C_2 are obtained for Eqs(4.1) and(4.2) assuming the following limits:

- $R_{min} = 0$ to $R_{max} = R_{vir} = 1.55 Mpc$
- $M_{min} = 5 \times 10^9 M_\odot$ to $M_{max} = \infty$

The total number of subhalos is estimated via observations ($N_{tot} = 321$) by using the Lisker, 2007 VCC catalogue, in the following way:

We take the VC luminosity distance $D_L = 16.5$ Mpc. The minimum perturber mass that we consider is $M_{pert} = 5.0 \times 10^9 M_\odot$. We take the mass-to-light in the B-band $M/L \approx 1$, so that we have $L = 5.0 \times 10^9 L_\odot$. The absolute magnitude of the sun in this band is $M_{abs} = 5.48$. We calculate the apparent magnitude from $m - M = 5 \log(D_L) - 5 = 31.09$. Then the dark mass to light ratio is $M_{dark}/M_{light} \approx 16.6$ we estimate the magnitude taking this ratio in account and we look at the VCC catalogue finding that the total number of subhalos is $N_{tot} = 321$ galaxies. Number that is consistent with Smith et al. (2010) and Gao et al. (2004). In order to draw the mass distribution, a set of random numbers is generated following Eq (4.5), as r the galaxy's position is known, it is fixed in the equation. The equation then is inverted and the masses are derived.

4.1.2 Impact parameter distribution

The impact parameter describes the galaxy's perturber hitting plane. The p vector describes the point of passage in the galaxy's rest-frame between the perturber and the galaxy if the perturber is not deflected (focused) and continued its motion. It moves in the same direction as the initial perturber velocity vector v_{inf} .

This hitting point is the intersection of the vector v_{inf} and the plane that is perpendicular to v_{inf} and goes through the origin of the galaxy's rest-frame, i.e. the hitting



Figure 4.3: Gravitational focusing deflects the orbit of the perturber, r_{min} is the minimum distance between one another.

plane.

It is needed then to construct :

- The initial velocity vector v_{inf}
- The perturber initial position vector r_{inf}
- The rest frame of the galaxy (hitting plane) P

It is required to satisfy the condition $v_{inf} \perp P$ i.e., v_{inf} is the normal vector with modulus V_{rel} . Its detailed calculation will be described in the following section. For the calculation of the p vector, it is required to first find the maximum impact parameter p_{max} . To determine the maximum impact parameter p_{max} we use the following equation (Spurzem et al., 2009):

$$p_{max} = \sqrt{\left(1 + \frac{M_{tot}}{V_{rel}}\right)} \quad (4.6)$$

Where $M_{tot} = M_{pert} + M_{gal}$ and V_{rel} is the relative velocity between the galaxy and the perturber.

The direction will be given by the angles α , β and γ , this is the transformation between the galaxy cluster rest-frame and the galaxy's rest-frame is given by the following transformation matrices:

$$\begin{aligned}
M_{rot_x} &= \begin{bmatrix} 1 & 0 & 0 \\ 0 & \cos(\beta) & -\sin(\beta) \\ 0 & \sin(\beta) & \cos(\beta) \end{bmatrix} \\
M_{rot_y} &= \begin{bmatrix} \cos(\alpha) & 0 & \sin(\alpha) \\ 0 & 1 & 0 \\ -\sin(\alpha) & 0 & \cos(\alpha) \end{bmatrix} \\
M_{rot_z} &= \begin{bmatrix} \cos(\gamma) & -\sin(\gamma) & 0 \\ \sin(\gamma) & \cos(\gamma) & 0 \\ 0 & 0 & 1 \end{bmatrix}
\end{aligned}$$

4.1.3 The encounter rate

The encounter rate gives us the number of encounters expected in a certain time interval. We calculate the frequency of encounters by taking the inverse of this quantity and weight it by the probability of encounters expected $P_{encounter} = 0.1/1Gyr$:

$$\frac{dN}{dt} = n(m, r)V_{rel}\Sigma \quad (4.7)$$

where $n(m, r) \propto r^{\beta-2}$. We define the cross section Σ as:

$$\Sigma = \pi p_{max}^2 \quad (4.8)$$

Gravity can affect the perturber's motion before the impact, such effect is called gravitational focusing. This is expressed by the term $1 + [\frac{v_{esc}}{v}]^2$ that is also known as the Safronov number, it is a measure of how gravity increases the collision cross-section as seen in the following equation:

$$\Sigma = \pi p_{max}^2 \times \left[1 + \left[\frac{v_{esc}}{v} \right]^2 \right] \quad (4.9)$$

here v_{esc} is the perturbers escape velocity.

Fast interactions between galaxies occur in galaxy clusters. The encounter velocity is higher than the rotational velocities of galaxies. As mentioned in the introduction of this work, the energy injected to the system scales as v^{-2} (Binney and Tremaine, 1987). This means that the effect of a fast encounter is minor when the encounter occurs at high velocities.

4.1.4 The perturbers velocity

To determine the relative velocity distribution it is assumed that the velocities of galaxies follow a Maxwellian distribution, it is known from observations that galaxies in general follow this kind of distribution. One can express the typical Maxwellian distribution expression as a distribution function of the 'line of sight' relative velocities between galaxy and perturber:

$$f(V_{rel}) = exp^{-V_{rel}/4\sigma^2} \quad (4.10)$$

The quantity V_{rel} represents the relative velocity between two galaxies. It is computed by using an average velocity dispersion value for the VC of $\sigma_{cluster} \approx 1204$ km/s (Fig 10, Conselice et al. (2001)). This velocity is calculated by using the average velocity of spiral galaxies in the cluster $\sigma_{sp} 900km/s$ and for the ellipticals $\sigma_e 700km/s$ gives an average σ for the central galaxy population of $\sigma 800km/s$. For the infalling galaxy we take a $\sigma = 900km/s$. Finally, the combined relative velocity dispersion is $\sigma_{cluster} = 1204km/s$.

The direction of the velocity vector and its position can be constructed by applying the same transformation that was performed for the impact parameter vector $p = (p, 0, 0)$ to the velocity vector $v_{inf} = (0, V_{rel}, 0)$ since this vector is perpendicular to the plane before the transformation is applied and the angles are invariant under transformations. The initial position of the perturber is then obtained by defining a distance at "infinity" R_{inf} and then solving the following set of equations for the

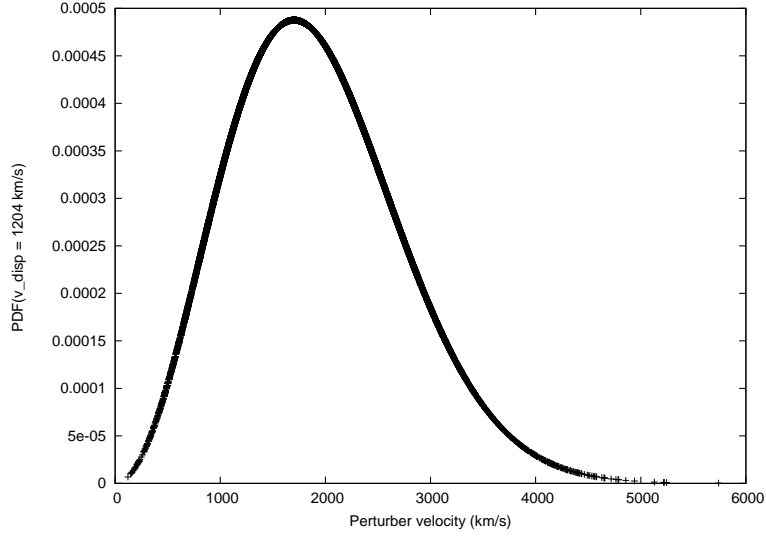


Figure 4.4: Perturber velocities drawn out of a Maxwellian distribution with a set of random numbers

transformed quantities:

$$r_{inf}' = p' + C * v_{inf}' \quad (4.11)$$

$$C * v_{inf} == R_{inf} \quad (4.12)$$

$$C = R_{inf}/v_{inf}' \quad (4.13)$$

$$C = R_{inf}/V_{rel} \quad (4.14)$$

$$r_{inf}' = p' + \frac{R_{inf}}{V_{rel}} * v_{inf} \quad (4.15)$$

After this transformation, the required quantities are in the galaxy rest-frame, r_{inf}' and v_{inf}' .

4.2 Galaxy harassment simulation setup

For the simulation setup, it is necessary to transform and scale all the calculated quantities into N-body units. We define the units for the galaxy-galaxy cluster system as:

$$1N_{u_l} = 5kpc \quad (4.16)$$

$$1N_{u_m} = 5 \times 10^{10} M_{\odot} \quad (4.17)$$

$$(4.18)$$

where $1N_{u_l}$ is the galaxy disk half light radius and $1N_{u_m}$ is the total mass of the galaxy.

The galaxy cluster mass and length parameters are given by the values found by McLaughlin (1999):

$$M_{vir} = 4.3 \times 10^{14} M_{\odot} \quad (4.19)$$

$$R_{vir} = 1.55Mpc \quad (4.20)$$

Which in Nbody units are expressed based on the pre-defined Nbody units defined by the galaxy parameters being therefore:

$$ZMBAR = 8400 \quad (4.21)$$

$$RBAR = 310 \quad (4.22)$$

$$(4.23)$$

Not forgetting that in an N-body unit system the gravitational constant has the value $G = 1$.

4.2.1 Scaling of quantities

The scaling of the quantities is performed in the following way:

In this particular galaxy simulation, we have three different scales: the 'galaxy cluster + galaxy system scale', the internal galaxy scaling and the stellar evolution scale. This is necessary because the Nbody6 GPU code is originally designed for simulating dense stellar systems, such as star clusters. Galactic systems in galaxy

clusters require additional scaling when using this code. Moreover, if stellar evolution is required, one has the additional stellar evolution scale.

The reasons for having so many different scales are the following: First, the mass of the galaxy cannot be represented particle by particle within the Nbody6 GPU code. A galaxy has typical masses ranging in $10^8 - 10^{13}M_{\odot}$, in particular, we aim to model a galaxy which mass is of the order of $10^{10}M_{\odot}$. As this is not physically possible, it is necessary to distribute the galaxy's mass over a number of particles much lower than the one we would require ideally.

Another issue, is the length of the system. This is longer than in the case of a star cluster. The scale length of star clusters is in the order of parsecs while the scale length of the galaxy is in the order of kiloparsecs and the cluster scale is in the order of megaparsecs.

The code converts physical quantities into N-body units by using the length scale and the mass scale which definition is given in section 1.1.5.

One has to be very careful when using the different scaling systems. In general words, what has to be done is to find a right conversion factor between the galaxy cluster scale and the galaxy's internal scaling guided by the output values provided by the code with its default values of $RBAR$ and $ZMBAR$ at first. Then one has to find the proper conversion factor between both systems. It is necessary to leave the mass scale factor $ZMBAR$ unchanged as it would lead to errors if one has the stellar evolution running. So one has to manipulate the value of the scale length $RBAR$ in order to achieve the desired scaling.

In our case, it has been necessary to scale the time and to scale the perturber velocities generated by the Monte Carlo implementation for generation of galaxy perturbers. This scaling is performed in the following way:

With the Nbody unit definition for length and mass and by using the definition of

the time scale factor $TSTAR$ (Eq (1.20)) one that the conversion factor in physical units between the galaxy cluster and the galaxy system is $T_C = 60MyrT_G$, one arrives to the relation:

$$RBAR_C = RBAR_G * 60^{(-2/3)} \quad (4.24)$$

which gives the right conversion factor between the galaxy cluster frame and the galaxy frame. Here, $RBAR_G$ is the internal galaxy length scale $RBAR$ that has been mentioned throughout the his text until now, and $RBAR_C$ that is the galaxy cluster length scale.

4.3 Simulating the Virgo tidal field

The calculation of the tidal forces within the code is carried out by dividing them into regular and irregular. Regular forces are those that do not present significant changes in its behavior during a certain time scale whereas the irregular forces do change and therefore, they have to be computed more often than the regular forces. The code divides them in these two groups as it is less expensive in terms of computing time, so, they are computed when it is required instead of doing it for each time step interval:

$$FIRR_y = TIDAL_4 * \dot{y} \quad (4.25)$$

$$FIRR_x = TIDAL_4 * \dot{x} \quad (4.26)$$

$$FREG_x = TIDAL_1 * x \quad (4.27)$$

$$FREG_z = TIDAL_3 * z \quad (4.28)$$

$$FREG_x = TIDAL_1 * \dot{x} \quad (4.29)$$

$$FREG_z = TIDAL_3 * \dot{z} \quad (4.30)$$

Tidal forces use the same conversion factor as the Oort functions, just keeping in mind that the tidal terms due to centrifugal forces have dimensions of $1/[t]^2$ while

the Coriolis term *TIDALA* has also dimensions of $1/[t]$.

Tidal forces dominate the vicinity of the galaxy cluster center, meaning that when galaxies pass near the pericenter of the orbit tend to get more tidally disrupted as the tidal field is stronger. In the other hand, the Coriolis force is dominating close to the edge of the galaxy cluster, where the tidal force effect is not strong anymore. The tidal radius of the galaxy is calculated using the formula given in the previous section at every orbital time step integration in order to avoid any miscalculation of the particles that are removed from the galaxy due to the interaction with either the tidal field or because of the galaxy harassment that will be discussed later on in this work.

4.4 Stellar evolution models of the galaxy

We assign two stellar populations to the disk and bulge components of the simulated galaxy by using the GALEV evolutionary synthesis models (Kotulla et al., 2009). To create a stellar evolution model, one needs to provide the star formation history (SFH) of the object that will be modeled, i.e . the initial mass function (IMF), the star formation rate (SFR) and the initial metallicity Z_0 . It is possible also to set the parameters of the cosmological model, which we choose to take the standard Λ -CDM values $H_0 = 70km/sMpc^1$ $\Omega_m = 0.3$ and $\Omega_\lambda = 0.7$.

GALEV follows the time and redshift evolution of its spectrum, luminosities and colors using the stellar BaSeL library of model atmospheres from Lejeune et al. (1998) which covers the wavelength range from UV to NIR. For the purpose of this work, we use the SDSS filter set whose filters cover the optical range and one near infrared band. At the end, one obtains information about the model evolution in terms of the gas content, stellar mass, gaseous, stellar abundances and SN rate.

The initial mass function (IMF) gives the number of stars newly born in a certain mass interval $[M, M + dM]$:

$$dN/dM \propto cM^{-(1+\alpha)} \tag{4.31}$$

α is a dimensionless exponent that shapes the distribution of the function.

We choose to take the Kroupa IMF (Kroupa, 2001) to run the models for both the disk and bulge components. This IMF provides a more realistic fit to the low-mass end of the IMF rather than the most commonly used single-slope Salpeter IMF (Salpeter, 1955). The values for the α parameter of the Kroupa IMF are:

$$\alpha_1 = +0.30.7, \quad 0.01 \leq m/M_{\odot} < 0.08 \quad (4.32)$$

$$\alpha_2 = +1.30.5, \quad 0.08 \leq m/M_{\odot} < 0.50 \quad (4.33)$$

$$\alpha_3 = +2.30.3, \quad 0.50 \leq m/M_{\odot} < 1.00 \quad (4.34)$$

$$\alpha_4 = +2.30.7, \quad 1.00 \leq m/M_{\odot} \quad (4.35)$$

with mass limits $M_{inf} = 0.1M_{\odot} - M_{sup} = 100M_{\odot}$

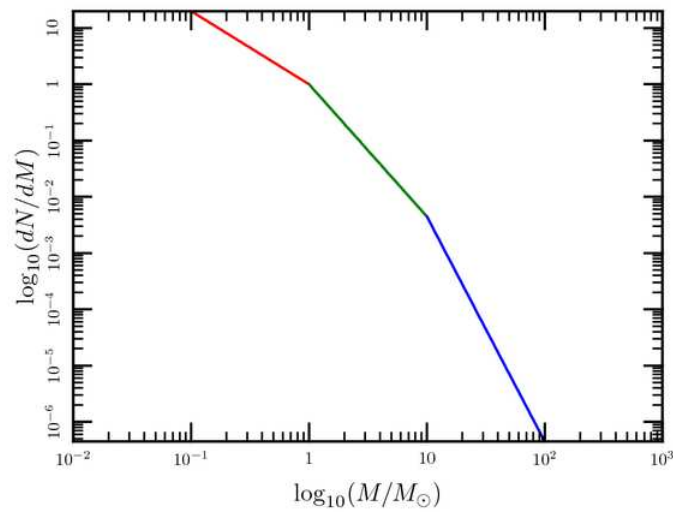


Figure 4.5: Kroupa Initial Mass Function. Source Kroupa (2005).

The star formation rate (SFR) has the form:

$$SFR = constant \times \sigma_{gas}^N \quad (4.36)$$

where σ_{gas} is the projected surface gas density and the exponent N is the slope of the power-law relation (Schmidt law) usually determined by HI observations. The star formation rate depends on local gas properties as the efficiency of stellar generation is mainly determined by the amount of gas available to form stars.

4.4.1 The disk stellar population

To model the disk's SFH, we assign a constant star formation rate, where after 8 Gyrs of star formation, it is suddenly truncated (Fig.4.6).

When truncation occurs, there is no more gas replenishing the galactic disk to form

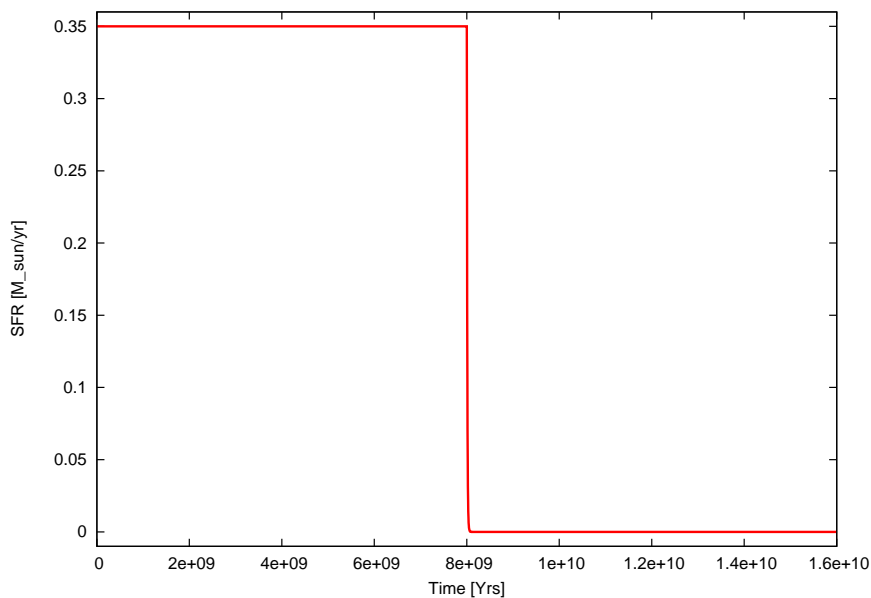


Figure 4.6: Star formation rate of the galactic disk of the galaxy model

stars (Fig.(4.4.1)) leading to an eventual decrease on the stellar mass of the galactic disk component Fig.(4.8).

GALEV models are chemically consistent, meaning that they combine the chemical evolution of the ISM abundances and the spectral evolution of the stellar population. These models use stellar evolutionary tracks, and stellar yields for a large range of metallicities and take in account the increasing initial abundances of suc-

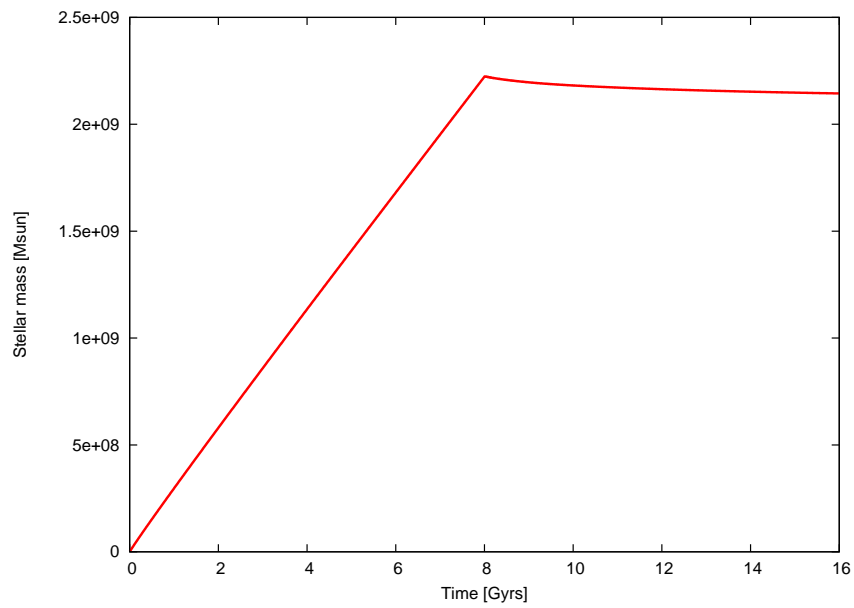


Figure 4.7: Galactic disk stellar mass

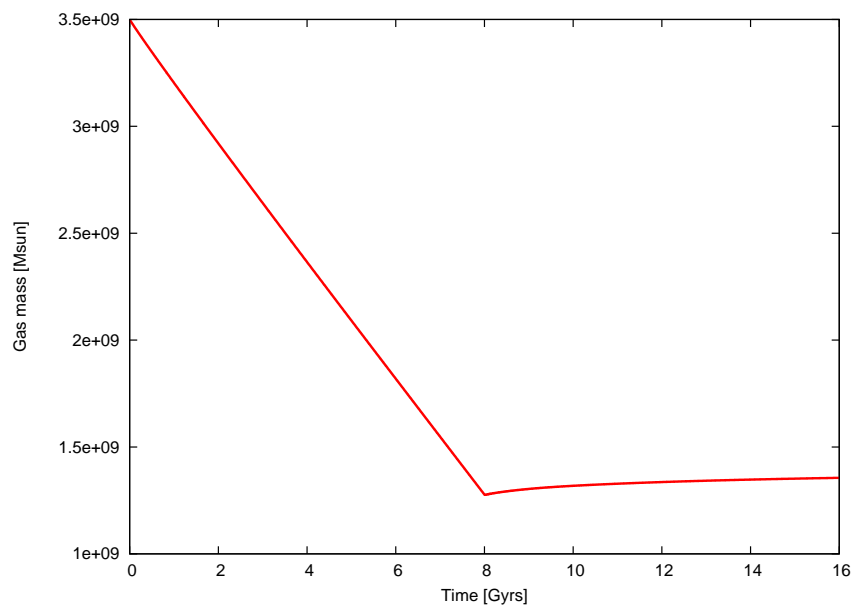


Figure 4.8: Galactic disk gas mass

cessive stellar generations. Fig (4.9) shows the metallicity evolution of the galactic disk component over time.

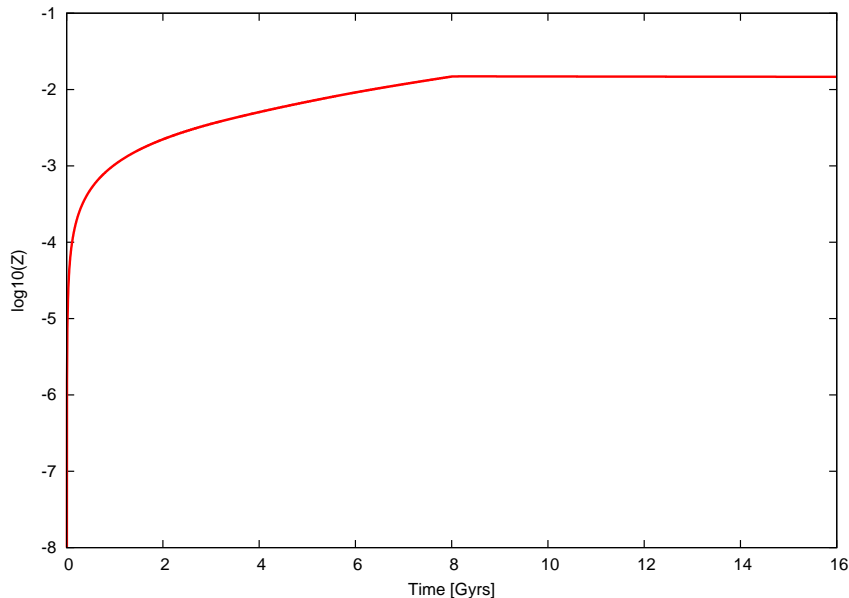


Figure 4.9: Metallicity evolution of the galactic disk.

4.4.2 The bulge stellar population

The SFH assigned to the bulge component is given by a exponential decaying short duration star forming burst that has the form:

$$SFR \propto e^{-(t/\tau)} \quad (4.37)$$

with an e-folding time $\tau = 1 \times 10^7 yrs$ Fig.(4.10). Figs.(4.11 and 4.12) show the time evolution of the mass and gas component. During the star forming burst the gas mass is transformed in stars, afterwards no more gas infall takes place leaving only the stars formed during the short SF burst.

The metallicity of the bulge is not self-consistent as in the case of the disk. We assign an initial metallicity Z_0 which evolution over time is shown in Fig.(4.13) This approach of assigning 'a priori' stellar populations to the luminous components of

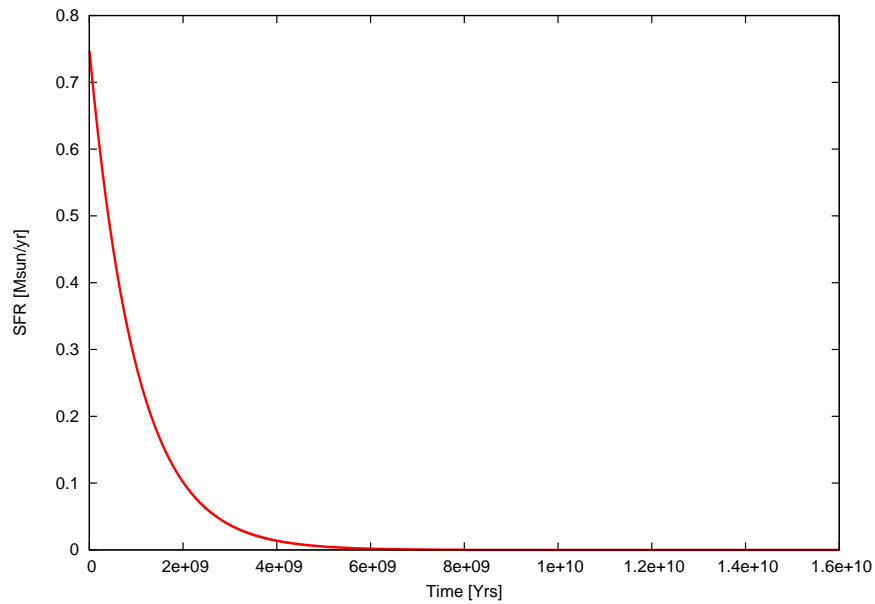


Figure 4.10: Star formation rate of bulge component of the galaxy model.

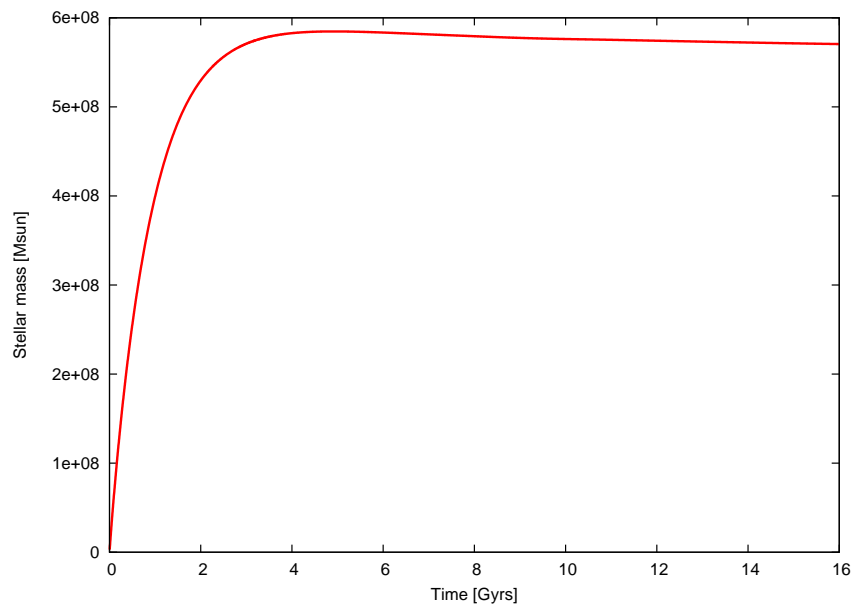


Figure 4.11: Stellar mass evolution of the bulge component. The SFR assigned follows an exponential decay with an e-folding time $\tau = 1 \times 10^7$ yrs.

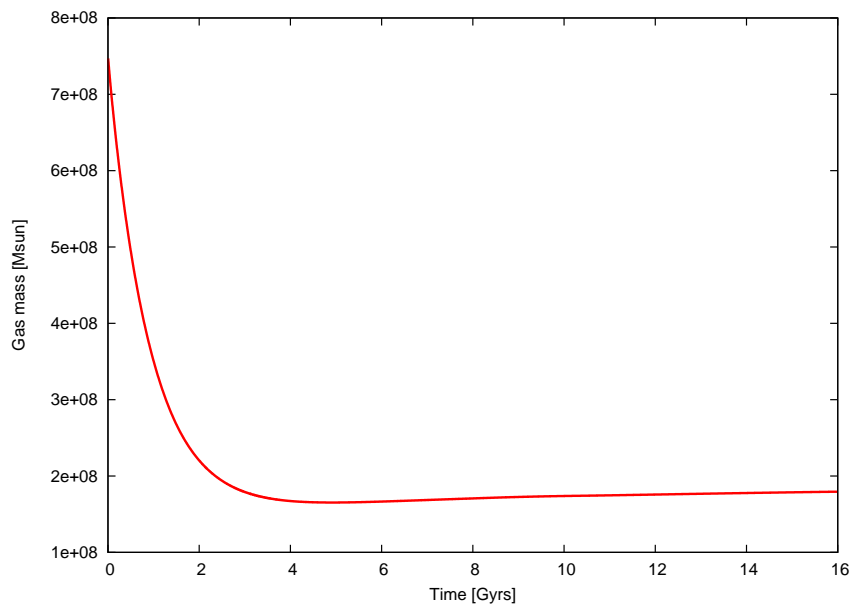


Figure 4.12: Evolution of the gas mass of the bulge component over time. The SFR assigned follows an exponential decay with an e-folding time $\tau = 1 \times 10^7 yrs$.

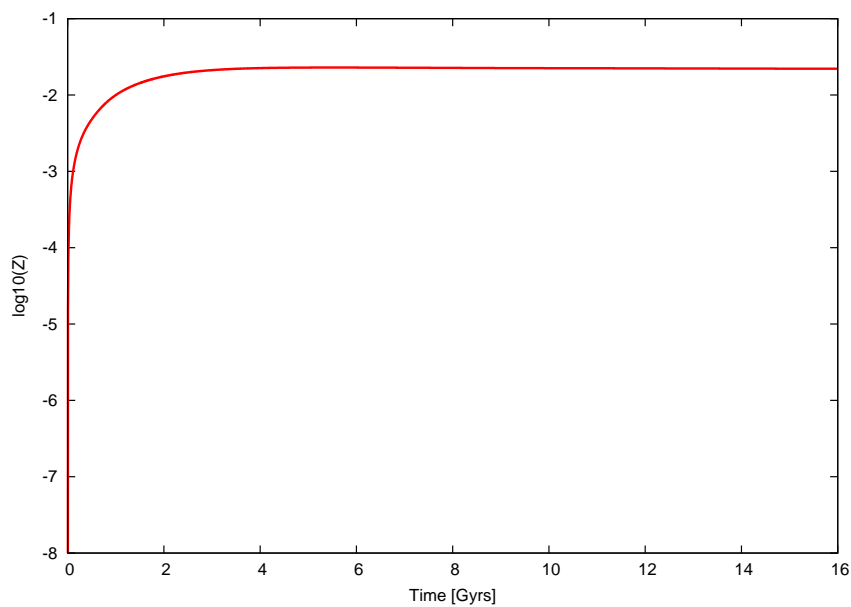


Figure 4.13: Metallicity evolution of the bulge mass component. The initial metallicity assigned is Z_0 .

the galaxy model is done through the GALEV models as it has been found in the test runs for the galaxy model performance when run within the Nbody6 GPU code. The disk presents instabilities which raise when using the stellar evolution scheme as the code reassigns a new mass to the original particle masses computed by the Salpeter (1955) models if the mean of the newly generated masses differ from the ones given by the initial conditions of the model.

The dynamical features originated by the disk instability are a consequence of the disk setup as the particles are generated with velocities independent of their individual masses. This could be fixed in the near future by modifying the of Kuijken Dubinski model generation program by generating the bulge and disk particles according to a given mass function and by scaling of particle velocities with their individual masses.

Chapter 5

Results

In this chapter, we will discuss the results of the simulation performed to account for the effects of the simulated Virgo cluster tidal field. Afterwards, the results that come out from simulating the harassment mechanism will be analyzed from the dynamical point of view as well as in terms of stellar evolution parameters derived for the initial model and the remnant galaxy after has suffered several encounters.

5.0.3 The effect of the tidal field

We set up a simulation of the Virgo cluster tidal field with the following parameters: The eccentric orbit traced by the galaxy's motion has an eccentricity $e = 0.9$. The galaxy begins to orbit well outside the virial radius at $R_{apo} = 3.2$ Mpc entering the galaxy cluster at $R_{vir} = 1.55$ Mpc. The galaxy moves across the galaxy cluster reaching the pericenter of its orbit at $R_{peri} = 165$ kpc. During its motion within the galaxy cluster, the dynamical and morphological properties of the infalling galaxy are affected by the strength of the tidal field exerted by the cluster's potential due to the gravitational interaction of both systems. The strength of the tidal field has a radial dependence as the forces exerted depend on the position of the galaxy relative to the cluster center.

While the galaxy travels towards the pericenter of its orbit, it begins to lose angular

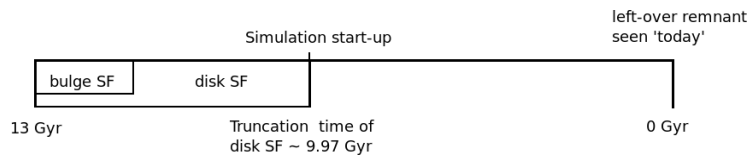


Figure 5.1: Schematic representation of the relevant time scales for the stellar evolution of the galaxy

momentum and kinetic energy while the potential energy increases preserving the equilibrium of forces between the cluster center and the galaxy. To achieve this equilibrium, the particles that conform the galaxy begin to get stripped away from the initial configuration as the binding energy is not sufficient anymore to keep the particles together.

The galaxy feels thus the combined effect of the tidal forces that act radially towards the cluster center, as it is a rotating system, it also feels the Coriolis force that results from the product of the angular momentum and the radial position vector.

In Figs 5.2 and 5.3 it is shown the variation of the tidal field strength in terms of the tidal energy that comprises both the centrifugal and the vertical tidal energies together with the Coriolis energy that the galaxy feels while passing through the galaxy cluster.

The halo particles that embed the stars that form the disk and bulge of the galaxy are the first on feeling the effect of the tidal field as they belong to the outer component of the galaxy. This effect gets stronger when the galaxy is approaching the cluster center as the relative distance between the galaxy and the core of the cluster decreases, thus feeling more intensively the gravitational attraction of the cluster tidal field.

Throughout the simulation, the galaxy continues its motion after passing the first pericentric passage completing three orbits. The galaxy's orbital period is of $P_{orbit} \approx 3$ Gyrs, thus, we follow its evolution in the cluster for about 9 Gyrs.

When the simulation begins, the three galaxy components are smooth and don't present any substructure (Fig 5.4). We run a 100,000 particle simulation where the particles are distributed in the following way:

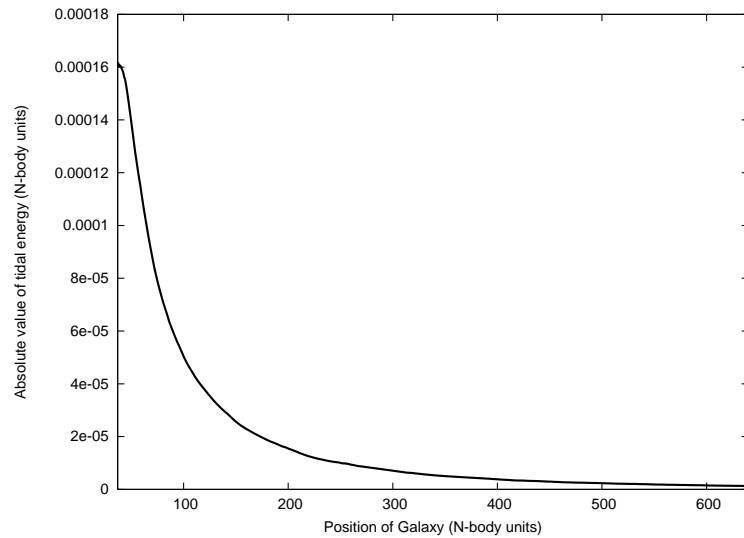


Figure 5.2: Tidal energy as a function of galaxy's position relative to the cluster center in N-body units.

- 50,000 particles for the halo component
- 40,000 particles for the disk component
- 10,000 particles for the bulge component

Figures (5.6 and 5.7) show the time evolution of the galaxy under the effect of the tidal field:

After few Myrs the halo particles begin to get stripped away due to the strength of the field which becomes stronger once the galaxy enters the galaxy cluster. The galactic disk heats up due to the heat provided by the interaction making its disc scale height increase its value, what results on making the disk thicker than it was at the beginning of the simulation (Fig 5.5).

The mass loss begins to be noticeable at around 1 Gyr. The halo component is

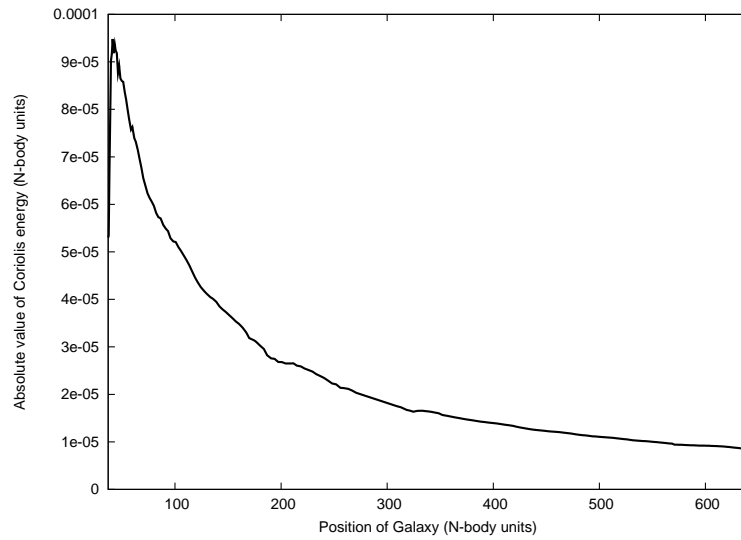


Figure 5.3: Coriolis energy as a function of galaxy's position relative to the cluster center in N-body units.

mainly affected losing at the end of the simulation the 60% of its original mass in the total time evolution 9 Gyr.

The galactic disk loses about the 13% of its original mass and the bulge component 7%.

In Fig ??, the number distribution of the three components is shown as a function of time. The galaxy begins to orbit outside the cluster, so that the mass loss is not noticeable until it enters the cluster. Halo particles are removed faster and easier than the particles that conform the disk and bulge. It is very important to see the

Figure 5.4: Projected particle positions of the three galaxy components. In red: halo; green: disk, blue: bulge

effect of the tidal field alone before starting the harassment simulations as we can quantify how much material is lost due to the gravitational interaction with the

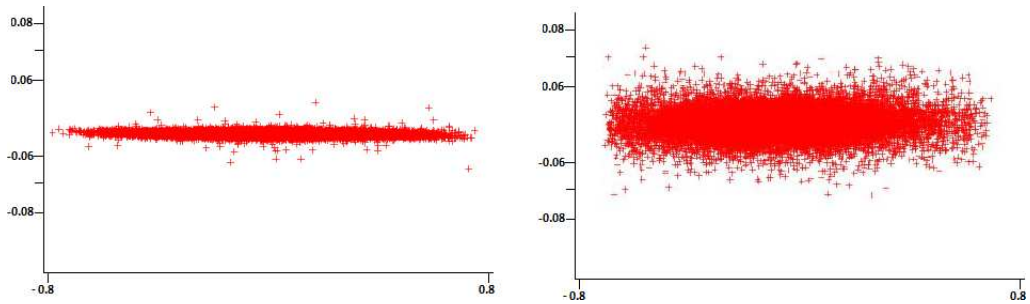


Figure 5.5: Disk thickening caused by tidal heating. Right figure: Disk at beginning of the simulations. Left figure: Disk after one orbital period of the galaxy within the galaxy cluster has been completed.

cluster tidal field.

5.0.4 The galaxy harassment effect

To explore the strength of the galaxy harassment effect, we choose to take an orbit with eccentricity $e = 0.55$. Its apocentric distance is of $R_{apo} = 340$ kpc $R_{peri} = 80$ kpc. The galaxy orbits the galaxy cluster center for about 3 Gyrs where it encounters several galaxies through its orbital passages.

For testing this scenario, we choose to place the galaxy well inside the galaxy cluster as we want to quantify the effects of harassment, more over, to set an upper limit and see what happens to the galaxy when 'extreme' harassment occurs.

To account for the effects of this extreme but still probable scenario, we make the galaxy encounter several perturbers by setting a probability threshold that works in the following way:

By construction, the probability of having an encounter in the simulation is timestep dependent. It depends also on an 'average encounter probability' per orbit, which we set to the value of $p = 0.01$ at each timestep, and the number of encounters

N_{enc} we will have during these timesteps.

The probability is given by:

$$N!/((N - N_{enc})!N_{enc}!)x0.99^{(N - N_{enc})}x0.01_{enc}^N \quad (5.1)$$

where N is the number of time steps.

In this way, we 'force' the encounter random number generator to find a perturber more often in the same number of timesteps than we would have without this upper encounter limit but the probability of this to happen is less likely than in the conventional scenario.

The results of this simulation scenario are illustrated in Figs 5.8 and 5.9. Here both, the strength of the tidal field and the harassment mechanism act along together.

The galaxy suffers five encounters in total over the 3 Gyrs that spends passing within the galaxy cluster. According to our simulations, the tidal field is mainly driving this transformation and just 13% of the galaxy's mass loss is due to galaxy encounters.

We do not find harassment so effective even when we simulate the extreme harassment scenario. Alike Smith et al. (2010), where he states in his conclusions that: "Harassment of small late-type dwarf galaxies that have recently been accreted into the cluster is not an effective mechanism for forming the thickened discs of dwarf ellipticals."

They explore the galaxy harassment scenario via close encounters for one orbital passage of a low-mass disk galaxy that infalls in the Virgo cluster. Although they do not evolve the model further than one orbital period, they conclude that the orbit where the galaxy travels across the cluster determines the strength of these mechanism. Galaxies in small eccentric orbits at small apocentric distances are more

likely to have an encounter due as they orbit the cluster center in a smaller time interval than a galaxy that is falling into the cluster from outside in a radial orbit.

In tests performed in order to test our numerical simulations it was found that when having a realistic orbit as the one described at the beginning of this chapter to test the strength of the tidal field, the chance of having an encounter with another galaxy is highly improbable as the pericentric distance of such an orbit is too far from the galaxy cluster center, where the density is higher and thus, encounters are far more probable to occur.

Mastropietro et al. (2005) simulates galaxy harassment finding harassment very effective to drive the morphological transformation from disks to dE like galaxies. Probably this is due to the fact that the galaxy that turns to be extremely harassed always orbit along the densest part of the cluster plus they make the galaxy travel several orbits throughout the simulation.

5.0.5 Image photometry

We want to compare the 3-D information obtained through the numerical simulations with the data provided by the SDSS survey data. For this it is necessary to transform this information in color distributions and in structural parameters. For this we map the 3-D data obtained into 2-D distributions as if the galaxy would be observed from a certain position in order to make a proper comparison with the SDSS data for the VC.

Each component of the galaxy is tagged in order to identify each particle and know to which component it belongs. We map then the flux of each luminous component (disk and bulge) by first calculating the apparent magnitude at Virgo distance in the following way:

$$m_{ap_d} = 5\log_{10}(D_L) - 5 + M_{disk} \quad (5.2)$$

$$f_d = f_0 * 10^{-0.4*(m_{ap_d}/M_{*d})} \quad (5.3)$$

$$m_{ap_b} = 5\log_{10}(D_L) - 5 + M_{bulge} \quad (5.4)$$

$$f_b = f_0 * 10^{-0.4*(m_{ap_b}/M_{*b})} \quad (5.5)$$

$$f_{tot} = f_{disk} + f_{bulge} \quad (5.6)$$

Once we obtain these flux maps, we make photometry over each image for each of the SDSS bands u, g ,r ,i ,z using the photometry software AMOR (Lisker,2006).

The AMOR software has been designed for computing the morphological parameters of galaxies. It creates stamp images of a given source. In our case, we create FITS images of the galaxy for the initial conditions and for the time steps after an encounter occurs. This time steps are the 'look-up' times we look at after the encounter occurs what is about 100 Myrs after it happens. This time is chosen as it is considered to be the time it takes to the galaxy to show the features originated by the harassment mechanism.

We run first AMOR on the SDSS r-band image for the initial conditions model and afterwards for the subsequent snapshot images after each encounter, with a circular aperture. It recomputes the initial input parameters required to obtain the stellar structure and outputs back the right elliptic aperture required to calculate accurately the galaxy flux and thus, outputting finally more accurate values of the galaxy's structural parameters.

The parameters obtained using the AMOR software are given in the tables 5.1 and 5.2.

Name	M_r	μ_{eff}	r_{eff}	$r_{eff}(arcsec)$	$1r_{petr}$
remnant	13.885	24.454	130.947	51.855	176.963
5 th	13.855	24.346	126.325	50.025	177.924
4 th	13.763	24.136	119.634	47.375	175.935
2 nd	13.560	23.312	89.889	35.596	154.987
initial	13.393	22.320	61.643	24.340	115.974

Table 5.1: Structural parameters derived from the galaxy photometry.

Name	u_{ap}	g_{ap}	r_{ap}	i_{ap}	z_{ap}	$g - i$	$u - r$	$i - z$
remnant	16.484	15.037	14.306	14.005	13.734	1.032	2.178	0.271
5 th	16.425	14.978	14.248	13.947	13.676	1.031	2.177	0.271
4 th	16.282	14.845	14.122	13.824	13.554	1.021	2.160	0.270
2 nd	15.932	14.513	13.807	13.515	13.248	0.998	2.125	0.267
initial	15.692	14.289	13.602	13.317	13.054	0.972	2.090	0.263

Table 5.2: Galaxy colors derived from the galaxy photometry.

5.0.6 Structural parameters

The galaxy encounter simulation starts right after the SF in the galactic disk has been truncated at 9.97 Gyrs. Throughout the simulation, the galaxy experiences several galaxy encounters with other cluster members as seen in the previous section. The combined effect of both tidal forces and galaxy encounters, results in a change in the galaxy morphology but it is also reflected in the evolution of its stellar populations. We analyze the stellar evolution of such populations keeping track of them since the galaxy is placed initially in the galaxy cluster and begins to orbit around the center. We look at the stellar properties of the harassed galaxy every 100 Myrs after an encounter has occurred and we place the structural parameters that were extracted from the photometry at each 'look-up' time.

The preceding plots show the relations between the structural parameters ob-

tained while doing the photometry of the snapshot images obtained after looking after each of the encounters that the galaxy underwent.

The stripping of luminous material caused by the tidal interactions that the galaxy suffers, can be expressed in terms of the relation between effective surface brightness, effective radius and subsequently, represented by the colors derived from this structural properties.

To understand the structural parameters of the galaxy, we compare the initial values of such parameters to the ones obtained after the galaxy loses material by a mix of the tidal field plus encounters with other galaxies.

The effective radius of the galaxy should shrink as a consequence of the loss of luminous mass. This affects the surface brightness of the galaxy together with a change of its initial absolute magnitude.

One would expect that this results in a fainter object which surface brightness is decreasing as the effective radius should be smaller every time. Though, in our simulation results, the initial galaxy expands its length over the time and the particles that initially formed the bulge begin to spread out towards the disk component. It can be due to an artifact of the Nbody simulations as the 'self-consistent' approach initially provided by the Kuijken and Dubinski (1995) models as probably, is not suitable for galaxies that will suffer such a strong halo mass loss as the one our galaxy experiences in our simulations. The concept of self consistency is strongly linked to the halo that embeds the galaxy. The fact of losing the halo particles due to the mixed effect of the tidal field together with the close encounters that the galaxy experiences might cause the disk and bulge components to be stripped away from their initial configuration resulting in an expansion of the disk and bulge length relative to the initial setup.

In terms of the colors derived, the remnant galaxy is placed in the red sequence while the initial model, i. e., the disk galaxy to be harassed lies still in the edge of

the blue cloud as seen in Fig (5.14).

To understand the age-metallicity relation, we plot the derived colors $u - r$ vs $i - z$ that turn to be good age -metallicity tracers. The initial disk galaxy is younger than the remnant galaxy but there is no metallicity gradient as indicated in Fig. (5.15). It would have been expected that the galaxy becomes more metal rich as it ages but the metallicity gradient between the initial model and the remnant is not steep meaning that there is basically no metallicity evolution in the galaxy.

We analyze the effect of the harassment mechanism based in the effective radius of the galaxy, its effective surface brightness, and the SDSS magnitudes and colors. The galaxy has a surface brightness of when infalls in the galaxy cluster, the luminous mass loss due to the combined effect of harassment and tidal field leads to an eventual decrease in the galaxy's surface brightness.

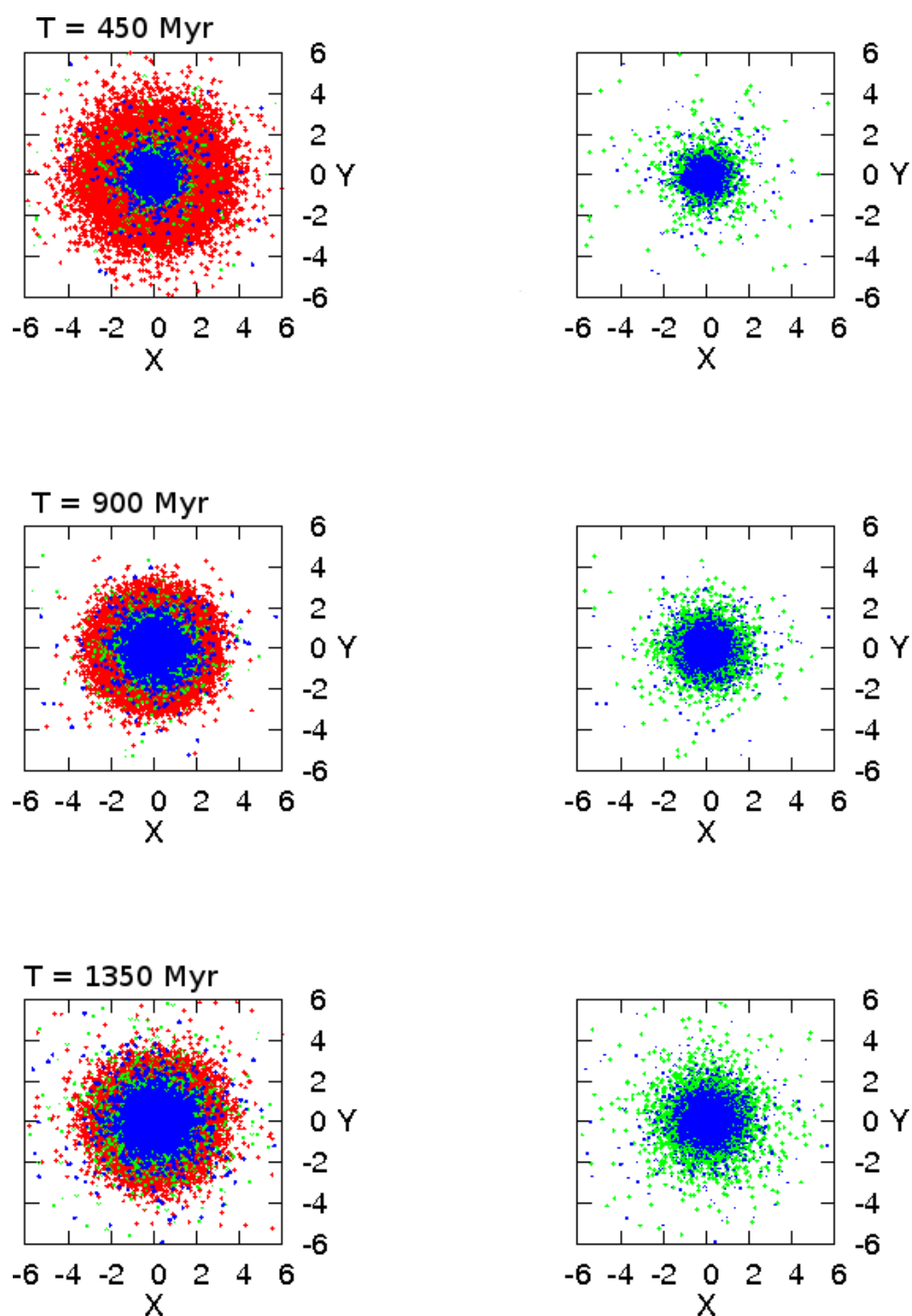


Figure 5.6: Time evolution of the galaxy embedded in the Virgo galaxy cluster field. The figure shows the projected particle positions for the three galaxy components in N-body units (1-Nbody length unit = 5 kpc). The left side figures show the same projection for the disk and bulge component.

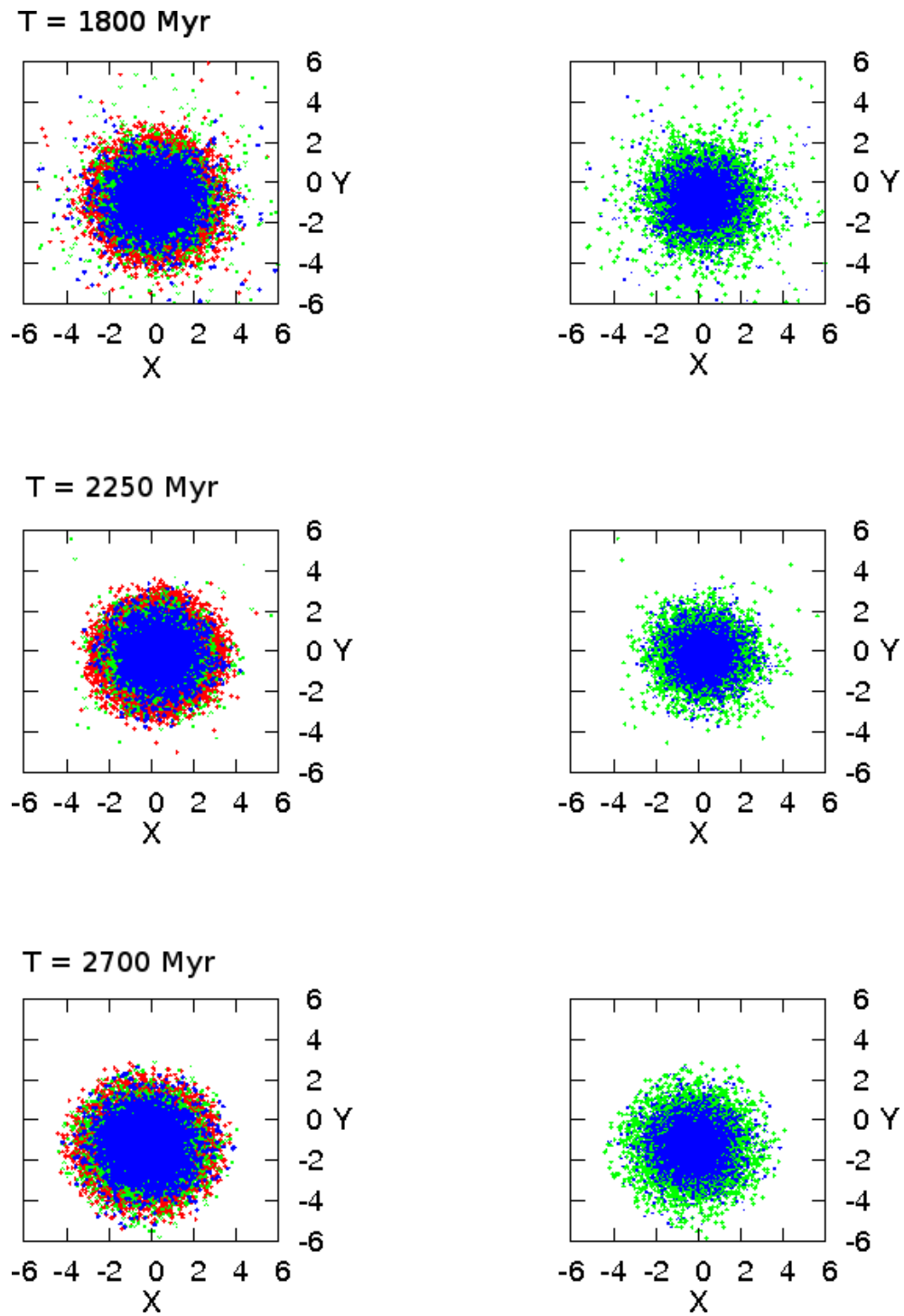


Figure 5.7: Time evolution of the galaxy embedded in the Virgo galaxy cluster field. The figure shows the projected particle positions for the three galaxy components in N-body units (1-Nbody length unit = 5 kpc). The left side figures show the same projection for the disk and bulge component.

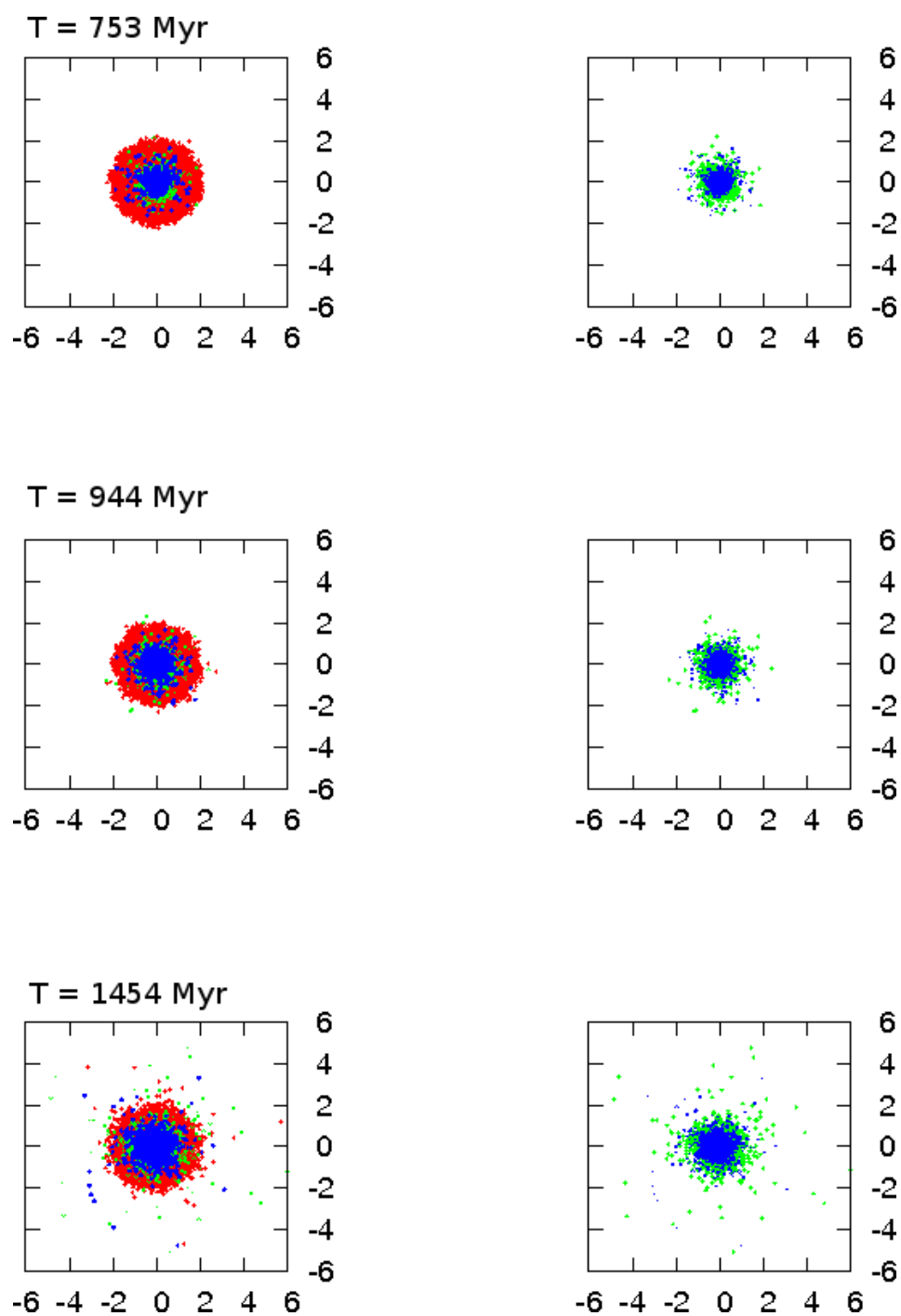


Figure 5.8: Time evolution of the galaxy embedded in the Virgo galaxy cluster field under the effect of the tidal field forces and encounters with other galaxies. The figure shows the projected particle positions for the three galaxy components in N-body units (1-Nbody length unit = $5kpc$). The left side figures show the same projection for the disk and bulge component.

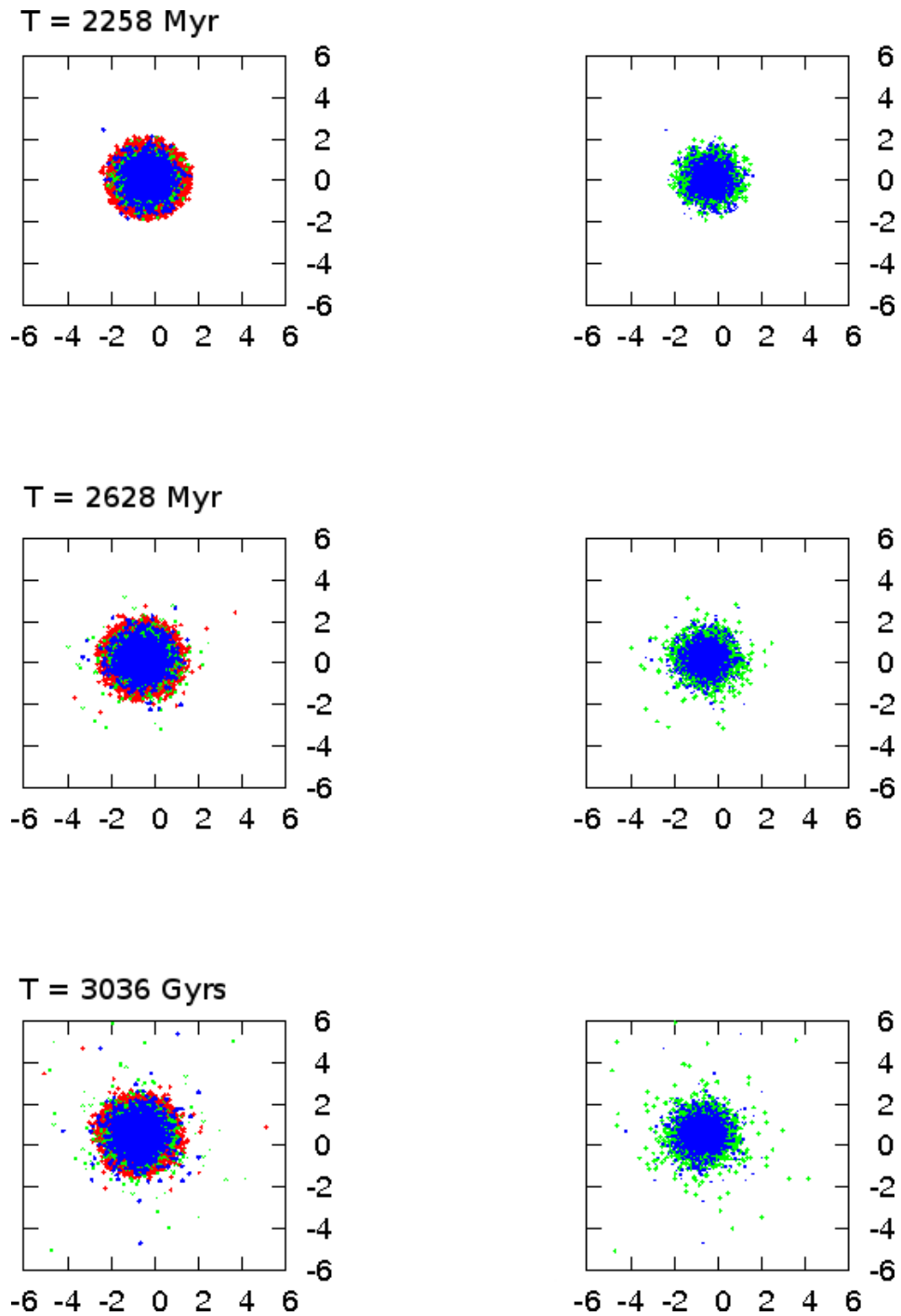


Figure 5.9: Time evolution of the galaxy embedded in the Virgo galaxy cluster field under the effect of the tidal field forces and encounters with other galaxies. The figure shows the projected particle positions for the three galaxy components in N-body units (1-Nbody length unit = 5 kpc). The left side figures show the same projection for the disk and bulge component.

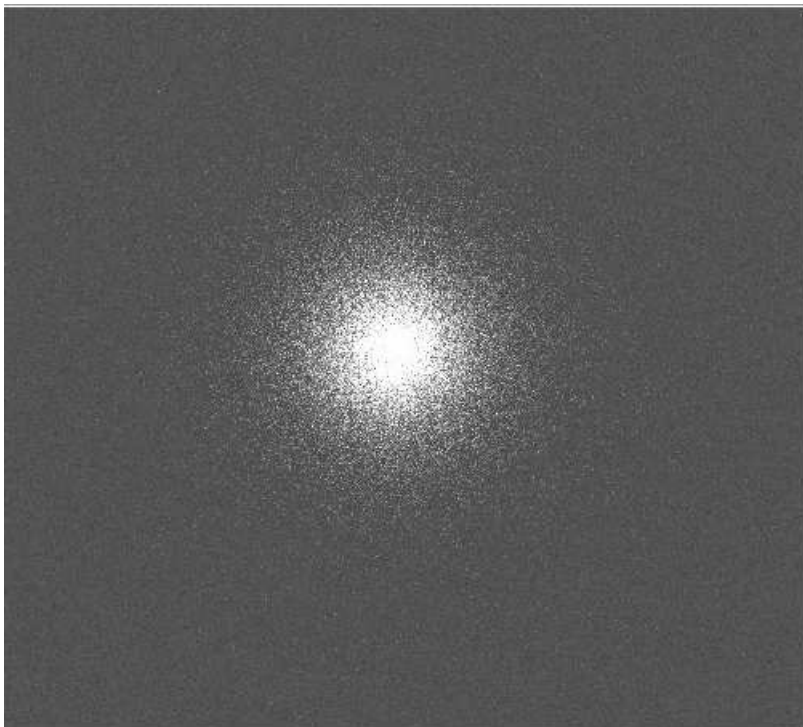


Figure 5.10: Galaxy remnant at the end of the simulation.

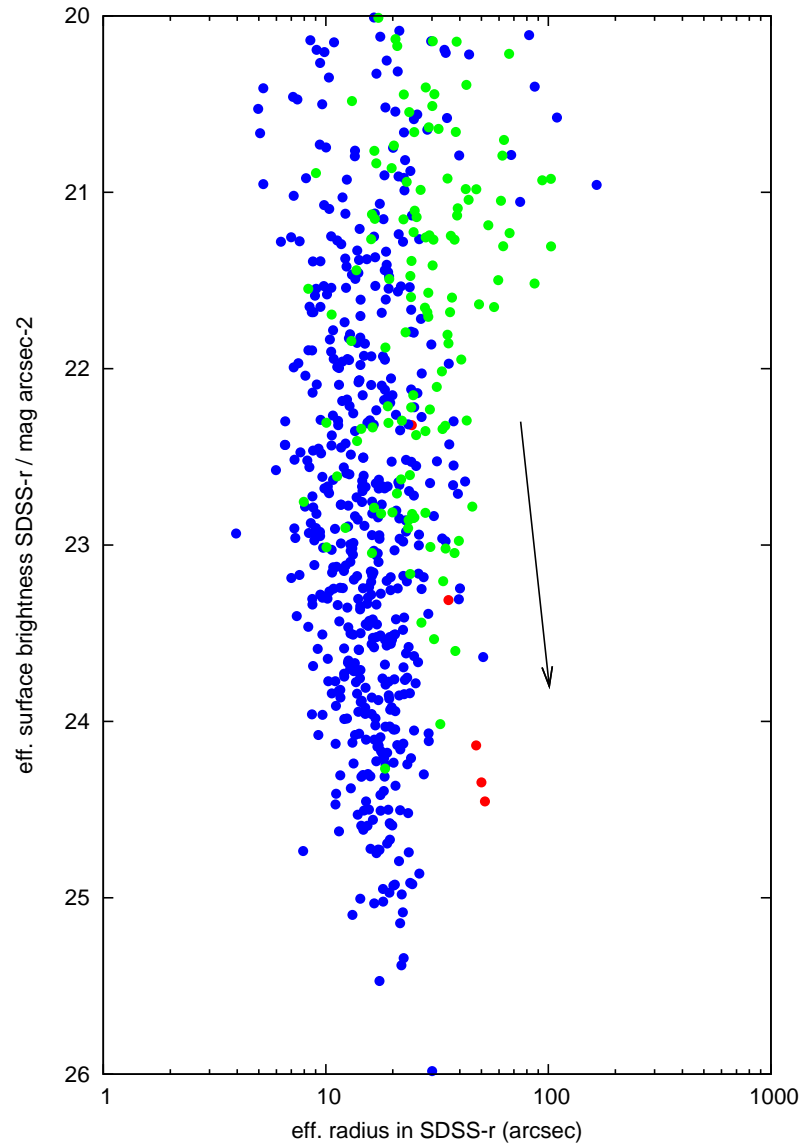


Figure 5.11: Effective surface brightness versus effective radius. The red dots represent the initial model and the subsequent stages after encounters have occurred. The arrow points towards the final stage (remnant galaxy). In blue: early-type galaxies. In green: late-type galaxies.

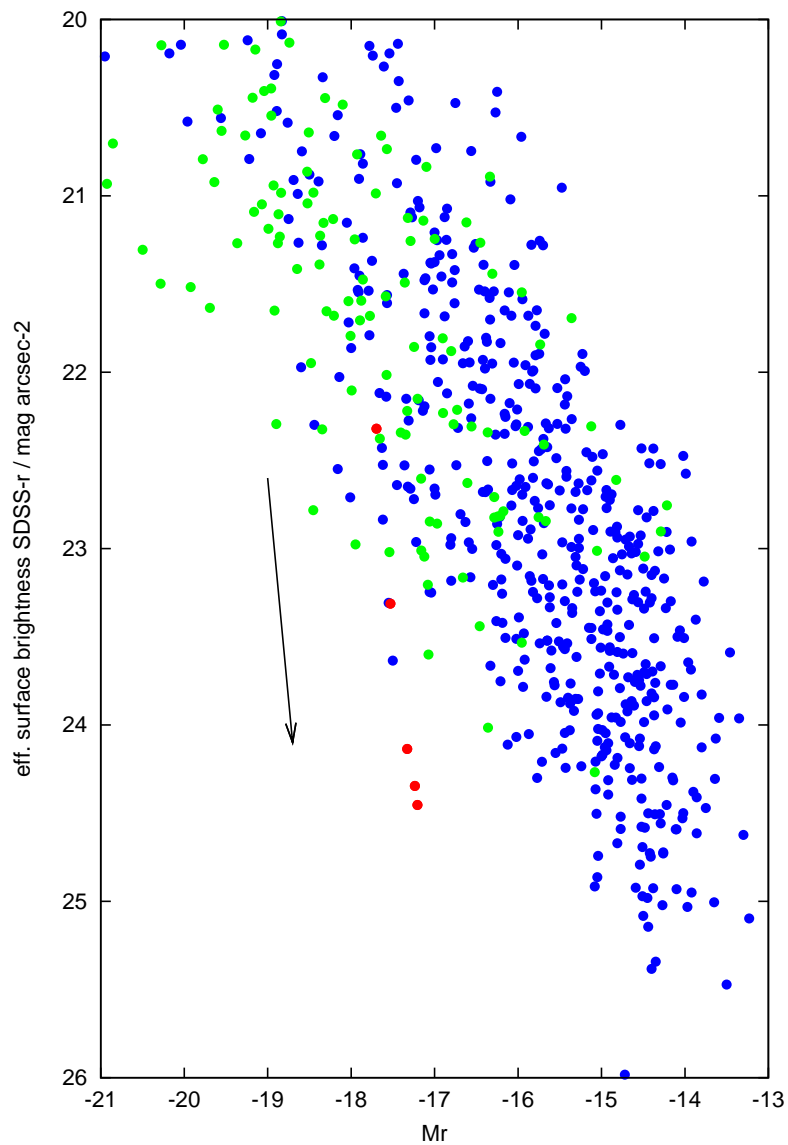


Figure 5.12: Effective surface brightness versus SDSS-r absolute magnitude M_r . The Virgo distance modulus is $M - m = 31.09$. The red dots represent the initial model and the subsequent stages after encounters have occurred. The arrow points towards the final stage (remnant galaxy). In blue: early-type galaxies. In green: late-type galaxies.

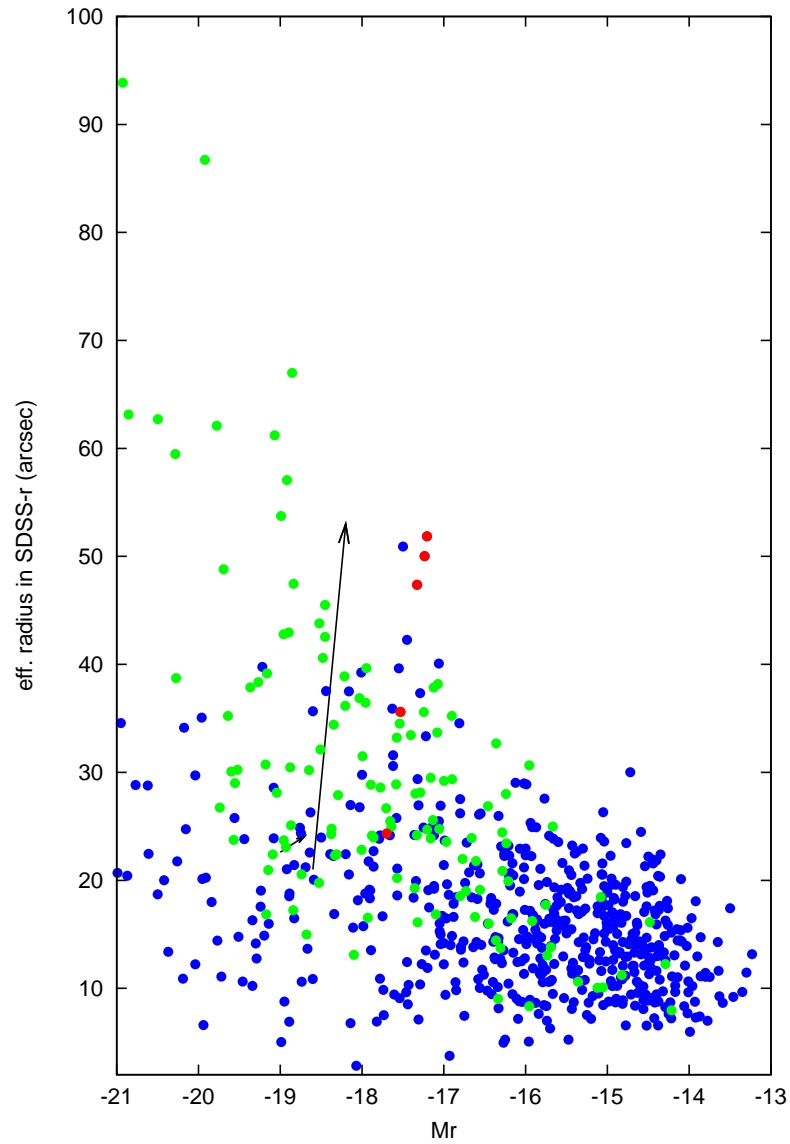


Figure 5.13: Effective radius versus SDSS-r absolute magnitude M_r . The Virgo distance modulus is $M - m = 31.09$. The red dots represent the initial model and the subsequent stages after encounters have occurred. The arrow points towards the final stage (remnant galaxy). In blue: early-type galaxies. In green: late-type galaxies.

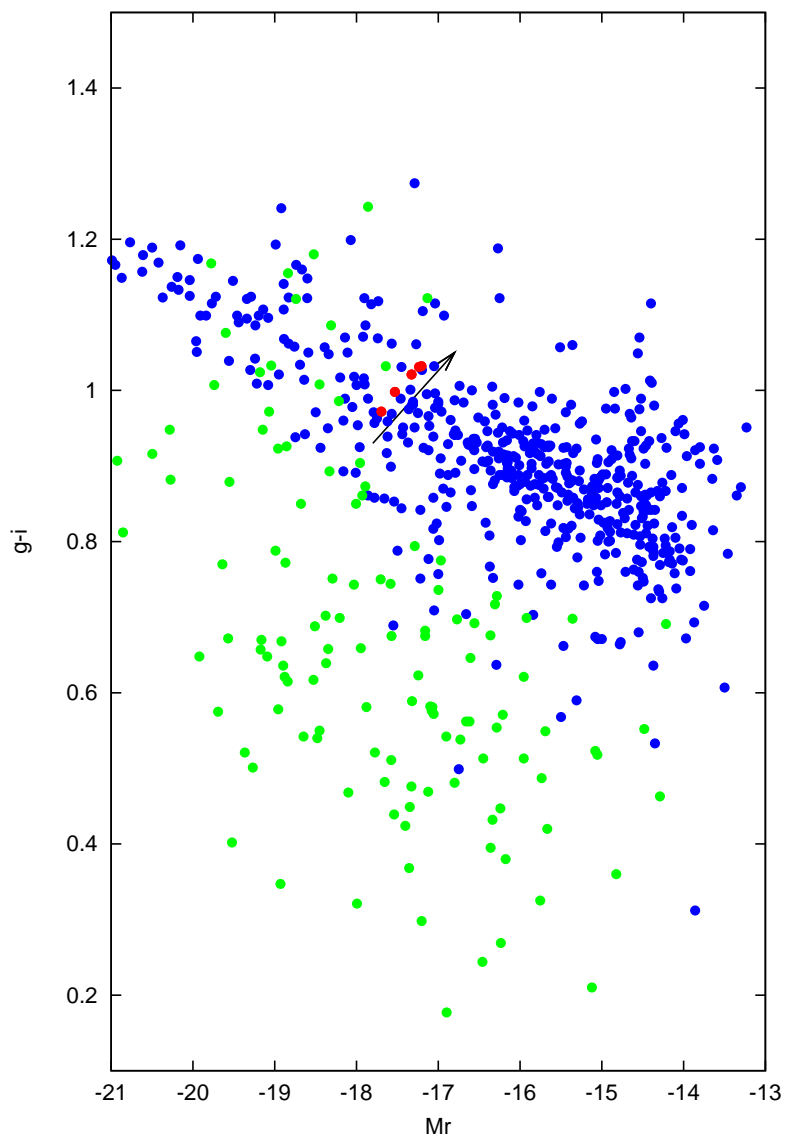


Figure 5.14: SDDS color - magnitude diagram: $g - i$ vs absolute magnitude M_r . The Virgo distance modulus is $M - m = 31.09$. The red dots represent the initial model and the subsequent stages after encounters have occurred. The arrow points towards the final stage (remnant galaxy). In blue: early-type galaxies. In green: late-type galaxies.

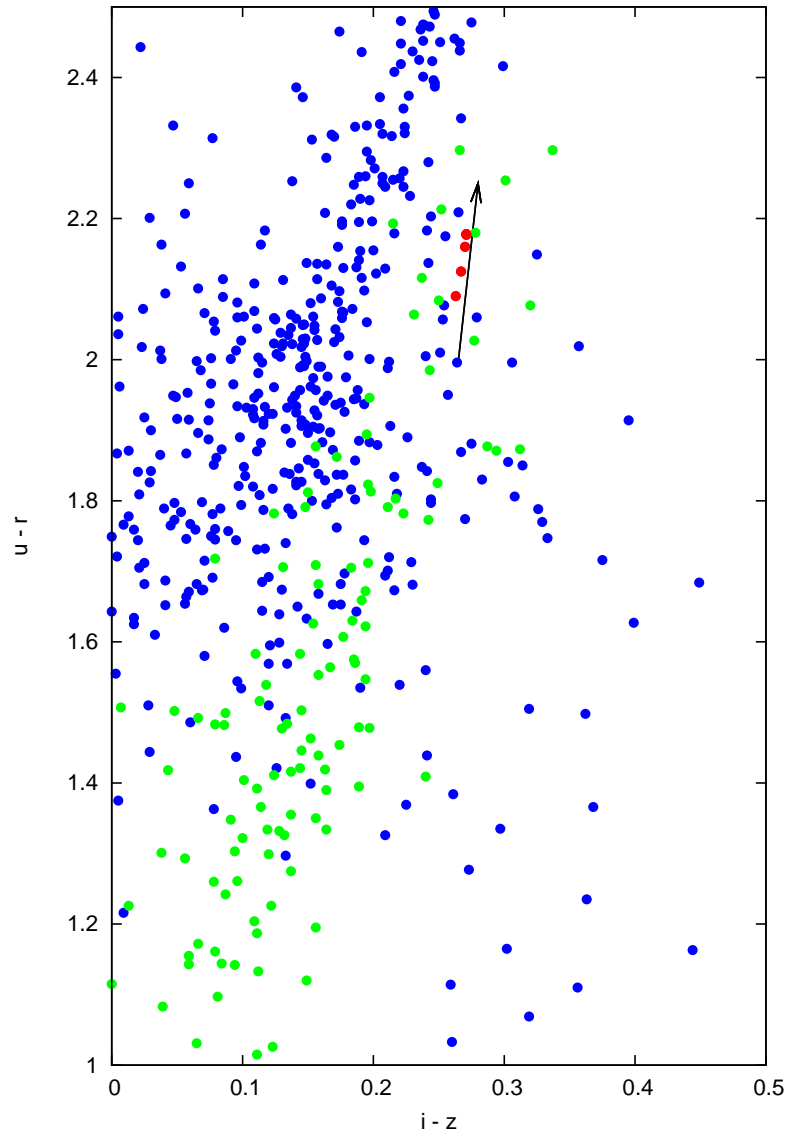


Figure 5.15: SDDS color-color diagram: $u-r$ vs $i-z$. The red dots represent the initial model and the subsequent stages after encounters have occurred. The arrow points towards the final stage (remnant galaxy). In blue: early-type galaxies. In green: late-type galaxies

Chapter 6

Discussion

Several works have provided different clues about the origin of low-mass early-type galaxies. It is clear that environment plays a key role on the morphological transformation of disk galaxies into early-type like. We have aimed to provide new evidence on trying to understand how the physical mechanisms that take place in galaxy clusters affect the morphology and the stellar structure of those galaxies that infall into galaxy clusters. It is clear that none of these effects act independently of each other intermixing together to cause such transformations.

As it has been mentioned, through this work, we use a direct integration Nbody simulation code and later on we transform the output by assigning two different stellar evolution star forming histories to the two luminous components of the simulated galaxy (bulge and disk) by transforming the structural parameters that come out from evolving the initial conditions of our simulation setup.

We have found that the the tidal field exerted by the cluster potential is the main driver of such transformation. It is important then to compare the different ways that several authors have used to carry out their simulations. Through this work, some comparisons between the results obtained and the ones obtained by other authors have been pointed out. Though, to enable a proper comparison in order to distinguish their results from the ones obtained in this work, it is practical to point out the main differences on how they have performed the simulations and the initial

conditions of the galaxy model that later on will experience close encounters with other galaxies.

The differences between the numerical simulations that have been carried out can be categorized mainly by the different Nbody simulation codes used, the initial conditions and the orbits that the galaxy follows within the galaxy cluster.

Probably it is easier to first look at the results obtained as starting point and later on distinguish the differences between all the simulation setups in order to find whether this is really an essential driver in the results.

The main question is, whether harassment really plays such a key role on driving the morphological transformation from a disk into a spheroidal shape like galaxy.

Moore et al. (1998) and Mastropietro et al. (2005) find out that galaxy harassment is the main driver of such evolution as well as the work published by Aguerri and González-García (2009). Interestingly, Smith et al. (2010) and the work carried out in my thesis work do not find harassment as the main driver of such morphological transformation. It comes then into play, the orbital setup of all this different works.

Moore et al. (1998), Mastropietro et al. (2005) and Smith et al. (2010) use a tree-code SPH Nbody simulation code taking into account a gas component. We do not have a gas component but we take into account the mass loss of the galaxy by assuming that already lost part of its mass before falling into the cluster. We diminish the initial mass of the galaxy by a factor of ≈ 1.5 of the initial mass taken by Mastropietro et al. (2005).

The fact of placing the galaxy already in the galaxy cluster at small apocentric distances from the cluster center is the most probable key to determine if harassment plays or not such a big effect. The number of passages through the cluster center and the pericentric distance are one of the determining factors that make this

harassing effect stronger.

It is natural then to think that the closer the galaxy is and the more orbits the galaxy completes, the stronger the harassment effect the galaxy will suffer as seen in Mastropietro et al. (2005), who places the galaxy at small apocentric distances. Being aware of this as referenced in their paper, Smith et al. (2010) place the galaxy well inside the cluster and follow its evolution through a first orbital passage. They do not follow this evolution later on as their galaxy model is not suitable for long evolutionary times as their model depends on the galaxy cluster mass which varies through time.

Knowing the strong effect that harassment has with these setups, we explore a similar scenario as we intend to investigate the extreme harassment effect that a galaxy embedded in a galaxy cluster can suffer as it was already mentioned in the results chapter.

Smith et al. (2010) describe in a very detailed way, how the eccentricity of the orbit that the galaxy follows is essential for this evolution. The closer the galaxy is to the pericenter and the less eccentric it is, the stronger the effect will be. This is due to the fact that the galaxy follows an orbit where the galaxy number density is higher and so the probability of having an encounter increases plus the fact that if the orbit is less eccentric, it will take more time to the galaxy to leave the pericenter.

In reality, when a galaxy infalls in a galaxy cluster, it follows a radial orbit beginning its passage well outside the virial radius of the cluster.

One can conclude then, that simulations that place the galaxy within the cluster at small apocentric distances will be more harassed, also because the orbital period is smaller making the galaxy complete several orbits accentuating the harassment effect.

What concerns the initial conditions setup might also play a role in the results

that come out from the simulations. While we model a three-component galaxy as well as Aguerri and González-García (2009), the above mentioned authors have a different initial conditions setup. They model the disk luminous component without taking into account the effect of the bulge.

Dynamically, the bulge component contributes to the galaxy's motion what as first sight it is noticeable when computing the circular velocity of the galaxy. It should be expected then, that the dynamics of the galaxy might variate somehow even if we cannot really quantify this variation as we did never follow the time evolution of a pure disk galaxy in our simulations. From the stellar population perspective, it has been shown that the stellar population of bulges do play a role in the stellar parameters derived from the photometry analysis of a galaxy, thus, being a more realistic approach.

Conclusions

We have found that the main driver for transforming disk galaxies into dE's is the tidal stripping due to the tidal field cluster potential.

This effect is able to strip the halo component and thicken the disks of infalling galaxies into galaxy clusters. Encounters with other galaxies make this effect stronger though we haven't found this mechanism to be the main driver of such mass loss and change in morphology.

It would be necessary to perform galaxy simulations with other initial conditions such as the bulge density to see whether this effect gets stronger depending on the bulge structure of the galaxy. So far, we have performed the harassment simulations with a bulge that is not compact as we try to reproduce an Sc like galaxy. Still, it would be interesting to vary the bulge density in order to account for differences in the morphological structure of the galaxy when harassment occurs.

The halo mass should be increased also to test the recent results obtained by Moster et al. 2010 whose work concludes that galaxies are embedded in dark matter halos that are a factor of 10 more massive than the galaxy dark matter halo used in this simulation.

From the N-body simulation perspective, it would be necessary to increase the number of particles in order to have a better resolution in the components of the galaxy model. Probably increasing the number of particles by a factor of 10 would

help to resolve better the effects in the structure of the modeled galaxy. In this respect, it is also an advantage to have access to the GPU cluster hosted at NAOC in Beijing, China which power would let us run in a near future simulations with higher number of particles in the order of 10^6 .

Moreover, it would be necessary to obtain the stellar evolution parameters directly from the Nbody6 GPU code. In the near future it is planned to modify the pre-existing routines already enabled in the Nbody6 GPU code to be suitable for working in these galaxy evolution framework instead of using the stellar evolution approach that we have used in this work using stellar evolution models of GALEV.

Bibliography

- S. J. Aarseth. Dynamical evolution of clusters of galaxies, I. , 126:223–+, 1963.
- S. J. Aarseth. From NBODY1 to NBODY6: The Growth of an Industry. , 111: 1333–1346, November 1999. doi: 10.1086/316455.
- J. A. L. Aguerri and A. C. González-García. On the origin of dwarf elliptical galaxies: the fundamental plane. , 494:891–904, February 2009. doi: 10.1051/0004-6361:200810339.
- A. Ahmad and L. Cohen. A numerical integration scheme for the N-body gravitational problem. *Journal of Computational Physics*, 12:389–402, 1973. doi: 10.1016/0021-9991(73)90160-5.
- H. Arp. Lines of Galaxies from Radio Sources. , 80:129–+, April 1968. doi: 10.1086/128602.
- K. Bekki and M. Chiba. Formation of the Galactic Stellar Halo. I. Structure and Kinematics. , 558:666–686, September 2001. doi: 10.1086/322300.
- B. Binggeli, A. Sandage, and G. A. Tammann. Studies of the Virgo Cluster. II - A catalog of 2096 galaxies in the Virgo Cluster area. , 90:1681–1759, September 1985. doi: 10.1086/113874.
- B. Binggeli, A. Sandage, and G. A. Tammann. The luminosity function of galaxies. , 26:509–560, 1988. doi: 10.1146/annurev.aa.26.090188.002453.
- J. Binney and S. Tremaine. Book Review: Galactic dynamics. / Princeton U Press, 1988. , 326:219–+, March 1987.

- C. J. Conselice, J. S. Gallagher, III, and R. F. G. Wyse. Galaxy Populations and Evolution in Clusters. I. Dynamics and the Origin of Low-Mass Galaxies in the Virgo Cluster. , 559:791–811, October 2001. doi: 10.1086/322373.
- A. Dressler. Galaxy morphology in rich clusters - Implications for the formation and evolution of galaxies. , 236:351–365, March 1980. doi: 10.1086/157753.
- N. W. Evans. Simple galaxy models with massive haloes. , 260:191–201, January 1993.
- L. Gao, S. D. M. White, A. Jenkins, F. Stoehr, and V. Springel. The subhalo populations of Λ CDM dark haloes. , 355:819–834, December 2004. doi: 10.1111/j.1365-2966.2004.08360.x.
- J. E. Gunn and J. R. Gott, III. On the Infall of Matter Into Clusters of Galaxies and Some Effects on Their Evolution. , 176:1–+, August 1972. doi: 10.1086/151605.
- R. Kotulla, U. Fritze, P. Weilbacher, and P. Anders. GALEV evolutionary synthesis models - I. Code, input physics and web interface. , 396:462–484, June 2009. doi: 10.1111/j.1365-2966.2009.14717.x.
- P. Kroupa. On the variation of the initial mass function. , 322:231–246, April 2001. doi: 10.1046/j.1365-8711.2001.04022.x.
- P. Kroupa. The Fundamental Building Blocks of Galaxies. In C. Turon, K. S. O’Flaherty, & M. A. C. Perryman, editor, *The Three-Dimensional Universe with Gaia*, volume 576 of *ESA Special Publication*, pages 629–+, January 2005.
- K. Kuijken and J. Dubinski. Nearly Self-Consistent Disc / Bulge / Halo Models for Galaxies. , 277:1341–+, December 1995.
- R. B. Larson, B. M. Tinsley, and C. N. Caldwell. The evolution of disk galaxies and the origin of S0 galaxies. , 237:692–707, May 1980. doi: 10.1086/157917.

- T. Lejeune, F. Cuisinier, and R. Buser. A standard stellar library for evolutionary synthesis. II. The M dwarf extension. , 130:65–75, May 1998. doi: 10.1051/aas:1998405.
- T. Lisker, E. K. Grebel, and B. Binggeli. Virgo Cluster Early-Type Dwarf Galaxies with the Sloan Digital Sky Survey. I. On the Possible Disk Nature of Bright Early-Type Dwarfs. , 132:497–513, August 2006. doi: 10.1086/505045.
- T. Lisker, E. K. Grebel, and B. Binggeli. Virgo Cluster Early-Type Dwarf Galaxies with the Sloan Digital Sky Survey. Iv. The Color-Magnitude Relation. , 135:380–399, January 2008. doi: 10.1088/0004-6256/135/1/380.
- J. Makino. Optimal order and time-step criterion for Aarseth-type N-body integrators. , 369:200–212, March 1991. doi: 10.1086/169751.
- J. Makino and S. J. Aarseth. On a Hermite integrator with Ahmad-Cohen scheme for gravitational many-body problems. , 44:141–151, April 1992.
- J. Makino and P. Hut. Performance analysis of direct N-body calculations. , 68:833–856, December 1988. doi: 10.1086/191306.
- C. Mastropietro, B. Moore, L. Mayer, V. P. Debattista, R. Piffaretti, and J. Stadel. Morphological evolution of discs in clusters. , 364:607–619, December 2005. doi: 10.1111/j.1365-2966.2005.09579.x.
- D. E. McLaughlin. Evidence in Virgo for the Universal Dark Matter Halo. , 512:L9–L12, February 1999. doi: 10.1086/311860.
- B. Moore, G. Lake, and N. Katz. Morphological Transformation from Galaxy Harassment. , 495:139–+, March 1998. doi: 10.1086/305264.
- J. F. Navarro, C. S. Frenk, and S. D. M. White. The Structure of Cold Dark Matter Halos. , 462:563–+, May 1996. doi: 10.1086/177173.
- E. E. Salpeter. The Luminosity Function and Stellar Evolution. , 121:161–+, January 1955. doi: 10.1086/145971.

- P. L. Schechter and P. J. E. Peebles. On the Significance of the Luminosities of First-Ranked Members of Sparse Groups of Galaxies. , 209:670–677, November 1976. doi: 10.1086/154766.
- F. H. Shu. Models of Partially Relaxed Stellar Disks. , 158:505–+, November 1969. doi: 10.1086/150214.
- R. Smith, J. I. Davies, and A. H. Nelson. How effective is harassment on infalling late-type dwarfs? , 405:1723–1735, July 2010. doi: 10.1111/j.1365-2966.2010.16545.x.
- R. Spurzem. Direct N-body Simulations. *Journal of Computational and Applied Mathematics*, 109:407–432, September 1999.
- R. Spurzem, M. Giersz, D. C. Heggie, and D. N. C. Lin. Dynamics of Planetary Systems in Star Clusters. , 697:458–482, May 2009. doi: 10.1088/0004-637X/697/1/458.
- R. B. Tully. Alignment of clusters and galaxies on scales up to 0.1 C. , 303:25–38, April 1986. doi: 10.1086/164049.
- R. B. Tully and E. J. Shaya. Infall of galaxies into the Virgo cluster and some cosmological constraints. , 281:31–55, June 1984. doi: 10.1086/162073.

Acknowledgments

I would like to give my very special thanks to my supervisors Prof.Dr. Rainer Spurzem and Dr. Thorsten Lisker and to Prof.Dr. Eva Grebel for the incredible academic and personal support I have received from them during this PhD thesis developing process. I have no words to express how grateful I feel towards them.

Also, I want to thank deeply Dr. Cristoph Olczak for all his great suggestions, the very useful technical support I have received from him when developing this project, for the friendship and good company during the time we worked together in China and now at ARI.

I would like to thank Dr. R. Kotulla for providing the code for computing spectral properties that will be used by integrated within the Nbody6 GPU code. I also would like to thank Dr. T. Tsuchiya for providing his version of the Kuijken & Dubinski (1995).

I would also like to thank Dr. Cristina Afonso and Dr. Roland Gredel for their great support and help provided through this long process. Also I would like to thank Prof. Dr. Reinhardt Mundt and Dr. Christian Fendt for all their attentions together with all the people that made possible this process to be continued. I do appreciate it deeply. To Dr. Christian Wolf and Dr. David Martínez-Delgado for the trust and support I received from them while my stay in MPIA.

To the International Max Planck Research School (IMPRS), the Astronomisches Rechen Institut (ARI) and other institutions that have provided me with funding for developing this work.

I want to thank the rest of my PhD committee examiners Prof. Ralf Klessen and Prof. Karlheinz Meier for accepting to be part of my doctoral committee thesis and the secretaries of the Dean's office for their help and advice during the thesis submission process.

I want also to tell my ex-officemates Justus Schneider and Stefan Lieder that I spent a great time with them and I value deeply all the personal support I got from them.

To the people that is part of my two working groups for being always so helpful and for the useful group meetings. To Frau Saskia Mayer, Dr. Peter Schwkendiek and all the ARI staff for being always so polite and helpful whenever I have required their help.

The time I have spent in ARI so far, has been full of nice moments in a great working atmosphere. It has been a wonderful experience to belong to this institute.

I want to thank also the people I worked with in Beijing ,China. Specially to those whom I worked closely with: Prof. Dr. Rainer Spurzem, Dr. Christoph Olczak and Dr. Peter Berczik for the great experience, the good times and the very useful support I received from them in the time spent there.

To Dr. Eric Peng for being part as external member of my IMPRS committee PhD thesis and for his useful comments and suggestions concerning my PhD thesis project.

To the National Astronomical Observatories of China and the Kavli Institute for Astronomy and Astrophysics members for hosting me during three months and for the facilities provided for developing part of this project. My time spent in China was a wonderful experience in all senses.

During all the time I have spent in Heidelberg, I have made great friendships that have been with me through all this life process which would have been very hard to live alone if I didn't have the great luck of meeting them:

I want to thank the great friends I made in MPIA: Aday Robaina, Vernesa Smolic, Florian Rodler, Javier Rodón, Andrés Carmona, Victoria Rodríguez and José Borelli for the wonderful moments we spent there and for all the great times we have spent outside too.

To my dear girls, Giulia Vannoni, Giovanna Pedaletti and Claudia Mignone. Giovanna and Claudia also for being the best roommates one can ever have. To the three of you for taking care of me soooo much and for the great times we have shared together.

Also, to my dear friends Vivi Tsalmantza, Olga Zacharopoulos, Matteo Bocchi, Viviana Niro, Sara Vallero and Alessandro Berton. To Giovanni Natale, Jamie O' Sullivan, Marik B. Heider, Dusan Budjas, Emma De Oña, Yolanda Sestay, Paulina Ordoñez, Domenico Tamburro, Dominik Riechers, Kester Smith and lots of other people that I've met and have made my life here much better.

To my great friends Nicole Kaliwoda, Frida and Janosch Weber and his family for being with me in the most difficult times and for supporting me so much always but overall in those not so good days I also have passed here. I will never forget it.

To my dear old friends from Mexico that even with the distance, they have always been around loving me and making sure that I'm doing well: Verónica Lora, Luis Acosta, Julio Cruz, Luis Mier y Terán, Federico de Mateo and Carla García-Parrodi plus all the university friends. To my friends of even older times Claudia Hoyos, Angel Heredia and all the high-school gang.

To the wonderful family I have, specially to my mother Isabel that is the best person in the world and to my dear aunt Amelia. To my cousins Karina, Oscar and Jessica and specially to my dear cousin Adriana for caring about me so much always and being present

all the time!

Also to my father, that I hope is doing well somewhere. To the family friends Amparo, Consuelo, Yolanda, Teresita, Martha, Helen and their families for worrying about me and my family always but in particular all the time I have been here.